ISBN 978-82-471-1804-7 (printed ver.)
ISBN 978-82-471-2011-8 (electronic ver.)
ISSN 1503-8181

Doctoral theses at NTNU, 2010:28

Gullik Anthon Jensen

Offshore Pipelaying Dynamics

Doctoral Thesis

Gullik Anthon Jensen

Doctoral theses at NTNU, 2010:28

NTNU
Norwegian University of
Science and Technology
Thesis for the degree of
philosophiae doctor
Faculty of Information Technology, Mathematics
and Electrical Engineering
Department of Engineering Cybernetics

NTNU
Norwegian University of
Science and Technology

NTNU
Norwegian University of
Science and Technology

Gullik Anthon Jensen

Offshore Pipelaying Dynamics

Thesis for the degree of philosophiae doctor

Trondheim, February 2010

Norwegian University of
Science and Technology
Faculty of Information Technology, Mathematics
and Electrical Engineering
Department of Engineering Cybernetics

NTNU
Norwegian University of
Science and Technology

NTNU
Norwegian University of Science and Technology

Thesis for the degree of philosophiae doctor

Faculty of Information Technology, Mathematics
and Electrical Engineering
Department of Engineering Cybernetics

ISBN 978-82-471-1804-7 (printed ver.)
ISBN 978-82-471-2011-8 (electronic ver.)
ISSN 1503-8181

ITK Report 2010-4-W

Doctoral Theses at NTNU, 2010:28

Printed by Tapir Uttrykk

Summary

This thesis considers three issues regarding modeling of offshore pipelaying dynamics. These are: (i) the formulation of an offshore pipeline installation operation as a control problem, (ii) the development and passivity analysis of a robotic pipe model for a submerged pipe string, suitable for real–time applications in closed–loop control systems, and (iii) the development and validation of a nonlinear FEM model for simulation and control of the elastic pipeline dynamics, including FEM dynamics of a pipeline combined with vessel dynamics, for simulation and control of pipelay operations under dynamic positioning.

Pipeline installation is defined as the operation of positioning a pipeline along a reference path on the seabed from a surface vessel. In control terms, this can be stated as a path–following control problem, where the pipe touchdown point tracks the reference path. However, the only controllers for the touchdown point are the pay–out of pipe into the water, and the motion of the surface vessel. Considering that the pipe is an elastic body, and that both the pipe and the vessel are subject to environmental loads, the control problem that must be considered is a dynamic target–tracking problem, where the surface vessel must track a moving target position on the surface in order to control the position of the touchdown point. A target–tracking controller may be implemented as a guidance system, by extending the dynamic positioning system that is common for pipelay vessels. An important component in the guidance system is the dynamic pipe model mapping touchdown and surface vessel position.

Motivated by robotics, a compact system formulation is derived for the suspended pipeline by considering it as a hyper–redundant manipulator with an arbitrary number of links. This model captures the main dynamics of the pipe, including its geometric configuration and top tension. The model is in the state–space, and on a vectorial form using minimal coordinates. A passivity analysis establishing input–output passivity of the system is performed. This model is applicable in simulations where the main dynamics are required, and the available computation time is limited.

Static and dynamic analysis of pipelines during installation is characterized by a combination of geometrical nonlinearities and extreme flexibilities of the system. A nonlinear PDE formulation for the pipeline is developed based on a three–dimensional elastic beam model, taking into account the internal forces of longitudinal extension, shearing, twist and bending, as well as external loads from gravity, buoyancy, hydrodynamic drag, seabed interaction, and environmental loads. This

highly flexible system is then coupled to a dynamic model of the pipelay vessel. A passivity analysis establishing input–output passivity of these systems separately, and combined, is performed.

A nonlinear FEM model, based on exact kinematics, is derived to approximate the solution of the PDE pipe formulation. The weak formulation of the PDE is semi–discretized in the curve parameter into a finite dimensional space to obtain an explicit set of ordinary differential equations. This semi–discretized model is solved by using standard integrators for time. The set of ordinary differential equations is a convenient representation for simulation and control of pipelay operations under dynamic positioning. The model is successfully validated against the natural catenary and the commercial FEM code RIFLEX. The model has potentially numerous applications in dynamical analysis, in control system design and simulation, and in tools for training and decision support.

Acknowledgments

The research presented in this thesis is the result of my doctoral studies performed from September 2005 to September 2009, at the Department of Engineering Cybernetics (ITK), and Centre for Ships and Ocean Structures (CeSOS) at the Norwegian University of Science and Technology (NTNU). The Norwegian Research Council (NFR) provided the funding for this project through the strategic university program (SUP) on Computational Methods in Nonlinear Motion Control (CMinMC), directed by Professor Tor Arne Johansen.

Thanks are due to many. First of all, I would like to thank my supervisor, Professor Thor I. Fossen at the Department of Engineering Cybernetics, NTNU. He supported and encouraged me during my work, and his optimism and enthusiasm rubbed off on me. He provided a good working environment, and his office door has always been open to me. For this I offer my sincerest gratitude. I am thankful to my co–supervisors, Professor Carl M. Larsen at the Department of Marine Technology, NTNU, for willingly sharing his vast knowledge on pipelines and risers, and Dr. Tu Duc Nguyen for sharing his extensive knowledge on control, and for always being positive and encouraging. I would also like to thank former professor Olav Egeland for having faith in my abilities, and granting me the possibility to pursue a PhD degree.

The research work has generated several publications, and I am grateful to the co–authors, Dr. Niklas Säfström, Dr. Aksel Andreas Transeth, and Morten Breivik, for complementing and extending my own knowledge by their contributions. In particular, I am deeply grateful to Dr. Niklas Säfström, whom at the time was a PhD student at the Department of Mathematical Sciences, NTNU. The collaboration has been enjoyable, and his contributions are instrumental to the results presented in this thesis. I would like to acknowledge Dr. Yilmaz Türkyilmaz who's initial work on the nonlinear FEM model for offshore pipelaying provided an excellent starting point for my own research, and Dag Fergestad, MARINTEK, for producing the RIFLEX data applied for the validation of the nonlinear FEM model.

I would like to thank the capable staff at the Department of Engineering Cybernetics, in particular Tove Blomset Johnsen and Eva Amdahl of the administration for handling the paper work. I would like to thank Professor Svein Sævik at Institute of Marin Technology, NTNU, for proofreading Chapters 2 and 3.

I am grateful to have had the privilege of so many good colleagues during my studies. In particular, the fellowship of PhD students at the department has been

unique, and my stay has in particular been enjoyable thanks to Johannes Tjønnås, Giancarlo Marafioti, Mernout Burger, Esten Grøtli, Morten Breivik, Christian Holden and Hege Langjord. We started out as colleagues, we ended up as friends. I would also like to thank my good friend Svein Børge Nygård for always listening and being a supporter.

Finally, I give my unconditional love and gratitude to my loving wife Line Rørstad Jensen, and my three wonderful children, Marthine, Gullik and Oda Natalie. These have been trying times, but together we made it.

Gullik A. Jensen
Trondheim, January 2010

Contents

Chapter 1

Introduction

Slender marine structures are characterized by having a small cross–section area compared to the overall structure length, and in the offshore industry these structures have many applications, e.g., mooring lines, umbilicals, towers, pipelines and risers (drilling risers, production risers, export risers and workover risers). The success of marine operations depends on good understanding of the dynamics of these structures. This understanding can be acquired from analysis and simulations of the structures based on mathematical models.

In this thesis offshore pipeline installation from a surface vessel, a so–called *pipelay operation*, is considered, see Figure 1.1. The main objective of the operation is to position an elastic pipeline along a predefined path on the seabed only by means of active control of the pipelay vessel position, while at all times ensuring the structural integrity of the pipe.

Offshore pipelines are essential for the transportation of oil and gas, and range from small diameter interfield flowlines to large diameter export lines for transportation from offshore installations to shore and for transportation across oceans between countries. The use of subsea pipelines represents a safe and environmentally friendly mean of transportation (Collier and Rosier, 1995).

Currently, efforts are being made to locate and retrieve oil and gas resources in increasingly deeper waters, and offshore pipeline technology is constantly evolving to keep up with these advances. Hence, the main drives in the offshore pipeline industry today concerns installing pipes at large water depths, and in particular the development of large gas gathering and distribution systems throughout the world, e.g., the Langeled and Independence Trail pipelines, in the North Sea and the Gulf of Mexico (GOM) respectively.

1.1 Motivation

The general motivation for this thesis is to consider dynamics and control of flexible structures in offshore pipelay operations. To be more specific, the main motivation is mathematical modeling for control of elastic pipeline dynamics using nonlinear

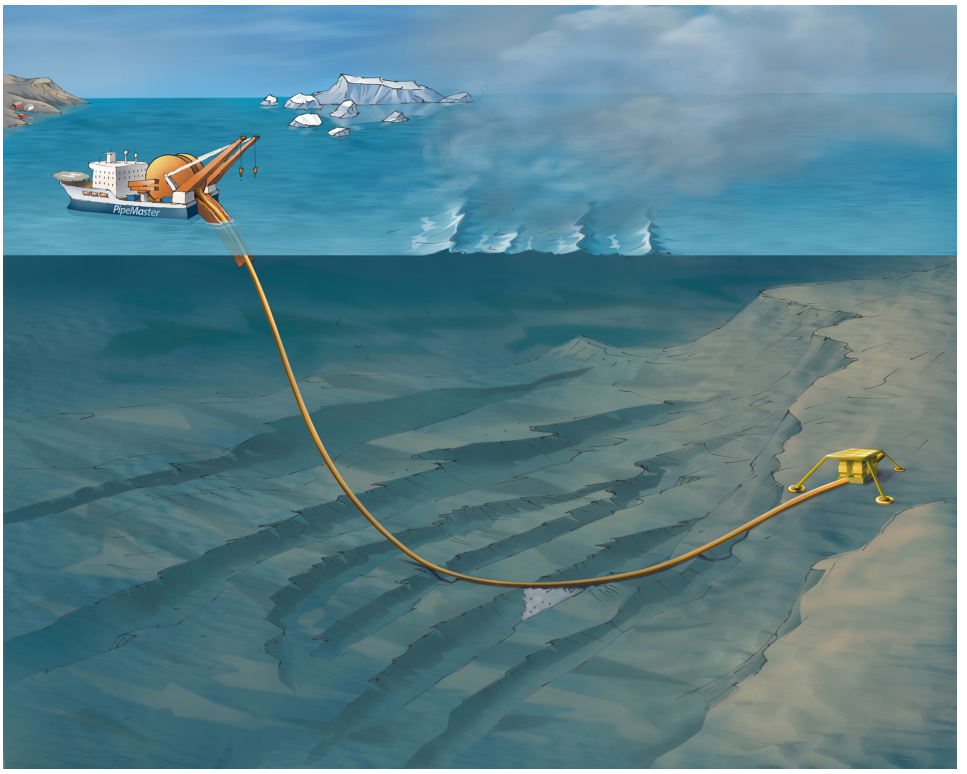

Figure 1.1: An artist's impression of an offshore pipelaying operation. Illustration: Bjarne Stenberg/MARINTEK.

Finite Element Models (FEM[1]) based on exact kinematics, and also combining FEM dynamics of a pipeline with vessel dynamics for simulation and control of pipelay operations under dynamic positioning.

Existing FEM models and codes are mainly designed for analysis purposes, and are not directly applicable for control applications. Hence, the main task in this thesis is to derive a new dynamic FEM formulation for an elastic pipeline, with performance and accuracy equal to that of existing FEM models, with properties that also makes it suitable for simulation and control applications.

For some simulation scenarios, and in control applications which requires real–time performance, applying a FEM model for the pipe dynamics is overly complex. A simpler pipe formulation, which still captures the main dynamics of the system, is also considered.

Finally, The field of offshore pipelaying has evolved with little influence from the field of control engineering. Hence, the scope of the thesis was extended to

[1]FEM is also an abbreviation for *Finite Element Method*, which is a numerical technique for finding approximate solutions of partial differential equations. To avoid confusion, the terms *FEM model* and *FEM method* are frequently used.

encompass an introduction to the background, methods, and challenges in offshore pipelaying presented in a control engineering perspective.

1.2 Pipeline Modeling

In the design phase of a typical offshore pipeline project today, mathematical models for the pipeline are needed to determine pipe properties, pipelay parameters, and the conditions under which the pipeline can safely be installed. Offshore pipelay operations were first conducted in shallow waters close to shore, where the strains and stresses in the pipe could satisfactory be approximated by analytic models, such as the catenary equation known from cable mechanics (Irvine, 1981), and the stiffened catenary equation (Plunkett, 1967; Dixon and Rutledge, 1968). As pipelay operations were taken into deeper waters the dynamic behavior of the pipe became significant. Hence, dynamic pipe models based on elastic beam models, known from continuum mechanics, were introduced. These models were discretized, using e.g., the finite element method (FEM), or the finite difference method (FDM), and solved numerically using computers.

Today, static models are mainly limited to determine the required equipment capacity. For large projects, and if the required equipment capacity is close to its limits, dynamic analysis are also performed. For the dynamic analysis and simulations of pipelay operations, computer codes based on FEM, e.g., RIFLEX, ABAQUS, OFFPIPE and SIMLA, are the method of choice, since these computer codes produce high quality discrete dynamic models. In these codes, the FEM models of the structures to be analyzed are developed by joining already defined finite elements.

Recent research propose new models tailored for control applications. Two models for cables used for trawling is developed in (Johansen, 2007), and tensegrity structures are considered in (Worldsen, 2007).

1.2.1 Model Classification

Mathematical models for offshore pipelines are classified in three groups, distinguished by their complexity and number of differential equations needed, see Figure 1.2. *The simulation model* is the most accurate description of the system, and should be able to reconstruct the time response of the real system. These are typically the mentioned FEM models used for dynamic analyses. *The controller model* is a reduced order or simplified model of the simulation model used for the implementation of a feedback control system. Model based controllers use a dynamic model to generate the feedforward and feedback signals. *The observer model* is like the control model, a reduced order or simplified simulation model, but will in general be different from the control model, as it is designed to capture the additional dynamics associated with the sensors system. The controller and observer models are used on–line in the control system implementation. The simulation model is used for validation of different controller schemes in computer simulations that does not impose real–time performance requirements. Validation

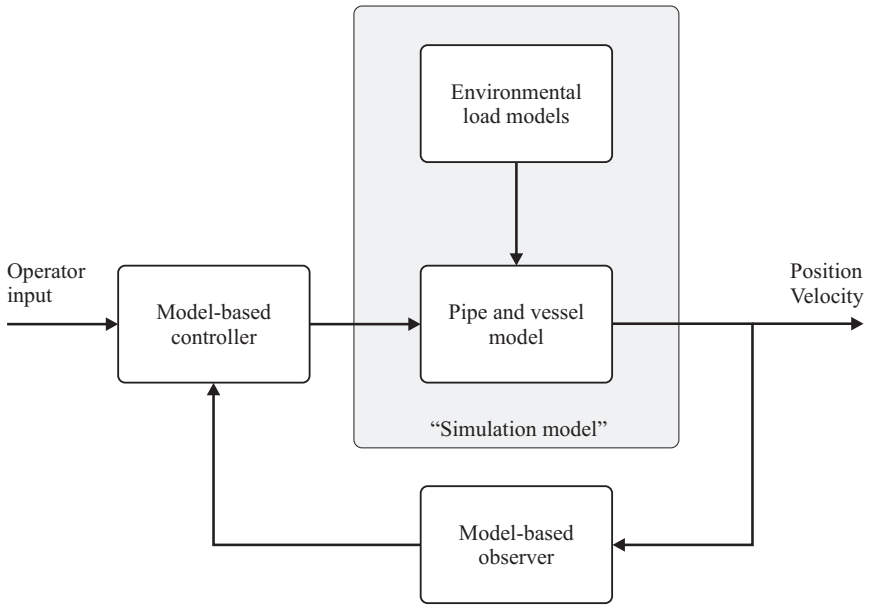

Figure 1.2: Model classification

through simulation is considerably cheaper than sea trials, and there are virtually no limitations to possible test scenarios.

1.2.2 Model Requirements

Albert Einstein has been attributed the statement: *'Everything should be made as simple as possible, but no simpler'*, which applies well to control and observer models, which should be as simple as possible, while still capture the main system dynamics. The following requirements must be satisfied by the control and observer models implemented in a control system:

1. *Real–time computation* – The model must be simple enough to compute in real–time.

2. *Dynamic* – The model must capture the main dynamics of the pipe.

3. *Stability* – The closed–loop system must be stable, preferably asymptotically stable. The model should inherit the stability property of the modeled system, which generally are assumed to be stable. However, for some applications, the modeled system is unstable, in which case the controller must be designed to ensure the stability of the closed–loop system.

4. *Accuracy* – The computation must be sufficiently accurate for the application. Integral action in feedback controllers can compensate for offsets.

The accuracy requirement for the simulation model is stricter than that of the controller and observer models, while the real–time computation requirement is relaxed. The requirements on dynamics and stability however, are the same.

1.2.3 Automating Pipelay Operations

Applying current technology, the tasks involved in pipelay operations are mostly performed by manual control, such as e.g., the dynamic positioning (DP) systems for vessel positioning. It seems plausible that introducing more automatic control in these systems can improve the performance in this industry, as it has for several other industries, including the process industry, aerospace industry (Åström, 1996).

In the applied pipeline construction methods, *tension* is the most important single parameter to control, and control systems can be designed for tension control. Considering control applications at a higher level, *guidance systems* are a natural extension to the DP systems that most modern pipelay vessels are equipped with. A guidance system automates the task of determining the optimal motion of the vessel. Consequently, closed–loop automatic control for pipelay operations is a relatively new application which may now gain more attention as DP systems have become standard for deep–water pipelay operations.

The issue of stability of the closed–loop feedback system arises when FEM computer code models are considered for application in model–based controllers. The pipe model must be shown to be passive, and the potentially large number of states and equations may complicate this analysis. However, mechanical flexible systems are continuous with infinite degrees of freedom, so–called *infinite–dimensional*. In practice these systems are modeled as finite–dimensional with a large number of dimensions, and the fundamental problem of actively controlling such systems is to control the large–dimensional system with a much smaller dimensional controller. This issue was addressed by Balas (1978), who showed that such controllers can become unstable when connected to systems with infinite degrees of freedom even if the discrete model is shown to be passive. This is due to the unmodeled modes in the system, named *the spillover*, which the controller does not account for.

1.3 Thesis Organization

The remaining chapters in this thesis are organized as follows:

- *Chapter 2* – An introduction to and overview of offshore pipelay operations which is suited for control researchers is given. This chapter also looks at the possibility of automating such operations beyond the manual DP–based control procedures of today since it seems plausible that control systems can be used to further improve the performance and profit of pipelay operations.

- *Chapter 3* – An offshore pipeline is an elastic body with complex dynamics. This chapter is on structural analysis, which considers the internal and external loads that governs these dynamics.

- *Chapter 4* – The natural catenary equation still has a significant position in the static structural analysis for risers and pipelines during installation and for computing tension. Due to this strong position, the catenary will be applied as a benchmark to validate the models developed in later chapters. In this chapter the catenary equations is derived, and a quasi–static nonlinear spring equivalent for the tension experienced by a pipelay vessel at the pipe surface end is derived.

- *Chapter 5* – In this chapter, a dynamic representation of the pipe and its kinematics is developed, that can replace the catenary pipe tension model for simulation and control applications. This representation is motivated by robotics, which yields a compact model as a set of ordinary differential equations (ODE), for effective implementation in a computer code. This model is intended for replacing the catenary equation for computing a dynamic tension in simulations and controllers, which is also capable of including flexural effects.

- *Chapter 6* – In Chapter 6 a nonlinear dynamic PDE formulation for a pipe string suspended from a pipelay vessel to the seabed in a pipelay operation is developed. This model extends a three–dimensional beam model capable of undergoing finite extension, shearing, twist and bending, to apply for marine applications by adding the effects of restoring forces, hydrodynamic drag and seabed interaction. The model is extended to include the pipelay vessel dynamics by applying a potential theory formulation of a surface vessel, suited for dynamic positioning and low speed maneuvering, as a boundary condition for the PDE. This system is found to be input–output passive and stable. Pipeline installation applications where the presented PDE is suited are e.g., analysis and simulation of the installation operation, operability analysis, hardware–in–the–loop (HIL) testing for vessel control systems, and automation of the pipelay operation.

- *Chapter 7* – The model developed in Chapter 6 is then validated against the natural catenary equation and the FEM code RIFLEX in Chapter 7.

- *Chapter 8* – Conclusions and recommendations for further work are made.

- *Appendix A* – In this chapter mathematical preliminaries on the concepts of coordinate vectors, reference frames applied in this thesis, rotation matrices and differentiation of coordinate vectors, are reviewed. This section should be read first by anyone not familiar with these concepts and their applications.

1.4 Contributions

The main contributions in this thesis are:

- The development of a nonlinear dynamic model for an elastic pipeline in a marine environment. The model is derived from physics, as the balance of linear and angular momentum for the elastic body with boundary conditions.

This model preserves the system energy and passivity properties, which is lost for linearized models. The model is continuous, and expressed as a PDE. A FEM model is derived from the PDE model by using a Galerkin method, which is a part of calculus of variations. This FEM model is validated against the natural catenary equation and the internationally leading FEM code for slender marine structures, RIFLEX. The validation shows a very good agreement between the models. *(Chapters 6 and 7).*

- The development of a dynamic nonlinear robot like pipe model. The model captures the main dynamics of the pipe, and input–output passivity is proved. The model is suitable for control, and it may replace the quasi–static tension models based on the catenary. *(Chapter 5).*

- The definition of the Pipelay Problem as a control problem, and guidance control concepts related to extending the capabilities of DP systems installed in most pipelay vessels today. *(Chapter 2).*

1.5 List of Publications

Publications by the author related to the work presented in this thesis.

- Jensen, G. A., Säfström, N., Nguyen, T. D. and Fossen, T. I., A Nonlinear PDE Formulation for Offshore Vessel Pipeline Installation, Journal of Ocean Engineering, DOI: 10.1016/j.oceaneng.2009.12.009 *(In press)*

- Jensen, G. A., and Fossen, T. I. A Robotic Approach to Nonlinear Dynamic Modeling of Offshore Pipelaying Operations. In Proceedings of the 8th MCMC, Guarujá (SP), Brazil, September 16–18, 2009.

- Jensen, G. A., Säfström, N., Nguyen, T. D. and Fossen, T. I., Modelling and Control of Suspended Pipeline during Pipelay Operation Based on a Finite Strain Beam Model. In Proceedings of ACC, Saint Louis, June 10–12, 2009

- Jensen, G. A., Breivik, M. and T. I. Fossen, Offshore Pipelay Operations From A Control Perspective. In Proceedings of the 28th International Conference on Ocean, Offshore and Arctic Engineering (OMAE 2009), Honolulu, Hawaii, May 31–June 5, 2009

- Jensen, G. A. and T. I. Fossen, Mathematical Models for Guidance and Control of Offshore Pipelaying. In Proceedings of the 28th International Conference on Ocean, Offshore and Arctic Engineering (OMAE 2009), Honolulu, Hawaii, May 31–June 5, 2009

- Jensen, G. A., Transeth, A. A. and Nguyen, T. D., Modelling and Control of Offshore Marine Pipeline during Pipelay. In Proceedings of the 17th IFAC World Congress, Seoul, Korea, July 6–11, 2008.

- Säfström, N., Jensen, G. A., Nguyen, T. D. and Fossen, T. I., A Nonlinear Elastic Model Applied to Pipelay Operation in Ocean Engineering. In Proceedings of 21st Nordic Seminar on Computational Mechanics, NSCM–21, 2008.

Chapter 2

Offshore Pipelaying

The installation of pipelines and flowlines and their connection to platforms constitute some of the most challenging offshore operations. The level of engineering sophistication and effort required, as well as the size and cost of the various types of installation vessels used have reached such a level that pipelaying has developed into an engineering discipline of its own accord (Kyriakides and Corona, 2007).

This chapter provides the reader with basic knowledge of the objectives, challenges, methods and background for offshore pipelaying, which will serve as the application case for the results developed in later chapters. The presentation is biased from a control engineers perspective. The major milestones in the development of offshore pipelaying as a discipline are presented, along with the current methods and equipment used in offshore pipeline construction. The pipe installation methods covered are:

- S–lay – (Section 2.2.1),
- J–lay – (Section 2.2.2),
- Reeling – (Section 2.2.3) .

Concepts of control in the pipelay operation are addressed with respect to controlling the pipe deformation from the vessel to the seabed, pipelay vessel motion control using anchors or dynamic positioning (DP), and position and motion control of the pipe touchdown point at the seabed. The measurements available during installation are listed as well as the standards governing most pipelay operations.

A pipeline development project is typically divided into three phases: *design*, *installation*, and *commissioning and operation*. In the design phase, the pipeline path and the pipe properties are determined. The path consists of straight and curved sections on the seabed which the pipe must be placed along, and is documented through detailed layout drawings, alignment sheets and bathymetry maps. Initially, the pipe diameter, wall thickness, material grade selection, the need for thermal insulation and coating is determined by the physical and chemical properties of the fluid the pipe is designed for. Then a pipelay analyses are performed. The static pipeline installation analysis forms a check on the pip laying vessel and

the equipment capabilities, and to check the initial stresses and strains within the pipeline. For complex installations, a more complex dynamic analysis is performed to account for dynamic effects during the installation. The choice of installation method may influence the design parameters of the pipeline.

Following the design phase is the installation phase, which covers all the activities following the fabrication of the pipe joints until the pipeline is ready for commissioning and operation. However, in this thesis, the term *installation* will be defined as the task of positioning the pipe on the seabed only. From a control perspective, the S–lay and J–lay methods are similar, and the following definition of pipeline installation will be applied in the remainder of this thesis:

Definition 2.0.1 ***Pipeline Installation (Pipelay)*** *Pipeline installation is defined as the operation of positioning a pipeline on the seabed from a surface vessel. The pipe is extended from the vessel at a pay–out speed* $U_p(t) \geq 0$*, and at a departure angle* $\alpha \in [0, \pi/2\rangle$*, defined relative to the mean sea surface.*

For the S–lay method the departure angle from the stinger is depending on the water depth, and will vary from close to horizontal, in shallow waters, to near vertical in deep waters. For the J–lay method $\alpha \approx \pi/2$. For the on–site pipe–assembly methods, the pay–out speed $U_p(t)$ will switch between $U_p(t) = 0$ when the pipe is being constructed and $U_p(t) > 0$ when the newly constructed pipe is payed out. Reeling methods allows a constant pay–out speed.

Over the preceding decades, development of offshore pipeline technology has mainly been reported at conferences such as the *Offshore Technology Conference* [1] (OTC), *International Conference on Offshore Mechanics and Arctic Engineering*[2] (OMAE), and *Offshore Pipeline Technology* (OPT). However, during recent years, the field has become more accessible by the publication of several textbooks, which are partly complementary, partly overlapping.

A general non–technical introduction to pipeline construction is given by Miesner and Leffler (2006) and more specifically for offshore applications, including pipelines, by Leffer et al. (2003). Decades of accumulated experience in the field, covering most topics are presented in Palmer and King (2008). Guo et al. (2005) provide useful introductions to technical aspects, where a more comprehensive overview of design methods, aimed at both new and experienced pipeline engineers are provided in Bai and Bai (2005). The book by Braestrup et al. (2005) restricts attention to the design and installation, while detailed mechanical design methods are found in Kyriakides and Corona (2007).

2.1 The History

The offshore pipeline industry has developed alongside the offshore oil & gas industry from a modest beginning in the years following World War II, to a mature

[1] The Offshore Technology Conference has been held annually since 1969 in Houston, Texas, USA. The event is focusing on the development of offshore resources in the fields of drilling, exploration, production, and environmental protection. The OTC Internet site: http://www.otcnet.org

[2] The OMAE is an international conference held annually since 1982. OMAE Internet site: http://www.omae.org

and global industry today. The global unprecedented need for energy drives the oil & gas industry constantly into deeper waters, and more hostile environments in search for recoverable resources. These drives generate a need for new pipelines, and the challenge of the pipeline engineers have always been to come up with methods and equipment to meet these needs. As a consequence of this, the offshore pipeline industry is highly market driven, and the methods are results of experience of installation crew and the engineering skill of the design teams at the contracting companies. Operating in the oil & gas business, the offshore pipelay industry is venerable to the fluctuation of the oil price, and cycles between boom an recession. The parts of this historic section related to the period from 1970 to 2000 is adopted from Timmermans (2000).

2.1.1 Operation Pluto

A forerunner to modern offshore pipelaying is *Operation Pluto*, its name an acronym for *Pipe–line Under the Ocean*. Operation Pluto was a secret World War II operation by British scientists, oil companies and armed forces to construct undersea pipelines under the English Channel between England and France to supply fuel to the Allied forces during the later invasion. The preparations was already undertaken in 1942, at a time where an invasion seemed highly unlikely. Two types of pipelines where developed. The *HAIS* pipe was a flexible 3 inch (75 mm) pipe with a lead core based on existing undersea telegraph cables, and the *HAMEL* pipe was a steel pipe of the same diameter. Once the invasion became a reality, the first pipeline (HAIS), was successfully installed between Shanklin Chine on the Isle of Wight through the English Channel to Cherbourg, a distance of 130 km, on August 12, 1944. A total of four lines were installed between these ports, and an additional seventeen pipelines were laid from Dungeness to Ambleteuse in the Pas–de–Calais as the fighting moved east. The installation of of HAIS pipeline was conducted with ships equipped with handling gear, while the HAMEL pipe was too rigid for the conventional installation methods, and the pipe had to be installed on special floating drums, named *Conundrums*, designed for this purpose only, see Figures 2.1 and 2.2. The pipelines of operation Pluto provided a total of $781\,000\,m^3$ of gasoline to the Allied forces until victory were declared in Europe on May 8, 1945.

Operation Pluto is thoroughly described by Searle (2004), and more than 1000 photographs of the pipeline operation has been unclassified and are now available to be viewed at The National Archives[3] in Kew, London.

2.1.2 The 1950s and 1960s

The history of modern offshore pipeline industry started in GOM, where in the early 1950s, regular onshore based oil companies moved into the water, starting near shore, and gradually moved into open waters. The first out–of–sight installation was completed in 1947, and in the 1950s and 1960s the industry boomed. In these early years, pipelines were laid from flat barges, and installed more by sheer muscle power than by efficient specially designed equipment. This time was very

[3]Internet address: http://www.nationalarchives.gov.uk.

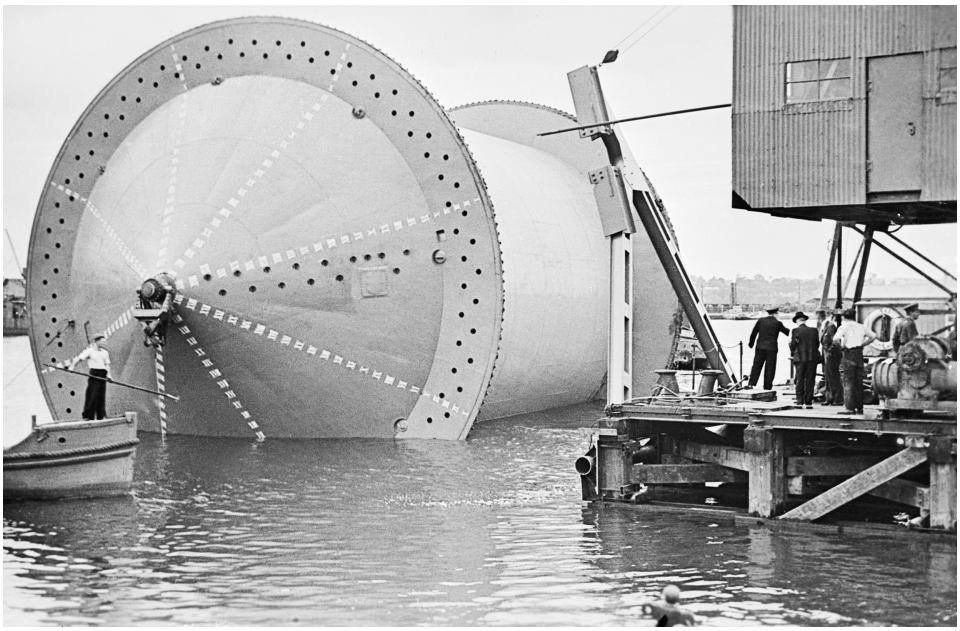

Figure 2.1: A Conundrum. By permission of The Imperial War Museum (T30).

much a pioneering time, and new methods and equipment were developed as the installation crews were running into obstacles. Examples are e.g., the inclined ramp for pipe support down to the seabed, allowing pipelaying in depths up to 15 meters, and the first stinger, which was like a ramp, but articulated and fixed to the barge only at one end. By the late 1960s, pipelaying under tension with a curved stinger and tensioners, a concept which is still used today, revolutionized the business. More on the pioneers of this time is found in (Pratt et al., 1997) and (Austin et al., 2004).

2.1.3 The 1970s and 1980s

By 1970 offshore exploration in water depths of $100 - 150$ meters in the North Sea led to the discoveries such as the Ekofisk field, and large gas fields off the southern coast of England. Pipelines were needed to bring oil and gas to shore in the UK, since limitations to the available technology made pipelines to Norway not feasible, as the pipeline would have to cross the Norwegian Trench. The physical climate of the North Sea was more severe than previously experienced, and the experience gained from decades of work in GOM by the pipeline industry, could not be applied. The productivity of the flat top laybarges was very low, and the pipes and stingers suffered much damage during the pipelay. Vessels with better seakeeping ability, capable of withstanding higher currents, to increase the operating window, as well as higher pipelay rates to exploit the available operating window better, was needed. Pipelay with the *Choctaw I* proved that the semi–

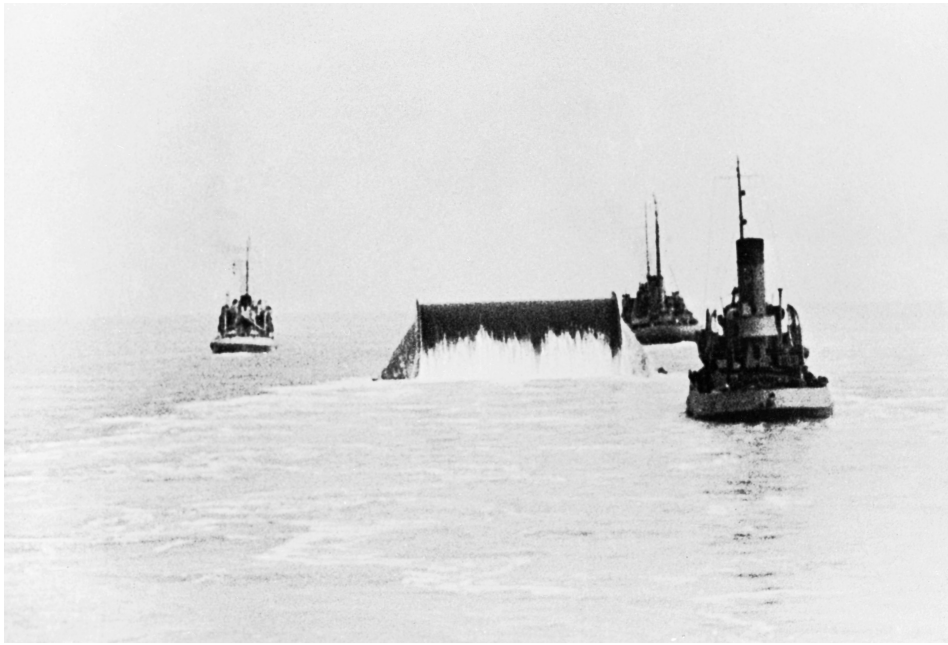

Figure 2.2: Un–reeling of HAMEL pipe from a Conundrum pulled by three tug boats. By permission of The Imperial War Museum (T29).

submersible hull shape successful, and by 1976 several large pipelay vessels with semi–submersible hulls had been added to the fleet, such as the *Viking Piper*, *Semac–I*, and *Castoro Sei*, which proved successfully in the North Sea. The second half of the 1970s suffered from low oil price, and offshore pipelaying experienced a downtime. By 1980 the industry was booming again, now projects were undertaken, and effort was put into research and development. Everything looked good, when in 1986 the oil price dropped again and caused severe damage to the industry.

2.1.4 The 1990s and the Present

The business finally recovered in the early 1990s, with new projects being realized. The water depth limit had been pushed to over 500 meters, and the traditional horizontal installation method with a stinger faced limitations, and the concept of vertical pipe installation, originally developed in the 1960's, gained attention. Several crane vessels were modified to handle J–lay, such as the *Balder* and the *DB–50*.

By the end of 1992, when the Soviet Union was disestablished and the last remains of the Cold War was gone, the offshore pipelaying industry became subject to globalization, and is now present in most parts of the wold, along with the oil & gas industry. Key deepwater areas are off the coast of Brazil, West Africa and GOM. The installation capabilities were by late 1990s close to 2000 meters and are now, ten years after, foreseen in depths close to 3000 meters (Knight and

Palathingal, 2007).

2.2 Pipeline Construction Methods

Pipelaying encompass installation methods whereby the pipe string is welded together from pipe joints, before the welds are inspected for defects and coated, all onboard a specialized pipelay vessel as it is installed on the seabed (Braestrup et al., 2005). Since the beginning of offshore pipelaying, several construction methods has been applied. The three methods that dominates installation of long pipelines today are *S–lay*, *J–lay*, and *reeling*. These methods will be described in the following sections. Note that so–called towing methods are not considered here.

To keep the pipe under tension to maintain the bending and axial stresses within an acceptable range is a key concept to all these installation methods. Through continually controlling the tension on the pipeline being laid, excessive bending and kinking of the pipeline is avoided without the necessity of extensive support structures or buoyant support means, which would not be feasible for deep waters. If sufficient tension for some reason can not be applied to the pipe, the pipe is lowered to the seabed in an abandoning procedure (A&R) for protection. When the conditions have improved, the pipe is retrieved and the operation continued.

The S–lay method is suitable for shallow to intermediate water depths, while the J–lay method is suitable for intermediate to deep water depths. Water depth is an inexact term, and the terms frequently used in literature are: *shallow*, *intermediate*, *deep* and *ultra–deep* waters. The exact water depths covered by each region has constantly been increased as pipelay operations has moved to increasingly deeper waters. Following Heerema (2005), 300 meters (1000 feet) considered deep before 1985, but since then 1500 meters (5000 feet) has become normal practice and also 2500 meters (8000 feet) is a reality. Studies are performed for installation at 3500 meters (11000 feet).

Depending on the installation method used, pipe properties, water depth and weather conditions, the length of pipe laid in a day varies from 1-1.5 kilometers for J–lay and up to 5 kilometers for S–lay. A typical rate for reeling is 14 kilometers per day. Since pipeline installation requires specialized vessels fitted with pipelaying equipment, there is only a limited number of vessels in the world. The main international companies that performs pipelaying are: Acergy, The Allseas Group, Saipem, Technip, Heerema, J. Ray McDermott, Global and Subsea7.

Comprehensive descriptions of installation methods can be found in any of the books listed previously, and details on pipelay vessels and equipment can be found on the Internet. In particular, the book by Kyriakides and Corona (2007) has a well written section on installation methods.

2.2.1 S–Lay

The most common installation method is S–lay, see Figure 2.3. Large numbers of pipe joints, typically 12 meters long, are manufactured and coated onshore. The pipe joints are brought to the pipelay vessel by supply vessels so that the pipe

construction can continue without interruptions. Onboard the S–lay vessel, the pipe joints are welded on to the end of the pipeline in a horizontal production facility called the *firing line*, which provides a sheltered environment for the workers that operates the multiple work stations for welding, non–destructive testing of the welds and coating. The pipeline is held in place to facilitate continued construction by so–called *tensioners*, which are large rolling caterpillar tracks with rubber pads that press on to the pipe going down to the seabed. When the pipe has been extended with the new pipe joints, the tensioners control the speed the finished pipe is extended from the vessel, called the *pay–out speed*, while maintaining the tension on the pipe as the vessel moves forward. The pay–out speed U_p is considered positive when the pipe is payed out, and its maximum value is limited by the mechanical properties of the tensioners. A sloping ramp supports the pipe as it moves from the vessel and onto the *stinger*. The stinger is a long open frame structure fitted with rollers which supports the pipeline and controls its curvature from the horizontal to the inclined section. The stinger is typically made out of several hinged sections to make it articulated. Hence, the stinger shape and curvature can be controlled by setting these segments at chosen angles. The overall stinger length depends on the pipelay vessel, but is typically in the range of 100 meters. The largest S–lay stinger is 130 meters, and mounted on the vessel Solitaire owned by The Allseas Group, see Figure 2.4. When the new pipe length has been payed out, the whole process is repeated.

The main advantage with the S–lay method is that the long firing line, running from bow to stern, enables parallel workstations for assembly of pipe joints, such that up to four pipe joints can be added at the time. This makes the method fast and economical, particularly for long pipelines. However, for large water depths, the pipe must be supported to a near vertical departure angle, which requires a very large stinger to avoid damaging the pipe. Also, with increasing water depths, the power needed to provide the required lay tension increases, which is directly transferable to high fuel expenses (Palmer, 1994). These are the main disadvantages of the method.

In shallow water of 100 meters, the lift off angle will typically be in the order of 30° from the horizontal. For increasing water depth, the lift off angle also increases up to 90° if the tension is kept within practical limits. This is commonly known as *Steep S–lay* (Perinet and Frazer, 2008), which can be performed by vessels like the Solitaire. This stinger configuration has shown to reduce the tension in the pipe compared to the traditional S–lay method. Furthermore, pipeline engineers argue that it will be safe to relax the standard strain level of the design in order to reach greater depths and handle even heavier pipelines (Perinet and Frazer, 2008).

The S–lay vessels can be classified into four generations (Guo et al., 2005).

1st Generation

The first generation S–lay vessels were flat–bottom spud barges where the pipe string was jointed horizontally on the open deck. Until early 1950s, these barges were mainly used in very shallow waters such as swamps and inland waters, bays, rivers, and marsh areas of the shallow GOM. The pipelines were laid by sheer

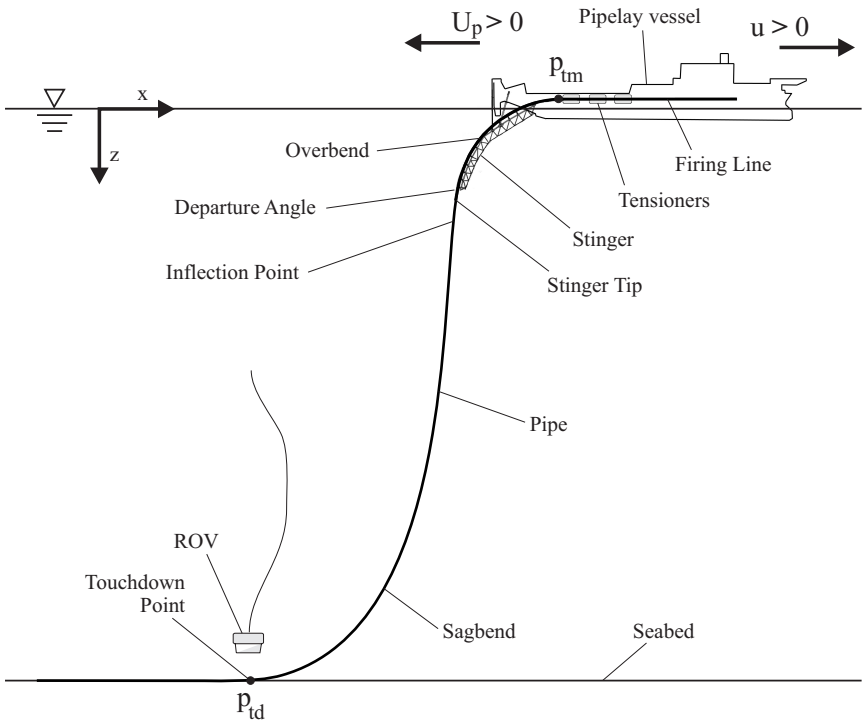

Figure 2.3: S–Lay pipe construction schematic.

muscle power since little or no efficient specially designed equipment had yet been designed.

Buckling and kinking occurred frequently, as the pipeline was not tensioned during the installation. In an effort to reduce the buckling, a ramp was attached to the side of the barge *Herman B* to support the pipe down to the seabed in 1954, and allowed the barge to install pipe in water depths up to 15 meters (40 feet) (Pratt et al., 1997). The next step in the development came in 1956, when the barge *M–211* was the first vessel to be fitted with a stinger. This stinger was a cradle consisting of two parallel 30–inch pipes, where the buoyancy of these pipes could be controlled to ease the pipeline to the bottom in deeper waters. However, this stinger was completely articulated and the shape and curvature could not be controlled. In 1958 Brown & Root built the *L.E. Minor*, which was the industry's first purpose–built lay barge, and it was bigger and faster than any other vessel at the time.

2nd Generation

The major disadvantage with the first generation pipelay vessels, which limited the maximum water depth pipes could be installed at, was that the pipe required support all the way to the seabed. This was solved in 1967 by the introduction

of pipelaying under tension (Cox et al., 1967), which along with the introduction of the curved articulated stinger (Langner, 1969) and tensioners, enabled control of the curvature and stresses of the pipeline without support. This marks the transition to second generation S–lay vessels.

Like the first generation, these vessels were barges, but modified with sophisticated equipment for pipe construction and installation, including a complex mooring system was used for station keeping. The S–lay barge spread in this case typically consist of: anchor handling vessels, supply vessels supplying pipe joints, pipe barges for storing pipe joints and tugs. These vessels are the most common, and a large number of these vessels still operate around the world (Guo et al., 2005).

3rd Generation

Moving into the North Sea, with rougher weather conditions than GOM, the second generation pipelay barges suffered large periods of down time. To provide a more stable working environment, less depending on the weather, large semi–submersibles were fitted with basically the same pipelay equipment as the second generation barges, including the anchors for positioning. These semi–submersibles are the third generation S–lay vessels. The first vessel in this generation was the *Viking Piper* constructed in 1975. Few vessels of this generation are still in operation.

4th Generation

For the fourth generation S–lay vessels, dynamic positioning is applied for motion control in stead of the anchors used in the previous generations. The first DP–based pipelay vessel was the Allseas' *Lorelay*, which was introduced in 1985 for deepwater applications (Anonymous, 1987a,b). The vessel was ship–shaped, which gave it a large pipe–carrying capability, and an aft stinger. It quickly proved very successful, particularly in the rough North Sea. The vessel was upgraded in 1996 (Anonymous, 1996), and quickly built up an impressive work record (Anonymous, 1997). The experiences gained from the Lorelay encouraged Allseas to construct the largest pipelay vessel currently in operation, the Allseas' *Solitaire* (Anonymous, 1995; Heerema, 1995, 1998). In 2005, Solitaire was upgraded to further increase her already impressive pipe installing capability, see Figure 2.4 (Knott, 2005; Heerema, 2005; Steenhuis et al., 2007).

Older vessels have been upgraded with DP capabilities, such as the third generation semi–submersible vessel *LB 200*, who was built in the 1970's by McDermott and later acquired by Acergy who upgraded it with a DP system. The vessel was renamed the *Acergy Piper* and operated in the North Sea. In 2004 it went through a major upgrade before installing the gas export trunkline named *Langeled* connecting Norway and England crossing the Norwegian Trench in 2006. In January 2009 the Acergy Piper was sold again, this time to Saipem, who renamed it *Castoro 7* (Castoro 7, 2009).

Figure 2.4: *Solitaire*, the largest S–lay vessel in the world, 300 m (984 ft) excluding stinger. Her S–lay capacity was increased in 2005 to a holding force of 1050 t, enabling her to lay the heaviest pipelines. Courtesy of The Allseas Group.

2.2.2 J–Lay

In deep water conditions the catenary configuration of the pipeline from the seabed to the pipelay vessel is near vertical at the pipelay vessel end. Based on this natural configuration, the pipe leaves the pipelay vessel in a nearly vertical position in the *J–lay* installation method. This eliminates the overbend region from S–lay completely, and the configuration of the suspended pipe resembles the letter *J*. The pipeline is constructed on a vertical ramp, the so–called *J–lay tower*, which is fitted with tensioners and work stations. The angle of the J–lay tower may typically vary between 0° and 15° from the vertical.

J–lay has many advantages (Palmer and King, 2008). The pipe leaves the barge steeply such that the total length of the free pipe is shortened and less applied tension is required for sagbend control. The touchdown point is not as far behind the vessel as for S–lay, due to the lower applied tension, so that positioning of the touchdown is easier, and the pipe can be installed more accurately. Also the complexity involved with a stinger is eliminated. The main drawback with the method is that the tower only facilitates one workstation, making the J–lay method inherently slower than the S–lay method, which is the price paied for pipe

Figure 2.5: *Saipem 7000* owned by Saipem is a semisubmersible crane vessel that has been in operation since 1998. During the winter of 1999–2000 the vessel underwent a refit to enhance its positioning and power systems and add a J–lay system. The J–lay tower can lay pipe from 4" to 32" diameter with a tension of up to 525 tonnes (5.15 MN) using the tensioners and up to 2,000 tonnes (20 MN) when using friction clamps. Courtesy of Saipem SpA.

installation at greater depths. The added weight high up on the vessel has an adverse effect on stability, and semi–submersibles are frequently used to facilitate J–lay due to their high stability. The method is not applicable in shallow water.

The first dedicated J–lay installation facility was installed on the DP derrick barge *DB 50*, owned by J. Ray McDermott in the 1992. Since 1998 several vessels have been fitted with J–lay capabilities. Two of the largest are the vessel *Saipem 7000 (S–7000)* that was fitted with a J–lay tower in 1999 (Faldini, 1999), see Figure 2.5 and *Balder* who was modified in 2001.

Numerous papers are published on the J–lay method. A historic review on the development of the J–lay method, and the set of system requirements are provided in Wilkins (1994). Technical aspects advocating for J–lay in deepwater installation are discussed by Choi and Jo (1999). A review of lessons learned from applying the method are described by Cavicchi and Ardavanis (2003). The S–lay and J–lay installation methods are often seen as complementary methods (Perinet and Frazer, 2007).

2.2.3 Reeling

One of the most efficient installation methods is the *Reel Vessel Method*, which is suitable for cables, umbilicals and flexible pipes, which generally have small diameters, and small–diameter rigid pipes (up to 16 inches). The pipe is constructed onshore in a controlled factory environment and spooled onto a large diameter reel fitted on the reeling vessel at a so–called *spooling–base*. Depending on the pipe diameter, the reel capacity is typically several miles of pipe. The loaded vessel then travels to the installation site where the pipe is installed by unspooling as the vessel moves. Reeling barges commonly has a horizontal reel and the pipe is paid into the ocean over a stinger similar to S–lay, while ship shaped reeling vessels has a vertical reel and a tower to accommodate a J–lay type installation. The pipe experience very large strains when it is spooled onto the real, often in the range of 2%, which requires that the pipe is mechanically straightened out during the installation.

The first dedicated reeling vessel was the barge *RB–2*, built in 1970 for the Flour Corporation. Currently, the vessel has been renamed *Chickasaw* and it is still in operation, now owned by Global Industries (Chickasaw, 2009). The first sea–going reeling vessel was the Apache, built in 1979 and currently owned by Technip. Technip announced in 2009 that the the Apache will be completely rejuvenated and reappear with improved capabilities as a new vessel, the *Apache II* in 2010 (Apache II, 2009). Before this rejuvenation, the Apache has completed over 400 pipelay projects. The current stat–of–the–art reeling vessel for deepwater rigid pipelay is the *Seven Oceans*, owned by Subsea7 and delivered in 2007, see Figure 2.6 (Seven Oceans, 2009).

2.3 Dynamic Positioning

Controlling the position and motion of a pipelay vessel is crucial for the success of a pipelay operation, since it is used to position the touchdown point, and to limit and control the loads on the pipe. If the pipelay vessel drifts sideways or rotates, the pipe will experience large bending in the region where it lifts off from the stinger, and may easily buckle and kink.

The first generation of pipelay barges were held in place by an anchor–mooring system, where anchors were placed in a spread formation by anchor handling vessels. The position and orientation of these barges could then be kept to avoid buckling and kinking of the pipe, and the barge moved forward by controlling the anchor–line winches.

However, positioning by mooring has several disadvantages (Palmer and King, 2008). The mooring lines radiate from the pipelay vessel in a full circle of directions, such that in congested areas it becomes difficult to place the anchors while keeping clear of existing structures, including the already installed pipe. Deep waters also limit the precision of the positioning due to the mechanical flexibility of the mooring system. Finally, the initial positioning and subsequent relocation of anchors is cumbersome, time consuming, and sensitive to weather conditions and sea states.

Due to such mooring–related constraints, the advantages of *dynamic positioning*

Figure 2.6: *Seven Oceans* owned by Subsea 7 is a pipelaying– and offshore construction vessel, delivered in 2007, capable of installing 16 inch pipelines in depths reaching 3000 meters. Huisman–Itrec *(www.huismanequipment.com)* designed and built the complex pipelay installation on the ship. Behind the superstructure a reel with a weight of 950 tonnes has been integrated in the ship. This reel can store up to 3500 tonnes of rigid steel pipe. Courtesy of Subsea 7.

(DP) for position control of pipelay vessels was early recognized. Dynamically positioned pipelay vessels keep their position exclusively by active use of thrusters, and fully actuated vessels are required for precision positioning in surge, sway and yaw, see Figure 2.7. Background on DP systems is found in (Bray, 2003; Fossen, 2002; Faÿ, 1990), while a DP system reference manual can give a hands–on introduction (Kongsberg, 2006). The pipelay vessel must also keep a specific heading, and may not freely weathervane in order to reduce the impact of the environmental loads. Tug–boat support may occasionally be used to keep position if the thruster capacity becomes insufficient. A DP vessel has a considerably shorter start–up time, and has the ability to abandon and recover pipelines quickly. The motion control becomes independent of water depth and the vessel can operate in congested areas and close to platforms. There is also less mechanical downtime for a DP vessel compared to an anchor vessel because the wear and tear on an anchor system is more intense.

However, two factors have historically worked against the employment of DP

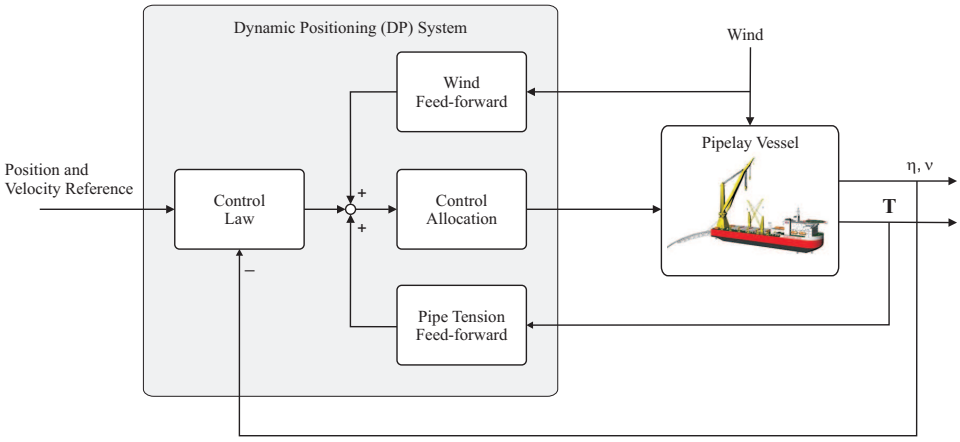

Figure 2.7: A typical pipelay DP system architecture, including position and velocity feedback and feedforward for wind and pipe tension $\boldsymbol{T}$.

technology in pipelay operations, namely the *reliability of the system*, since system failure potentially causes severe damages to both pipeline and vessel, as well as the *power required to balance the tension from the pipe*. Still, despite the initial reluctance to use DP systems, all newly commissioned pipelay vessels today are dynamically positioned. To ensure reliability, these vessels are usually configured to IMO Equipment Class 3, with full redundancy in all components. Older vessels are commonly retrofitted with class 2 equipment.

In a commercial off–the–shelf (COTS) DP system, see Figure 2.7, the generalized vessel position $\boldsymbol{\eta}$ and velocity $\boldsymbol{\nu}$ are controlled to a reference position and velocity. In practice, a DP operator (DPO) manually operates the DP system based on experience and know–how, using specific features that have been developed to aid in pipelay operations (Kongsberg, 2006). Such features include *tension compensation*, *pipe–pull* (i.e., move forward one pipe length at a time), and *tracking of vessel path*, where the dynamics of the pipe and environmental loads are compensated for by using a crab angle and track offset. However, the technology implemented in commercial DP systems, including pipelay–specific extensions, is classified and not easily accessible for academic researchers.

The actual installation process is always overseen by an engineer, who operates the vessel together with the captain. The engineer relies on a team of three to four people, where each team member has a dedicated task of monitoring or operating equipment. A typical task breakdown may be:

- Navigation (Surveyor)
- Vessel maneuvering (DPO)
- Tensioner/reeling/carousel operator
- ROV operator.

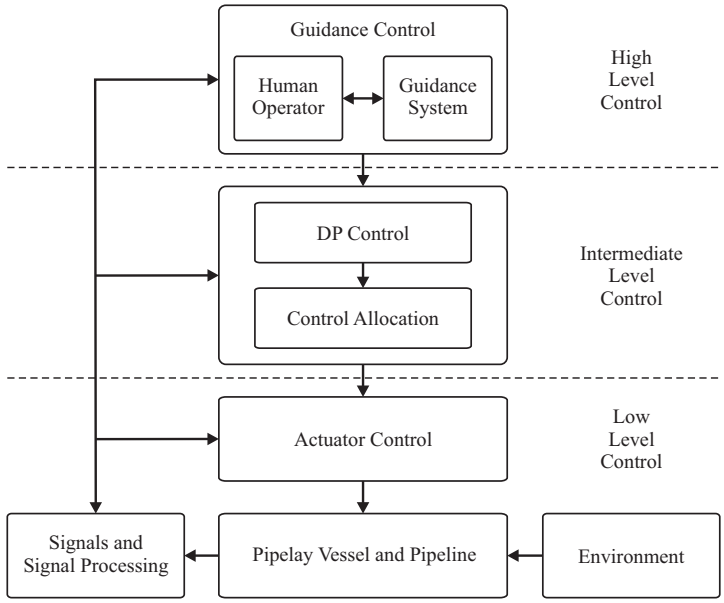

Figure 2.8: Motion control hierarchy. Adopted from (Breivik and Fossen, 2008).

The positioning of the vessel is done by a DP system, where reference positions are manually provided such that the vessel moves in a discrete fashion between consecutive references. The distance between these reference positions may vary in length, but the pipelay vessel will typically move in steps equal to the length of a pipe extension, which is limited by the length of the firing line. However, a reeling ship typically moves continuously since it can reel out its pipe continuously.

2.4 Motion Control Issues

The preceding sections have addressed how to install a pipeline safely on the seabed, by addressing pipeline construction and installation methods as well as vessel motion control. This section will address the issue of installing the pipeline *along the prepared path* on the seabed, which has been decided for it in the design phase, and prepared by seabed intervention work prior to the installation. The available actuators during the installation to complete this task is limited to the vessel motion control system and the pay–out speed.

A vehicle motion control system can be conceptualized to involve at least three levels of control in a hierarchical structure as illustrated in Figure 2.8 (Breivik and Fossen, 2008). The highest control level, termed the *guidance level*, is responsible for prescribing vessel guidance commands to position the touchdown point on the seabed. The intermediate level then encompass COTS DP controllers, which give commands through a control allocation algorithm to the low–level actuator controllers that manipulate the actual vessel propellers and thrusters.

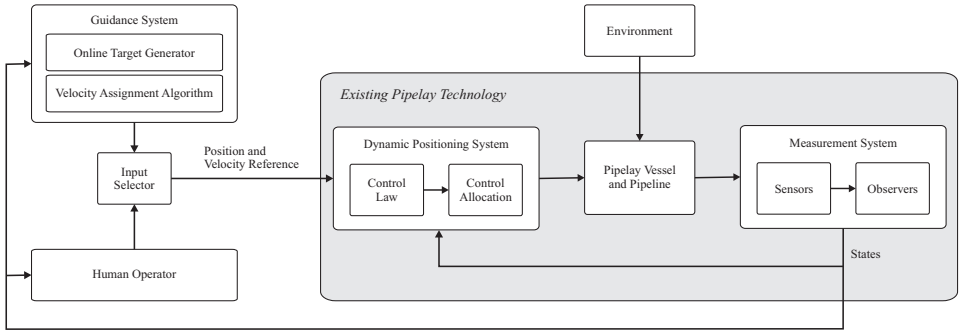

Figure 2.9: A typical pipelay DP system architecture, including pipe tension feedforward.

An objective of this section on motion control is to show the advantage of, and to motivate the design of guidance systems that can automate several of the tasks in pipelaying operations, which are currently carried out by the human DPO at the highest control level in Figure 2.8, as illustrated in Figure 2.9. Such guidance systems can conceptually be divided into an *online target generator* and a *velocity assignment algorithm*. While the target generator computes the virtual target point on the sea surface which the pipelay vessel must track for the touchdown point to follow the seabed reference path, the velocity assignment algorithm computes the associated reference velocity. Both reference position and velocity are subsequently fed to a COTS DP system.

At least two distinct approaches can be taken in the guidance system design:

1. In a *protocol–based* approach, the system tries to imitate a human operator based on a set of rules obtained from quantifying the operational procedure which the operator follows. The system is then implemented as a flow diagram, which is simple to implement, but which at best will perform the task only as well as the human operator.

2. In a *model–based* approach, the system computes the guidance signals based on mathematical models of the pipelay system. The great advantage of a model–based controller is the available computational power, which allows for computation of decision data based on real–time measurements, thus yielding more accurate results than data based on test scenarios. The performance of a model–based guidance system can thus potentially exceed that of a human operator. This motivates the development of the pipe models developed in Chapters 5 and 6.

Note that in this scenario the human operator is still a part of the system, but now only left to monitor the operation.

2.4.1 The Pipelay Problem

The overall objective of a pipelay operation is to position a pipeline along a desired seabed path from a start point to an end point while simultaneously ensuring pipeline integrity. All motion controllers try to achieve a control objective, and for pipeline installation the main control objective can be stated as:

Definition 2.4.1 ***The Pipelay Problem*** *The pipelay problem is defined as the task of laying a pipeline along a pre–specified reference path on the seabed through active motion control of a pipelay vessel, subject to varying environmental loads. The structural integrity of the pipe must be guaranteed at all times during the operation.*

The primary objective of the pipelay problem is thus to position the touchdown point as close as possible to the reference path on the seabed. A secondary objective can then be to move the touchdown point at a desired speed along this path. Thus, the touchdown point faces a so–called *path–maneuvering problem*, see (Breivik and Fossen, 2008) and (Skjetne et al., 2004). These two objectives must be satisfied such that the structural integrity of the pipe is ensured. Hence, the surface vessel must move such that both the path–maneuvering objective of the touchdown point, $\boldsymbol{p}_{td}$, and the pipe structural integrity is satisfied simultaneously. The pipelay vessel DP system must then track an instantaneously computed reference value for the vessel position, $\boldsymbol{p}_{tm}$, to achieve both objectives, and thus satisfy a *target–tracking* motion control objective, see Figure 2.11 (Breivik and Fossen, 2008). This objective corresponds to motion control scenarios where the target motion is not known apriori, which is the case for our application since the target is dynamically computed based on $\boldsymbol{p}_{td}$, $\boldsymbol{p}_{tm}$, U_p, environmental conditions, and a desired tension. Hence, the surface vessel must achieve target tracking for $\boldsymbol{p}_{tm}$ such that $\boldsymbol{p}_{td}$ satisfies its path–maneuvering objective. An analogous application can be found in (Sørensen et al., 2001), where a DP–controlled semi–submersible must chase a virtual setpoint on the sea surface to minimize bending stresses on a riser extending from the vessel to a stationary installation on the seabed. The pipelay problem can thus be seen as a dynamic version of this setpoint chasing application.

Note that the pipelay problem definition is independent of pipe diameter, water depth, installation method, departure angle, and whether an automatic controller is used or not.

The concept of velocity assignment can be illustrated through a simplified *speed controller* in 1 DOF for computing the desired surge speed u_d as

$$u_d = \underbrace{U_p \cos(\mu)}_{Feedforward} \underbrace{+ k_p (T_d - T) + k_i \int_{t_0}^{t} (T_d - T) d\tau}_{Feedback} \tag{2.1}$$

where T_d is the desired tension, μ is the slope of the seabed, and $k_p, k_i > 0$ are controller gains. The first term is a feedforward term for the pay–out speed with compensation for the seabed slope, while the next terms provide tension feedback.

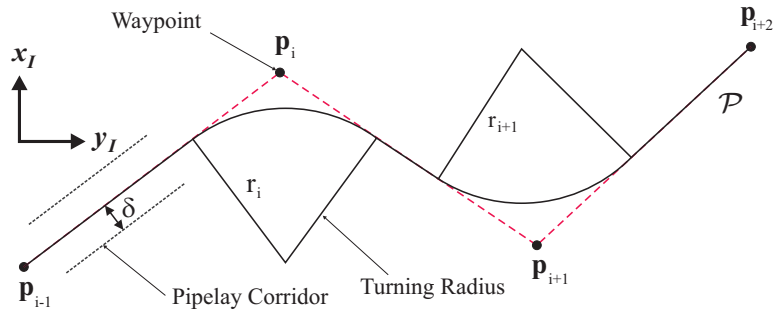

Figure 2.10: Subsea path parameterization.

The feedback part of (2.1) becomes a *tension compensation* PI–controller, used for station keeping for $U_p = 0$, i.e., to facilitate pipe joint welding.

Alternatively, the vessel speed can be set to a constant, and U_p controlled to achieve a desired lay–tension. This procedure is called *render*, and is used for reeling.

2.4.2 Subsea Path

Let the subsea path $\mathcal{P}$ consists of a finite set of n straight–line segments connecting $n-1$ waypoints, each with an associated turn radius r_i, $i \in \{1, \ldots, n\}$, organized in a waypoint table. The location of each waypoint is given by the position vector $\boldsymbol{p}_i \in \mathbb{R}^3$, stated relative to an inertial Earth–fixed reference frame. The turn radii ensures a smooth transition between consecutive line segments, and the path $\mathcal{P}$ is thus implicitly parameterized as a set of connected straight and curved segments, see Figure 2.10. Only one segment is in active use at a time.

Let $\mathcal{D}$ then define the part of the seabed which is located within a distance $\delta > 0$ of $\mathcal{P}$, coinciding with the breadth of the seabed preparations, done, e.g., by trenching, dredging, or rock dumping. Depending on the seabed conditions, this corridor has a typical width of 1-10 meters.

During pipelay, the goal is to have $\boldsymbol{p}_{td} \in \mathcal{D}$, and for $\boldsymbol{p}_{td} \notin \mathcal{D}$, a fault condition has occurred which must be corrected. A switching between the nominal and some fault–recovery controllers must then be performed to ensure that the situation is properly handled such that the pipe can be placed within $\mathcal{D}$ again. The field of *fault–tolerant control* deals with such scenarios (Blanke et al., 2006).

2.4.3 Vessel Path

Representing the vessel position by $\boldsymbol{p}_{tm}$, a nominal vessel path $\mathcal{V}$ can be found by purely kinematic considerations, which is valid under the following assumptions: Dynamic effects can be neglected due to low speeds, no environmental loads, and the water depth is constant for each segment, see Figure 2.11.

Let the position of a point on $\mathcal{P}$ be represented by $\boldsymbol{p}_{td}(\varpi) \in \mathbb{R}^2$, where $\varpi \in \mathbb{R}$ is a scalar variable. For straight–line segments (zero curvature), the desired vessel

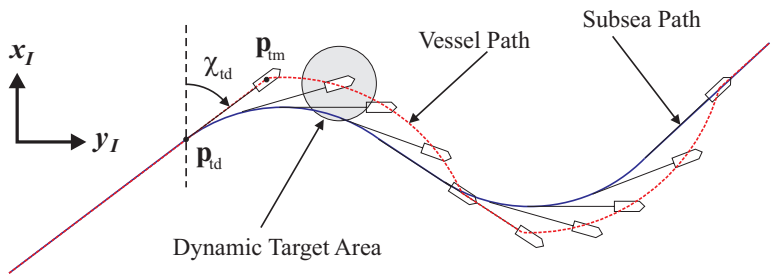

Figure 2.11: Subsea Path and corresponding vessel path.

position can then be computed by

$$\boldsymbol{p}_{tm}(\varpi) = \boldsymbol{p}_{td}(\varpi) + \boldsymbol{R}(\alpha_i) \begin{bmatrix} \|\boldsymbol{p}_{tm}(\varpi) - \boldsymbol{p}_{td}(\varpi)\|_d \\ 0 \end{bmatrix}, \tag{2.2}$$

where

$$\boldsymbol{R}(\alpha_i) = \begin{bmatrix} \cos(\alpha_i) & -\sin(\alpha_i) \\ \sin(\alpha_i) & \cos(\alpha_i) \end{bmatrix} \in SO(2), \tag{2.3}$$

and

$$\boldsymbol{p}_{td}(\varpi) = \begin{bmatrix} x_i + \varpi\cos(\alpha_i) \\ y_i + \varpi\sin(\alpha_i) \end{bmatrix}, \tag{2.4}$$

where $\|\boldsymbol{p}_{tm}(\varpi) - \boldsymbol{p}_{td}(\varpi)\|_d$ is the desired touchdown distance corresponding to a desired pipeline tension, and α_i is the orientation of the straight–line subsea path. For subsea segments with varying curvature, the vessel position can be computed by

$$\boldsymbol{p}_{tm}(\varpi) = \boldsymbol{p}_{td}(\varpi) + \boldsymbol{R}(\chi_{td}(\varpi)) \begin{bmatrix} \|\boldsymbol{p}_{tm}(\varpi) - \boldsymbol{p}_{td}(\varpi)\|_d \\ 0 \end{bmatrix}, \tag{2.5}$$

where $\boldsymbol{p}_{td}(\varpi)$ now depends on the particular path, and $\chi_{td}(\varpi)$ is the tangential direction of the curved subsea path at ϖ, see Figure 2.11.

2.4.4 Vessel Target

The kinematically computed vessel paths associated with (2.2) and (2.5) were reported to be satisfactory for installation in the shallow GoM. However, they do no longer suffice in a practical pipelay operation. They only provide approximations that are valid for ideal operating conditions, including nice weather and minimum current. In practice, the vessel must track a dynamic target located at a distance from the ideal location in order for $\boldsymbol{p}_{td}(\varpi)$ to be within $\mathcal{D}$ while simultaneously ensuring pipeline structural integrity, see Figure 2.11. Today, this target is manually computed by a DPO based on previous experience through various offset parameters available in the DP system. A future goal is thus to automate this by computing this target value dynamically based on mathematical models and real–time measurements. An even greater degree of accuracy and effectiveness in the pipelay operation may then be achieved.

2.5 Standards

The design and installation of pipelines must comply with established standards. The objective of these standards are to ensure safety, and to specify the minimum requirements to be satisfied by any designer. To ensure the validity and usability of a standard, it is important that new research achievements and experience gained from the most challenging pipeline projects recently executed are reflected. Probably the most used standard, at least in the North Sea, is the DNV–OS–F101 by Det Norske Veritas (Det Norske Veritas, 2000). This code employ a design practice based on so–called *limit states* for the pipeline design. In the limit–state design, all relevant failure modes for a pipe are formulated as limit states, which are classified into one of the four categories:

1. Serviceability Limit State (SLS),
2. Ultimate Limit State (ULS),
3. Fatigue Limit State (FLS),
4. Accidental Limit State (ALS).

The limit state is the limit between an acceptable and unacceptable condition expressed in mathematical terms derived through simplified design formulas for a given failure mode. The limit state design identifies the different failure modes and provides specific design checks to ensure structural integrity. The pipeline capacity is then characterized by the actual capacity of each individual failure mode. For more on limit state design in the DNV–OS–F101, see Mørk et al. (1998).

Other standards and recommended practices related to offshore pipelines are:

- API RP 1111 API (1998),
- ISO 13623 ISO (2000),
- BS 8010 BS (1993).

2.6 Measurements

The condition of the pipe is closely monitored during the pipelay operation by a measurement system that provides state measurements from filtering of sensor data and from state estimators. The instrumentation varies with different vessels based on size, operational depth and installation method, and the following measurements are considered here:

1. Vessel position and velocity
2. Touchdown position
3. Axial tension
4. Departure angle

5. Roller pressure
6. Distance to last roller
7. Free–span pipe length
8. Touchdown distance
9. Water depth
10. Environmental loads (current, wind, waves).

Vessel position and velocity

The vessel position may be obtained with high accuracy from a number of available position reference systems, including the global positioning system (GPS), hydroacoustic position reference (HPR) and microwave position reference systems (Bray, 2003). Since pipelaying is done over long distances, using GPS with corrections (DGPS) is very common and provides an accuracy of up to 0.1 meters. GPS can also provides vessel velocity measurements, however, DP systems commonly applies an observer to compute the vessel velocity.

Touchdown position

A remotely operated vehicle (ROV) is used to hover over the touchdown point and provide a visual image. It is not easy to define the exact touchdown point since the seabed is uneven and penetrable, so the position of the touchdown point $\boldsymbol{p}_{td}$ is commonly assumed to coincide with the ROV position. Multiple ROVs may also be used to monitor other parts of the pipe in the water.

Axial tension

The purpose of applying tension to the pipeline through tension machines is to control the curvature of the sagbend and the moment at the stinger tip through supporting the submerged weight of the suspended part of the pipe. The tension exerted on the tensioners from the pipe depends on the pipe properties and configuration.

Departure angle

The departure angle of the pipe leaving the stinger is estimated from the contact force on the rollers and/or closed–circuit television (CCTV) equipment on the stinger. An equivalent term is *lift–off angle*.

Roller pressure

Rollers are spaced out along the stinger, supporting the overbend and reducing the strain. The rollers are equipped with pressure cells to measure the contact force from the pipe. Theses measurements are used to ensure that the pipe follows the

stinger smoothly, and good practice indicates that the pipe should lift off from the stinger before the last roller. CCTV equipment may also be used for this purpose.

Distance to last roller

Frequently, the pipeline is required to lift off before the last roller on the stinger. Hence, monitoring in this area is of importance, and laser measure or similar device can be used to measure this distance.

Free–span pipe length

Since each link joint is numbered sequentially, visual identification of the joints at the touchdown point and at the vessel means that the length of the suspended pipe L can be found.

Touchdown distance

The touchdown distance is the horizontal distance between $\boldsymbol{p}_{tm}$ and $\boldsymbol{p}_{td}$, also known as the *lay–back* distance.

Water depth

Measurements of the water depth are readily acquired from acoustic sensors located on the pipelay vessel. At the touchdown point, the ROV will measure its depth using pressure sensors.

Environmental loads

Wind will influence the vessel position, but the direction and speed of the wind is easily measured and compensated for by the DP system. Currents and second–order wave loads can also be accounted for by the DP system. Loads that can not be avoided or compensated for are first–order wave effects.

Chapter 3

Pipelaying Mechanics

The structural analysis of an offshore pipeline under construction and installation deals with the computation of deformations, internal forces, and stresses as a result of external loads and the structural properties of the pipe. A short pipe section, like a single pipe joint appears to behave much like a rigid body, whereas a long pipe of several hundred meters is very elastic and behaves almost like a string. Hence, the pipe string behavior is highly dependent on the water depth. For the structural analysis, it is seen to function as a continuous beam, a tension member, a compression member, a pressure pipe, an externally loaded conduit, and a suppression element. The static and dynamic loads due to the construction methods and the environment are numerous and varied (Small, 1970).

Structural analysis of pipelines experienced a significant increase in importance in the late 1960's and 1970's, when offshore oil development moved into deeper waters and more hostile environment. Simple approximations and rules of thumb used in the 1950's and early 1960's were no longer adequate, and more complex methods had to be designed. This progress brought with it new and more complex problems in structural evaluation and analysis.

Structural deformation of the pipe during construction depends on the method and equipment used for installation, the structural properties of the pipe and the environmental loads. In this chapter we consider the loads on the pipeline, and how these loads control the deformation of the pipe. The effects of the marine environment, and the pipelay vessel are also considered. The pipelay mechanics presented in this chapter is the basis for the nonlinear dynamic pipe models developed in later chapters.

3.1 Pipeline Configuration

The static configuration of the pipeline during the pipelay operation depends on the installation method. For the S–lay method, the configuration is governed by the following parameters (Bai and Bai, 2005):

1. Tension at the pipelay vessel,

2. radius of curvature for the stinger,
3. roller positions,
4. departure angle form stinger,
5. pipe weight,
6. pipe bending stiffness,
7. water depth.

The material properties of the pipe, such as e.g., pipe diameter, wall thickness, weight, bending and axial stiffness are determined in the design phase of a pipeline project to meet the operational needs for the pipeline. Once the pipe material properties are determined, a static pipeline installation analysis is performed. This analysis essentially forms a check on the pipelay vessel equipment capabilities. It is used to compute the *pipelay parameters*, which are the optimal stinger radius, stinger departure angle, roller box height, and initial tension of the pipeline. It is also used to check that the stresses and strains of the configuration is within acceptable limits. Hence, the tension at the pipelay vessel is the only parameter that can be manipulated during the installation, as the departure angle is a function of the tension, and the water depth is a function only of the position along the subsea path. The axial tension in the pipe has a vertical and a horizontal component. The vertical component is dictated by the water depth and the pipe weight, and passively compensated for by the pipelay vessel restoring forces. Hence, only the horizontal tension is left to active control by the vessel motion control system.

The deformation of the pipeline from the stern of the pipelay vessel to the seabed, the so–called *configuration*, for an S–lay operation is geometrically split in two sections, namely the *overbend* and *sagbend*, with the addition of an *intermediate* region, see Figure 2.3, (Perinet and Frazer, 2008).

3.1.1 Overbend Region

The overbend is the fully supported region from the tension equipment over the stinger and to the stinger tip. The radius of curvature is beneath the center of the pipeline. The stinger supports the pipe on rollers spaced out along its length, which fully controls the pipe geometry and curvature. The roller contacts are monolateral and can be considered a boundary condition to the achievable possible configuration of the pipeline. From the third roller counted from the tip and up, the pipe is *displacement–controlled* (Callegari et al., 2000). The stinger radius yields a certain overbend strain, and this strain has to be checked against allowable strain levels in international codes such as e.g., DNV OS–F101. One of the concerns arising from high overbend strains is potential rotation of the pipe during installation and consequent twisting on the seabed, so–called *cork–screwing* (Heerema, 2005). Note that the local loads on the stinger do not propagate beyond the inflection point, and also that the J–lay method does not have an overbend region.

3.1.2 Sagbend Region

The sagbend is the free span region that extends from the end of the stinger to the touchdown point. The radius of curvature is now above the center line of the pipe. In the sagbend, the static load effect is governed by the tension, pipe submerged weight, external pressure and bending stiffness. The equilibrium configuration is load–controlled since there are no physical boundaries for the deformations that the pipeline can experience, so that the configuration in the sagbend is essentially the same for every deepwater installation method.

3.1.3 Intermediate Region

The intermediate region is the short section between the lift off point from the stinger and the inflexion point. The curvature is still on the stinger in this region, but not fully supported. Since the extent of this region can be difficult to determine, sometimes the *stinger–tip region* is used, which is defined as the pipe section that extends from the third–last stinger roller and down to the inflection point. This region is sometimes considered separately since the dynamic load effect caused by the contact of the pipe with the last roller can cause very high and uncontrolled dynamic bending loads. Consequently, the pipe lift off from the stinger is usually required to occur before the last roller (Callegari et al., 2000; Torselletti et al., 1999).

3.2 Pipelay Tension

Following from the previous chapters, the pipelay tension is the most significant parameters to control in order to successfully solve the control problem defined as the pipelay problem in Definition 2.4.1. Before considering the mathematical details on computing tension, we will in this section compare the tension that has to be compensated by the vessel motion control system for the S–lay and J–lay methods, respectively.

3.2.1 Comparing S–lay and J–lay

Consider two pipelines with identical properties installed by the S–lay and J–lay method, respectively, where the lift off angle θ is the same in both cases, see Figure 3.1. In the J–lay case, the shape of the pipe is a catenary. For static equilibrium, the axial tension T at the lift–off point can be decomposed in a vertical and a horizontal component,

$$H = T\cos(\theta), \tag{3.1}$$

$$V = T\sin(\theta), \tag{3.2}$$

where θ is the lift–off angle, and this also yields the relation

$$T = \sqrt{H^2 + V^2}. \tag{3.3}$$

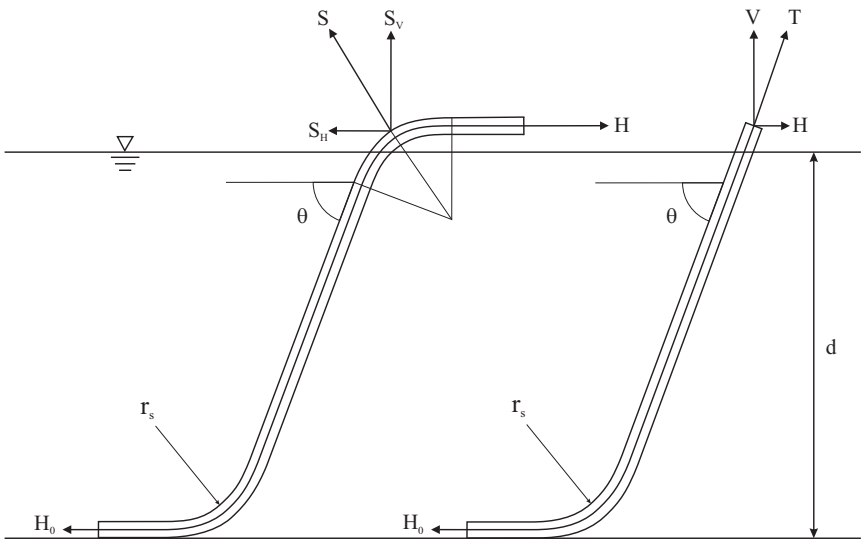

Figure 3.1: Comparing tension components for S–lay and J–lay equilibrium configurations. Adopted from Perinet and Frazer (2007).

At equilibrium, there are no external forces applied in the horizontal direction,

$$H + H_0 = 0, \tag{3.4}$$

while H_0 is the horizontal tension at the touchdown point. For a submerged pipe, the vertical tension is directly related to the length of the suspended pipe L and the pipe submerged unit weight w_s, as

$$V = w_s L. \tag{3.5}$$

From Irvine (1981) the tension at the top point of the pipe is

$$T = H + w_s d, \tag{3.6}$$

where d is the dip or sag of the pipe, which is the water depth at the touchdown point. Hence, in the J–lay case, the vessel positioning system must counteract H. For the S–lay case, the stinger acts on the pipe with force S, such that the vessel positioning system must counteract the sum of the bottom tension and the horizontal component of stinger reaction forces S_H. Hence, the tension compensation in the S–lay method is larger than for the J–lay method when other parameters are the same (Perinet and Frazer, 2007).

The lay–tension T is governed by the difference in $\mathbf{p}_{td}$ and $\mathbf{p}_{tm}$, which are the position of the touchdown point and the position of the last tension machine along the firing line, and the length of the pipe in between. For the static planar case, and where the axial tension dominates the bending stiffness of the pipe, this situation can be well represented by the natural catenary equation, which will be

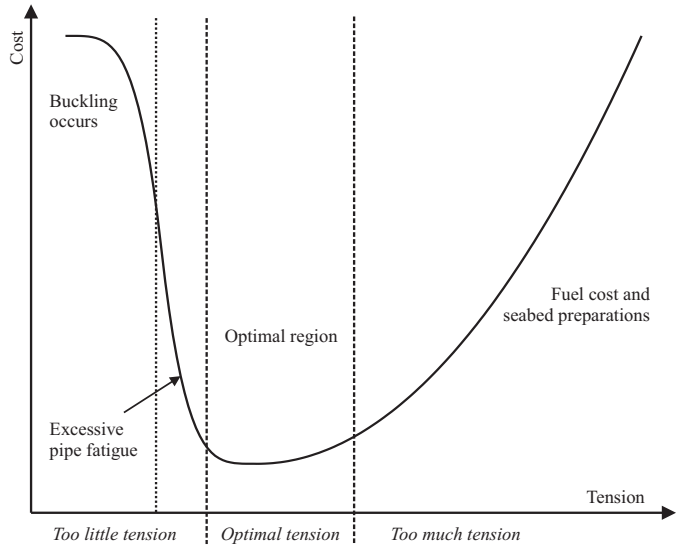

Figure 3.2: Tension vs. cost.

investigated further in Chapter 4. Also, since pipelaying is a low–speed application, catenary considerations may give good lay–tension approximations, if the dynamic loads can be neglected.

3.2.2 The Optimal Pipelay Tension

There are several reasons to keep low horizontal tension at the touchdown point. Low tension will reduce free spans and also allows for shorter radii of the curved segments, which will reduce the need for seabed preparations. The ROV used for monitoring the touchdown point has a limited range, and low horizontal tension will move the touchdown point closer to the pipelay vessel so that the ROV can be operated from this vessel. Reduced tension also reduces the fuel consumption of the surface vessel. The residual tension, which is the tension left in the pipe after installation, is also reduced with reduced lay tension, and should be as small as possible for most installations. However, too little tension will cause the pipe to buckle. Excessive tension can be detrimental to the pipe in the overbend, ovalizating or plasticizing the pipe. Most pipelines are installed empty to reduce the required tension. A graph of tension vs. cost is shown in Figure 3.2.

If the static analysis indicates that the pipelay vessel or the pipeline will be close to its limits, a dynamic analysis is performed to account for the dynamic effects, e.g, vessel dynamics, waves and current, or accidental loads, e.g., pipe flooding due to a buckle, that may influence the pipelay tension. Such a dynamic analysis is mostly done for deepwater operations, since they are usually costly and time consuming, but is good for an operability analysis, which indicates what environmental conditions the pipe can safely be installed in.

The tension becomes a dynamic parameter during installation, that is affected

Table 3.1: Loads on submarine pipelines categorized according to source, and classified as static or dynamic, indicated by **S** and **D** respectively. Adopted from Small (1970)

	Gravitation	Environment	Construction	Operation
Weight	S			
Buoyancy		S,D		
Drag Force		S,D	D	
Lift Force		S,D		
Inertial Force		D	D	
Tension			S,D	S,D
Compression	S		S,D	S
Torsion			S,D	
External pressure		S		
Internal pressure				S,D

by environmental loads and by the boundary conditions of the pipeline. The lower boundary condition is given by the position and orientation at the touchdown point, while the upper boundary condition is given by the position and orientation of the pipelay vessel.

3.3 Pipeline Installation Loads

The loads acting on a pipeline can be classified as *static* or *dynamic*, and be categorized according to source, i.e., *gravitational*, *environmental*, *constructional* and *operational*, following Small (1970), see Table 3.1. The loads vary in magnitude, direction, frequency and intensity. Some can be established with great accuracy, while others must be estimated. In the following, attention is limited to the loads that are of importance during the pipelay, which are related to *tension*, *bending*, *pressure*, and *contact forces* perpendicular to the pipe axis at the support on the stinger and the sagbend (Bai and Bai, 2005).

3.3.1 Elastic Beam Theory

To comply with the structural integrity requirement of the pipelay, as defined in Definition 2.4.1, the pipe deformations during the pipelay should be *linear elastic* once the pipe has left the stinger of the pipelay vessel. For an *elastic deformation*, internal forces of bending, twisting and shearing arise to counteract applied external forces, allowing the body to assume a new equilibrium state. If the applied forces are removed, the body will return to its original undeformed state. If the external forces exceeds the internal forces, a permanent deformation of the object,

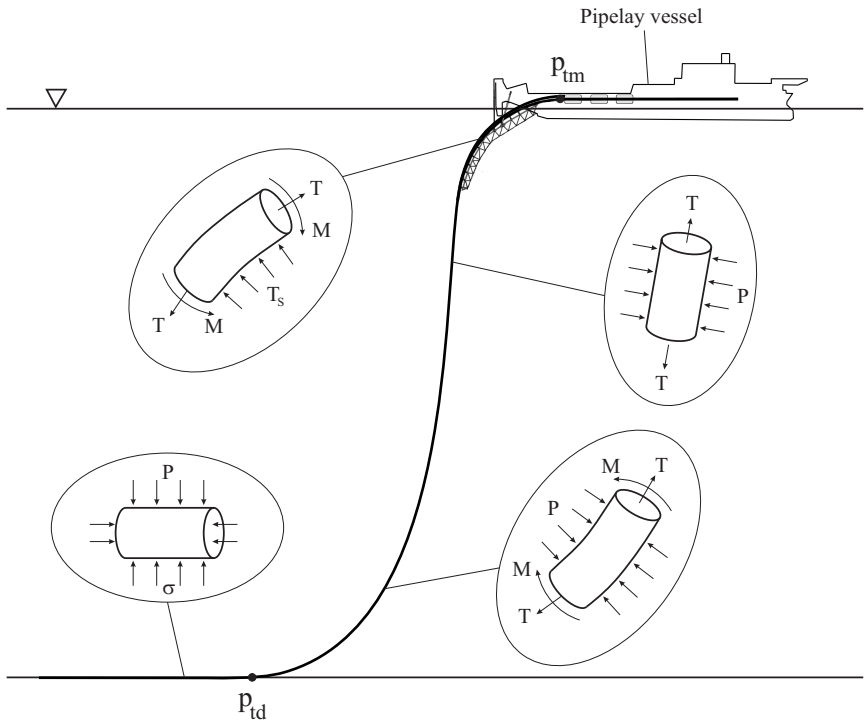

Figure 3.3: Loads on the equilibrium configuration for S–Lay pipe construction. On the stinger, the pipe in subject to tension T, bending moment M, and the contact force from the stinger T_s. Freely suspended in the wate, the pipe is subject to external pressure P. Gravity and buoyancy is not indicated in the figure. Resting on the seabed, a seabed force counteracts gravity forces.

so–called *plastic deformation*, or even structural failure occurs. For pipelines this is frequently known as *buckling*.

Hence, we will limit our attention to linear elastic deformations, that are governed by *Hooke's law*. This law linearly relates *stress* σ and *strain* ε of a deformation, and can be stated as

$$\sigma = E\varepsilon, \tag{3.7}$$

where E is Young's modulus. Strain is the relative amount of deformation, which is a measure of how much a given displacement differs locally from a rigid–body displacement. Strain is dimensionless, while Young's modulus and stress have dimension pressure. Several quantities for measuring the strength of a material arise in the generalized Hooke's law:

- *Young's modulus* E – describes the material's response to linear strain, the so–called *stiffness*. Stiffness is the resistance of the elastic body to this deformation.

- *Shear modulus* G – describes the material's response to shearing strains, which

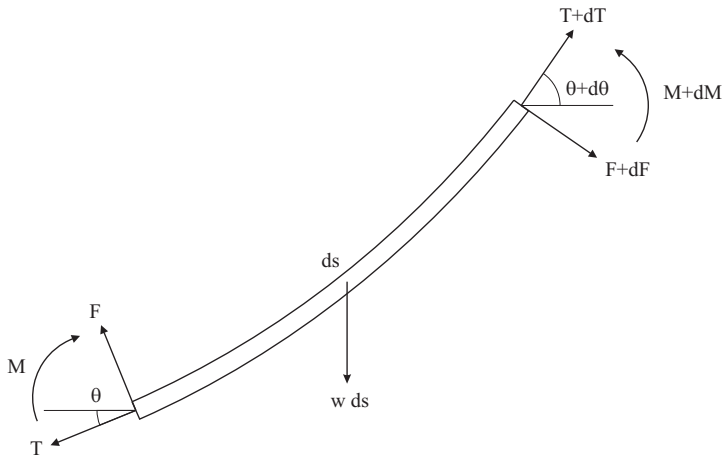

Figure 3.4: Equilibrium of forces on a catenary element of length ds.

occurs when a body experiences a force parallel to one of its surfaces while its opposite face experiences an opposing force.

- *Bulk modulus* K – describes the material's response to uniform pressure.

The bending stiffness EI of a beam relates the applied bending moment M to the resulting deflection of the beam, and given by

$$EI = \frac{M}{\kappa}, \tag{3.8}$$

where I is the area moment of inertia of the beam cross–section, and κ is the resulting curvature of the beam.

Assume that the pipe has uniform cross–sections and weight distribution along its length, then the governing equations for the pipe can be found by considering the static forces on a short segment of the tensioned pipe at equilibrium, see Figure 3.4. The equilibrium of forces in the horizontal direction x, and vertical direction y yields, respectively

$$\begin{aligned}(T+\delta T)\cos(\theta+\delta\theta) - T\cos(\theta)& \\ +(F+\delta F)\sin(\theta+\delta\theta) - F\sin(\theta) &= 0, \end{aligned} \tag{3.9}$$

$$\begin{aligned}(T+\delta T)\sin(\theta+\delta\theta) - T\sin(\theta)& \\ +(F+\delta F)\cos(\theta+\delta\theta) - F\cos(\theta) - w_s\,\delta s &= 0, \end{aligned} \tag{3.10}$$

where w_s is the unit weight of the pipe. Replacing small changes in values δ by the differential operator, and the approximation

$$\cos(\theta+\delta\theta) \approx \cos(\theta) - \sin(\theta)\ \delta\theta, \tag{3.11}$$

$$\sin(\theta+\delta\theta) \approx \sin(\theta) + \cos(\theta)\ \delta\theta, \tag{3.12}$$

which are valid for small values of $\delta\theta$, (3.9) and (3.10) become

$$-\left(T\sin\left(\theta\right)-F\cos\left(\theta\right)\right)\mathrm{d}\theta+\mathrm{d}T\cos\left(\theta\right)+\mathrm{d}F\sin\left(\theta\right)=0, \tag{3.13}$$

$$\left(T\cos\left(\theta\right)-F\sin\left(\theta\right)\right)\mathrm{d}\theta+\mathrm{d}T\sin\left(\theta\right)-\mathrm{d}F\cos\left(\theta\right)-w_s\,\delta s=0. \tag{3.14}$$

Multiplying (3.13) by $(-\sin\theta)$, and (3.14) by $(\cos\theta)$, before adding the two and divide by ds gives

$$T\frac{\mathrm{d}\theta}{\mathrm{d}s}-\frac{\mathrm{d}F}{\mathrm{d}s}-w_s\cos\left(\theta\right)=0, \tag{3.15}$$

where $\mathrm{d}\theta/\mathrm{d}s$ is the exact expression for curvature κ, also denoted $1/R$, for radius R. From classical beam theory, also called Euler–Bernoulli beam theory, we have that

$$\kappa=\frac{1}{R}=\frac{M}{EI}=\frac{\mathrm{d}\theta}{\mathrm{d}s}, \tag{3.16}$$

and the shear force equation

$$F=\frac{\mathrm{d}M}{\mathrm{d}s}, \tag{3.17}$$

which inserted in (3.15) yields

$$T\frac{\mathrm{d}\theta}{\mathrm{d}s}-EI\frac{\mathrm{d}^3\theta}{\mathrm{d}s^3}-w_s\cos\left(\theta\right)=0. \tag{3.18}$$

The equilibrium of horizontal forces between the two ends of the pipe element in Figure 3.4 are

$$H_0=T\cos\left(\theta\right)+F\sin\left(\theta\right), \tag{3.19}$$

which substituting for F, and substituted in for T in (3.18) yields the equation of for a uniform beam under self weight including flexural effects to be

$$EI\frac{\mathrm{d}}{ds}\left(\sec\left(\theta\right)\frac{\mathrm{d}^2\theta}{\mathrm{d}s^2}\right)-H_0\sec^2\left(\theta\right)\frac{\mathrm{d}\theta}{\mathrm{d}s}-w_s=0. \tag{3.20}$$

This equation is also known as the *nonlinear bending equation* and is valid for both deep and shallow waters and small and large deflections (Seyed and Patel, 1992). Equation (3.20) is of second order, with an unknown free pipe length and bottom reaction, so effectively the problem is of fourth order (Rienstra, 1987). For this problem no exact solutions are known, and approximations must be considered either by numerical methods, or by equation simplification. Numerical approaches were studied for a beam with small deflections in (Wilhoit and Merwin, 1967), and a nonlinear method was studied in Bryndum et al. (1982). If the flexural rigidity vanishes, an exact analytical solutions can be obtained for (3.20), known as the *natural catenary*. If the pipe weight vanishes too, the equation becomes equivalent to the nonlinear pendulum equation.

3.3.2 Gravity and Buoyancy

The unit *dry weight* of a pipe, w_d, is computed as a function of the pipe mass and the acceleration due to gravity, and is the same as the unit force due to gravity. For a circular pipe this force is given by

$$f_g = \frac{\pi}{4}\left(d_o^2 - d_i^2\right)\rho_s g, \tag{3.21}$$

where d_o and d_i are the outer and inner pipe diameter, ρ_s is the density of the pipe cross–section, which typically is made of steel, and g is the acceleration due to gravity. Pipelines of steel are usually coated with corrosion coating and concrete weight coating which have different density, which for the analysis should also be included.

Buoyancy is a hydrostatic force, often referred to as *Archimedes' principle*, after Archimedes who first discovered this law. Archimedes' principle in its most general form states that when a body is completely or partly submerged in a fluid, it experiences an upthrust equal to the weight of the displaced fluid. The buoyant force f_b, acting on a submerged body of arbitrary shape and volume V, is

$$f_b = \rho_w V g, \tag{3.22}$$

where ρ_w is the density of the fluid, which here is water. The buoyancy is generated by the closed pressure field acting on the body surface, and since the buoyancy does not produce moments on the body, it must act in the centroid, coinciding with the center of gravity. Some difficulties are encountered when Archimedes' law is used for computing buoyancy. The law can only be applied directly to completely closed pressure fields, it can not be applied directly to parts of submerged bodies, such as a segment of a submerged pipeline, and it says nothing of internal forces and stresses.

For a segment of a submerged pipe, the pressure field is not closed at the pipe segment ends, hence the effect of buoyancy will become different from what Archimedes' law states. This is addressed by Sparks (2007), who considers the loads on the pipe segment from gravity, internal fluids and external fluids by superposition to derive the *apparent* unit weight, w_a of the pipe,

$$w_a = w_d + w_i - w_e, \tag{3.23}$$

where w_i is the unit weight of the internal fluid, and w_e is the unit weight of the displaced water column. For practical application, the pipe is considered empty, $w_i = 0$, so that (3.22) is again valid, and the so–called *submerged weight* of a body, w_s, can be considered as the nett sum of its weight and buoyancy. The unit submerged weight for a cylindrical pipe, where the unit volume is given by $(pi/4)d_o^2$, is

$$w_s = \frac{\pi}{4}\left(d_o^2\left(\rho_s - \rho_w\right) - d_i^2\rho_s\right)g. \tag{3.24}$$

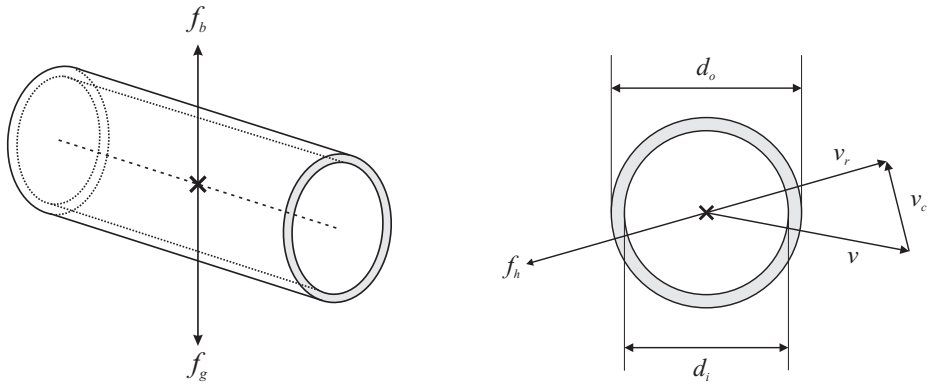

(a) Gravity and buoyancy (b) Hydrodynamic load

Figure 3.5: External loads of the pipline

3.3.3 Hydrodynamic Loads

The hydrodynamic in–line forces from current and wave loads on cylindrical structures such as e.g., risers and pipelines, are for an accelerated fluid environment where the cylinder is kept stationary and vertical (Sumer and Fredsøe, 2006)

$$f_h = \underbrace{\frac{1}{2}\rho_w C_D d_o u|u|}_{\substack{\text{Drag}\\ \text{force}}} + \underbrace{\rho_w C_m A\dot{u}}_{\substack{\text{Hydrodynamic}\\ \text{mass force}}} + \underbrace{\rho A\dot{u}}_{\substack{\text{Froude–Krylov}\\ \text{force}}}, \tag{3.25}$$

where C_D is the drag coefficient, ρ_w is water density, d_o is cylinder diameter, A is cylinder cross–section area, u is the fluid velocity, and C_m is the hydrodynamic mass coefficient. The mass and drag coefficients depends on on many parameters, e.g., Reynolds number, Keulegan–Carpenter number, a relative current number and surface roughness ratio, and have to empirically determined (Faltinsen, 1990). C_m for a cylinder can be found to be

$$C_m = 1. \tag{3.26}$$

The drag force is the resistance in the water to the relative motion, the hydrodynamic mass force is caused by the mass of the fluid around the body which is accelerated with the movement of the body due to action of pressure, and the *Froude–Krylov* force is produced by a pressure gradient due to the accelerated motion of the water in the outer–flow region of the cylinder.

By defining a new coefficient, C_M as

$$C_M = C_m + 1 \tag{3.27}$$

equation (3.25) can be re–written as

$$f_h = \frac{1}{2}\rho C_D d_o u|u| + \rho C_M A\dot{u} \tag{3.28}$$

which is known as the *Morison equation*, introduced in Morison et al. (1950). The new term $\rho C_M A\dot{u}$ is the so–called inertia force, or added mass, and C_M is the inertia coefficient.

In the case where the both the fluid and the cylinder is moving, which is the case for a pipeline being installed in water with currents, (3.25) can be re–written for the hydrodynamic force per unit length as (Sparks, 2007)

$$f_h = -\frac{1}{2}\rho C_D d_o \left(v_r\right)|v_r| - \rho C_m A\left(\dot{v}_r\right) + \rho A\dot{v}_c, \tag{3.29}$$

where v is the velocity of the pipe, v_c is the ocean current velocity, and the relative velocity is given by $v_r = v - v_c$. Note that the Froude–Krylov force is independent of v, as it is associated with the absolute motion of the fluid. Ocean currents are assumed to be slowly varying, so that $\dot{v}_c \approx 0$, and the Froude–Krylov term can be ignored.

The Morison equation was originally derived for wave–induced forces on piles, but has been used almost exclusively to approximate the combined forces from current and wave loads on risers and pipelines, as it is considered to be reasonable accurate as long as the diameter of the cylinder is small compared to the wavelength (Wade and Dwyer, 1976). The Morison equation has been subject to controversy since the drag force is nonlinear. In most applications, the the flow will not be perpendicular to the cylinder, and this allows for two ways of computing the force. Either the drag force can be computed in the direction of the flow and then transformed into components parallel and normal to the pipeline axis, or the velocity can be transformed into components parallel and normal to the pipeline axis, and then the force components can be computed. These methods will generally yield different results. The general practice today is to apply the latter method and then neglect the effect of the component parallel to the axis (Sparks, 2007).

Following Molin (2002), the evaluation of the nonlinear drag force when the velocity vectors $\boldsymbol{v}, \boldsymbol{v}_c \in \mathbb{R}^2$ are not aligned in a plane, can be done the following way. Decomposing the vectors in a common orthonormal frame, spanned by e.g. x and y, so that $(\boldsymbol{v}_c - \boldsymbol{v})$ can be solved directly. Replace each element of $|\boldsymbol{v}_c - \boldsymbol{v}|$ by $|\bar{v}|$, where $\bar{v}$ is the Euclidean norm of $(\boldsymbol{v}_c - \boldsymbol{v})$,

$$\bar{v} = \sqrt{\left(v_{c,x} - v_x\right)^2 + \left(v_{c,y} - v_y\right)^2}. \tag{3.30}$$

For modeling and simulation, installing offshore pipelines is inherently a low–speed application, such that the hydrodynamic effects on the pipe are dominated by the drag force. Hence, $\dot{\boldsymbol{v}} \approx 0$, which implies that the acceleration terms of (3.29) can be neglected in modelling.

3.3.4 Pipe–Soil Interaction

The pipeline configuration on the seabed during installation is determined by the interaction between the pipe and the seabed soil, which is important for the horizontal and vertical stability of the pipeline on the seabed (Braestrup et al., 2005). The most significant effects at the seabed are:

- *Vertical bearing capacity* – Forces that sustain the weight of the pipe.
- *Lateral soil resistance* – The ability of the soil to resist lateral forces imposed on the pipe.
- *Axial soil resistance* – The ability of the soil to resist axial forces imposed on the pipe.

The pipe route on the seabed is selected and prepared by seabed intervention to be as smooth and flat as possible before the pipelay starts. The seabed soil varies from solid rock and hard clay to soft clay, sand and mud. Seabed intervention work, such as e.g., trenching and rock dumping, is often performed before and after the pipelay. This section is adopted from (Braestrup et al., 2005).

Vertical Bearing Capacity

The vertical bearing capacity is the ability of the soil to counteract the weight of the pipe. The pipe will sink into the seabed until the soil reaction force can balance the downward force. For heavy pipelines and soft soil, the pipe may be completely embedded into the seabed. The equilibrium of forces are given by:

$$w_s + f_v + f_w - 2f_f \leq R_V, \tag{3.31}$$

where

f_v - vertical force due to pipe curvature in the vertical plane,
f_w - weight of soil on top of pipe,
f_f - friction along the shear planes,
R_V - Bearing capacity of the soil.

A common approach for modeling the contact forces between the pipe and the soil, used in e.g., van den Boom (1985), is lumped spring and damper pairs that can be tuned to obtain different soil properties. Computations for deep water J–lay on rigid and Winkler soil is done in Lenci and Callegari (2005). See also Pesce et al. (2006).

Lateral Soil Resistance

Steel pipelines has a large torsional stiffness, which will prevent the pipe from rolling on the seabed. Hence, only the soil resistance against sliding is considered here. The lateral soil resistance can be separated into to parts. One part is purely frictional, the other part is due to passive soil pressure. The passive soil pressure is due to pipe embedment, cyclic wave loads, and by the build–up of a soil ridge in front of the pipe. The frictional component depends on the vertical reaction force, and a friction coefficient. In sand, the lateral soil resistance is approximated by:

$$R_H = \mu R_V + \frac{2}{3}\beta\rho_s d_o^2 \left(\frac{H_u}{d_o}\right)^{3/2}, \quad 0 \leq H_u \leq d_o, \tag{3.32}$$

where

R_H - lateral soil resistance,
μ - pipe–soil coefficient of friction,
β - empirical constant,
ρ_s - submerged unit weight of sand,
H_u - height of soil ridge.

In clay, the passive soil resistance depends on the undrained shear strength C_u, such that the lateral soil resistance is approximated by:

$$R_H = \beta C_u d_o \left(\frac{H_u}{D} \right). \tag{3.33}$$

The radius of curvature is normally so large that the bending resistance of the pipe can be neglected, but tension induced in the pipeline during laying will tend to straighten any curves, unless the pipe is kept in place by the lateral soil resistance. The minimum achievable lay radius r_{min}, is computed by:

$$r_{min} = \gamma \frac{H_0}{R_H}, \tag{3.34}$$

where γ is a safety factor, typically set at $\gamma = 1.2$.

Axial Soil Resistance

The effective axial force in free spans depends on the axial soil resistance R_a, where the axial resistance restrains the deflection induced at the supports. The axial soil resistance is found by considering the soil pressure perpendicular to the pipe, which for sand is

$$R_a = \int_A \mu_a \sigma_n dA, \quad \mu_a = \tan\left(f_\phi \phi_s\right), \tag{3.35}$$

where

A - surface area in contact with the soil,
μ_a - axial friction coefficient,
σ_n - normal pressure on the soil,
f_ϕ - skin friction,
ϕ_s - effective angle of friction.

In clay, the axial resistance should be taken as the minimum of (3.35) and

$$R_a = \int_A f_c C_u dA, \tag{3.36}$$

where f_c is the skin friction factor for clay.

3.3.5 Environmental Loads

Ships and offshore structures operating in a sea environment are constantly subject to sea loads and motions caused by *wind*, *waves* and *ocean currents*, which with a common term is named environmental loads. A brief introduction is provided here. Sea loads are extensively treated in the textbook by Faltinsen (1990).

- *Wind* – Wind is the movement of air with respect to the earth surface, and can be described by its direction and speed. The forces and moments generated on a floating body from the wind is highly dependent on the body geometry, and given by

$$\boldsymbol{\tau}_{\text{wind}} = \frac{1}{2}\rho_a V_{rw}^2 \begin{bmatrix} C_X(\gamma_{rw}) A_{F_w} \\ C_Y(\gamma_{rw}) A_{L_w} \\ C_Z(\gamma_{rw}) A_{F_w} \\ C_K(\gamma_{rw}) A_{L_w} H_{L_w} \\ C_M(\gamma_{rw}) A_{F_w} H_{F_w} \\ C_N(\gamma_{rw}) A_{F_w} L_{oa} \end{bmatrix}, \tag{3.37}$$

  where ρ_a is the density of air, V_{rw} is the relative wind speed, γ_{rw} is the relative angle of attack, C_X, C_Y, C_Z, C_K, C_M, and C_N are non–dimensional wind coefficients, H_{F_w} and H_{L_w} are the centroids above the water line of the frontal and lateral areas A_{F_w} and A_{L_w} respectively.

- *Waves* – Waves are induced by the wind, and the wave loads can be separated in *1st–order waves* $\boldsymbol{\tau}_{\text{wave}_1}$, and *2nd–order waves* $\boldsymbol{\tau}_{\text{wave}_2}$ (Faltinsen, 1990).

  - *1st–order wave–induced loads* – zero mean oscillating wave frequency motion,
  - *2nd–order wave–induced loads* – a non–zero mean and slowly–varying drift force.

  Hence, the total wave load is

$$\boldsymbol{\tau}_{\text{wave}} = \boldsymbol{\tau}_{\text{wave}_1} + \boldsymbol{\tau}_{\text{wave}_2}, \tag{3.38}$$

  which has an oscillating motion about a slowly–varying mean value. In control systems, the 1st–order waves are removed by so–called *wave–filters*, so that inly 2nd–order waves are considered by the control system, since for e.g. station–keeping applications, it is the 2nd–order waves that causes the vessel to drift. The effect of wave-loads diminish exponentially with the water depth, and a common rule of thumb is to assume no wave–loads at depths greater than one half wave length. For a typical period of $T = 15\,s$, the wave length is $\lambda = 351\,m$, and the wave-load effect are present down to a water depth of approximately 175 meters.

- *Ocean currents* – For operation in a local area, the current can be assumed to be irrotational, with a linear velocity, $\boldsymbol{v}_c^n$, but no angular velocity. Hence,

the current velocity $\boldsymbol{\nu}_c$ in the inertial frame n is

$$\boldsymbol{\nu}_c^n = \begin{bmatrix} \boldsymbol{v}_c^n \\ \mathbf{0} \end{bmatrix} \in \mathbb{R}^6, \quad \boldsymbol{v}_c^n = \begin{bmatrix} u_c \\ v_c \\ w_c \end{bmatrix} \in \mathbb{R}^3 \tag{3.39}$$

which is assumed to be slowly varying, such that $\dot{\boldsymbol{\nu}}_c^n \approx 0 \rightarrow \dot{\boldsymbol{v}}_c^n \approx 0$. The current velocity in the body–fixed frame is

$$\boldsymbol{v}_c^b = (\boldsymbol{R}_b^n)^{\mathrm{T}} \boldsymbol{v}_c^n, \quad \boldsymbol{R}_b^n \in SO(3), \tag{3.40}$$

where $\boldsymbol{R}_b^n$ is the rotation matrix from n to b defined in (A.4). The relative linear velocity $\boldsymbol{v}_r^b$ and acceleration for a body with linear velocity $\boldsymbol{v}^b$ in water with current velocity $\boldsymbol{v}_c^n$ is then

$$\boldsymbol{v}_r^b = \boldsymbol{v}^b - (\boldsymbol{R}_b^n)^{\mathrm{T}} \boldsymbol{v}_c^n, \tag{3.41}$$

$$\dot{\boldsymbol{v}}_r^b = \dot{\boldsymbol{v}}^b - \left(\dot{\boldsymbol{R}}_b^n\right)^{\mathrm{T}} \boldsymbol{v}_c^n. \tag{3.42}$$

The wind and waves imposes direct loads on ships and offshore structures, whereas the ocean current imposes an indirect load by changing the relative velocity of the body. Hence, to include the loads from the ocean current, the relative velocity must replace the body velocity for hydrodynamic and hydrostatic terms in the equation of motion. A submerged body will experience different directions and speeds for the current at different water depths due to current profiles, which must be accounted for (Yttervik, 2005). For design of structures in the North Sea, the total current velocity is typically taken to be $1\,m/s$.

Environmental Loads on the Pipe

The pipeline is subject to waves and ocean currents. The pipeline is considered a small–volume structure, since $\lambda/d_0 > 5$. The wave-induced excitation loads on such small volume structures can be estimated from Morison equation (3.28), which involves both viscous drag and inertia forces. Using this equation, with $C_M = 2.0$ and $C_D = 1.0$, the viscous drag forces will be greater than the inertia forces for $H/d_o > 4\pi$, where H is the peak–to–peak amplitude.

Environmental Loads on the Pipelay Vessel

The pipelay vessel is subject to wind, waves and current loads. For the vessel concepts of today, the impact of these loads can not be reduced by weathervaning during the pipelay operation, since this would cause excessive stresses on the pipe. In the equations of motion for the pipelay vessel, the wind and wave loads $\boldsymbol{\upsilon}$ are added by using the *principle of superposition*,

$$\boldsymbol{\upsilon} = \boldsymbol{\tau}_{\text{wind}} + \boldsymbol{\tau}_{\text{wave}}, \tag{3.43}$$

In the closed–loop vessel motion control system, the effects of the wind $\boldsymbol{\tau}_{\text{wind}}$ are often compensated for by feedforward, while the effects from the waves are compensated for by a feedback loop, see Figure 2.7.

3.3.6 Stinger Loads

The stinger supports the pipe overbend on rollers, which are spaced out along the stinger. Sometimes rollers are located together in so–called *roller boxes*. The preferred stinger radius, which is the radius of a circle that the curvature of the stinger will follow, is computed in the design phase of the pipelay project. The stinger, which consists of several segments connected by hinges, is then set to correspond to this radius before the installation starts, and remains unchanged throughout the pipelay. Under nominal operating conditions the weight from the pipe should be evenly distributed between the rollers. The pipe will then experience contact forces perpendicular to the pipe axis at the rollers. This contact is modelled by springs where the spring constant is set to zero if the pipe is not in touch with the stinger by Martinez and Goncalves (2003). A mechatronic system for controlling the height of the rollers close to the stinger tip, in order to control the pipeline/stinger reaction forces to extend the operational depth is discussed in Callegari et al. (2000).

The stinger is a very large truss structure extending far from the pipelay vessel it is attached to. The stinger influences the dynamics of the pipelay vessel. The stinger extends deep into the water and is subject to environmental loads from waves and current. For pipelay operations where very large stingers are used, the hydrodynamic effects on the stinger must be included in the model used for the dynamic analysis. Validation for the in–house analysis tool for analyzing dynamic effects on the stinger of Solitaire is described in Marbus (2007).

3.4 Pipelay Vessel Model

Following Fossen (1994), the pipelay vessel is considered to be a *rigid body*, whose kinetics can be represented in 6 degrees of freedom (DOF) as

$$\boldsymbol{M}\dot{\boldsymbol{\nu}} + \boldsymbol{C}(\boldsymbol{\nu})\boldsymbol{\nu} + \boldsymbol{D}(\boldsymbol{\nu})\boldsymbol{\nu} + \boldsymbol{g}(\boldsymbol{\eta}) = \boldsymbol{\tau} + \boldsymbol{\chi} + \boldsymbol{\upsilon}, \tag{3.44}$$

where

$\boldsymbol{M}$	- system inertia matrix including added mass,
$\boldsymbol{C}(\boldsymbol{\nu})$	- Coriolis–centripetal matrix including added mass,
$\boldsymbol{D}(\boldsymbol{\nu})$	- damping matrix,
$\boldsymbol{g}(\boldsymbol{\eta})$	- vector of gravity/buoyancy forces and moments,
$\boldsymbol{\tau}$	- vector of control inputs,
$\boldsymbol{\chi}$	- vector of pipeline forces and moments,
$\boldsymbol{\upsilon}$	- vector of environmental disturbances.

The model assumes an inertial reference frame, the *NED* frame (denoted by n), and a body–fixed frame b. The position of the vessel in the n frame is given by $\boldsymbol{p}^n$, and the vessel orientation with respect to the n frame is given by the rotation matrix from the NED to the body frame, $\boldsymbol{R}_b^n$, which in Fossen (1994) for (3.44) has been parameterized in Euler angles $\boldsymbol{\Theta}$, which is a vector of coefficients and hence not a true vector in n nor b. For the body–fixed frame, the axes are chosen to

coincide with the principal axes of inertia. The linear velocity in b is $\boldsymbol{v}^b$, and the angular velocity of frame b with respect to n decomposed in b is $\boldsymbol{\omega}^b$. Applying the motion variables for a marine vessel according to SNAME (1950), the state vectors of generalized position $\boldsymbol{\eta}$ and velocity $\boldsymbol{\nu}$ are

$$\boldsymbol{\eta} = \begin{bmatrix} \boldsymbol{p}^n \\ \boldsymbol{\Theta} \end{bmatrix}, \qquad \boldsymbol{p}^n = \begin{bmatrix} x \\ y \\ z \end{bmatrix} \in \mathbb{R}^3, \quad \boldsymbol{\Theta} = \begin{bmatrix} \phi \\ \theta \\ \psi \end{bmatrix} \in \mathcal{S}^3, \tag{3.45}$$

$$\boldsymbol{\nu} = \begin{bmatrix} \boldsymbol{v}^b \\ \boldsymbol{\omega}^b \end{bmatrix}, \qquad \boldsymbol{v}^b = \begin{bmatrix} u \\ v \\ w \end{bmatrix} \in \mathbb{R}^3, \quad \boldsymbol{\omega}^b = \begin{bmatrix} p \\ q \\ r \end{bmatrix} \in \mathbb{R}^3. \tag{3.46}$$

The transformations between the n and b frames constitutes the nonlinear kinematics associated to (3.44),

$$\dot{\boldsymbol{\eta}} = \boldsymbol{J}(\boldsymbol{\eta})\,\boldsymbol{\nu}, \tag{3.47}$$

$$\boldsymbol{J}(\boldsymbol{\eta}) = \begin{bmatrix} \boldsymbol{R}_b^n(\boldsymbol{\Theta}) & \boldsymbol{0}_{3\times 3} \\ \boldsymbol{0}_{3\times 3} & \boldsymbol{T}_\Theta(\boldsymbol{\Theta}) \end{bmatrix}, \tag{3.48}$$

where $\boldsymbol{R}_b^n(\boldsymbol{\Theta})$ is parameterized in Euler angles by the zyx–convention, and $\boldsymbol{T}_\Theta(\boldsymbol{\Theta})$ relates the body–fixed angular velocity to the Euler rate vector,

$$\boldsymbol{R}_b^n(\boldsymbol{\Theta}) = \begin{bmatrix} \mathrm{c}\,\psi\,\mathrm{c}\,\theta & -\mathrm{s}\,\psi\,\mathrm{c}\,\phi + \mathrm{c}\,\psi\,\mathrm{s}\,\theta\,\mathrm{s}\,\phi & \mathrm{s}\,\psi\,\mathrm{s}\,\phi + \mathrm{c}\,\psi\,\mathrm{c}\,\phi\,\mathrm{s}\,\theta \\ \mathrm{s}\,\psi\,\mathrm{c}\,\theta & \mathrm{c}\,\psi\,\mathrm{c}\,\phi + \mathrm{s}\,\phi\,\mathrm{s}\,\theta\,\mathrm{s}\,\psi & -\mathrm{c}\,\psi\,\mathrm{s}\,\phi + \mathrm{s}\,\theta\,\mathrm{s}\,\psi\,\mathrm{c}\,\phi \\ -\mathrm{s}\,\theta & \mathrm{c}\,\theta\,\mathrm{s}\,\phi & \mathrm{c}\,\theta\,\mathrm{c}\,\phi \end{bmatrix}, \tag{3.49}$$

$$\boldsymbol{T}_\Theta(\boldsymbol{\Theta}) = \begin{bmatrix} 1 & \mathrm{s}\,\phi\,\mathrm{t}\,\theta & \mathrm{c}\,\phi\,\mathrm{t}\,\theta \\ 0 & \mathrm{c}\,\phi & -\mathrm{s}\,\phi \\ 0 & \mathrm{s}\,\phi/\mathrm{c}\,\theta & \mathrm{c}\,\phi/\mathrm{c}\,\theta \end{bmatrix}, \quad \theta \neq \pm\frac{\pi}{2}, \tag{3.50}$$

where $\mathrm{s}\,\cdot = \sin(\cdot)$, $\mathrm{c}\,\cdot = \cos(\cdot)$, and $\mathrm{t}\,\cdot = \tan(\cdot)$. The following properties apply to the matrices (Fossen, 1994):

P1) $\boldsymbol{M} = \boldsymbol{M}^{\mathrm{T}} > 0, \quad \dot{\boldsymbol{M}} = 0,$

P2) $\boldsymbol{s}^{\mathrm{T}}\left[\dot{\boldsymbol{M}} - 2\boldsymbol{C}(\boldsymbol{\nu})\right]\boldsymbol{s} = 0, \quad \forall\, \boldsymbol{s} \in \mathbb{R}^6,$

P3) $\boldsymbol{C}(\boldsymbol{\nu}) = -\boldsymbol{C}\left(\boldsymbol{\nu}^{\mathrm{T}}\right), \quad \forall\, \boldsymbol{\nu} \in \mathbb{R}^6$

P4) $\boldsymbol{D}(\boldsymbol{\nu}) > 0, \quad \forall\, \boldsymbol{\nu} \in \mathbb{R}^6.$

By applying the kinematic transformations,

$$\begin{aligned} \dot{\boldsymbol{\eta}} &= \boldsymbol{J}(\boldsymbol{\eta})\,\boldsymbol{\nu} && \Leftrightarrow \quad \boldsymbol{\nu} = \boldsymbol{J}^{-1}(\boldsymbol{\eta})\,\dot{\boldsymbol{\eta}} \\ \ddot{\boldsymbol{\eta}} &= \boldsymbol{J}(\boldsymbol{\eta})\,\dot{\boldsymbol{\nu}} + \dot{\boldsymbol{J}}(\boldsymbol{\eta})\,\boldsymbol{\nu} && \Leftrightarrow \quad \dot{\boldsymbol{\nu}} = \boldsymbol{J}^{-1}(\boldsymbol{\eta})\left[\ddot{\boldsymbol{\eta}} - \dot{\boldsymbol{J}}(\boldsymbol{\eta})\,\boldsymbol{J}^{-1}(\boldsymbol{\eta})\,\dot{\boldsymbol{\eta}}\right], \end{aligned} \tag{3.51}$$

the equations of motions (3.44) can be expressed in the n frame,

$$\boldsymbol{M}_\eta(\boldsymbol{\eta})\,\ddot{\boldsymbol{\eta}} + \boldsymbol{C}_\eta(\boldsymbol{\nu},\boldsymbol{\eta})\,\dot{\boldsymbol{\eta}} + \boldsymbol{D}_\eta(\boldsymbol{\nu},\boldsymbol{\eta})\,\dot{\boldsymbol{\eta}} + \boldsymbol{g}_\eta(\boldsymbol{\eta}) = \boldsymbol{J}^{-\mathrm{T}}(\boldsymbol{\eta})\,(\boldsymbol{\tau} + \boldsymbol{\chi} + \boldsymbol{\upsilon}) \tag{3.52}$$

where

$$\boldsymbol{M}_{\eta}(\boldsymbol{\eta}) = \boldsymbol{J}^{-\mathrm{T}}\boldsymbol{M}\boldsymbol{J}^{-1} \tag{3.53}$$

$$\boldsymbol{C}_{\eta}(\boldsymbol{\nu},\boldsymbol{\eta}) = \boldsymbol{J}^{-\mathrm{T}}\left[\boldsymbol{C}(\boldsymbol{\nu}) - \boldsymbol{M}\boldsymbol{J}^{-1}\dot{\boldsymbol{J}}\right]\boldsymbol{J}^{-1} \tag{3.54}$$

$$\boldsymbol{D}_{\eta}(\boldsymbol{\nu},\boldsymbol{\eta}) = \boldsymbol{J}^{-\mathrm{T}}\boldsymbol{D}(\boldsymbol{\nu})\boldsymbol{J}^{-1} \tag{3.55}$$

$$\boldsymbol{g}_{\eta}(\boldsymbol{\eta}) = \boldsymbol{J}^{-\mathrm{T}}\boldsymbol{g}(\boldsymbol{\eta}). \tag{3.56}$$

The properties **P1**, **P2**, and **P4** on equivalent forms holds for (3.52). However, the skew–symmetric property of $\boldsymbol{C}(\boldsymbol{\nu})$ is not conserved in the transformation.

The model (3.44) is a convenient representation which captures the main vessel–ocean–pipe effects, and has been adopted as a standard for vessel control design and analysis purposes. However, in recent years there has been a significant drive to develop time–domain models for simulation and control system design based on data obtained from seakeeping programs such as VERES (Fathi, 2004) and WAMIT (WAMIT, 2004). These programs use potential theory to compute the potential coefficients (added mass and potential damping) and the existing wave loads (Froude–Krylov and diffraction forces) for a given vessel design (Fossen, 2002) and (Fossen and Smogeli, 2004). In Perez and Fossen (2007), a potential theory representation for a surface vessel suited for dynamic positioning and low speed maneuvering is developed.

For low–speed applications, we can approximate the equations of motion with a linear kinetic model,

$$\boldsymbol{M}\dot{\boldsymbol{\nu}} + \boldsymbol{C}_{RB}\boldsymbol{\nu} + \boldsymbol{C}_{A}\boldsymbol{\nu} + \boldsymbol{B}(\infty)\boldsymbol{\nu} + \boldsymbol{\mu} + \boldsymbol{G}\boldsymbol{\eta} = \boldsymbol{\tau}, \tag{3.57}$$

Let

$$\boldsymbol{M} \triangleq \boldsymbol{M}_{RB} + \boldsymbol{M}_{A}, \tag{3.58}$$

where $\boldsymbol{M}_{RB}$ is the rigid body inertia matrix

$$\boldsymbol{M}_{RB} = \begin{bmatrix} m_V\boldsymbol{I}_{3\times 3} & \boldsymbol{0}_{3\times 3} \\ \boldsymbol{0}_{3\times 3} & \boldsymbol{I}_V^b \end{bmatrix}, \tag{3.59}$$

where m_V is the total vessel mass, and $\boldsymbol{I}_V^b \in \mathbb{R}^{3\times 3}$ is the body inertia tensor. Matrix $\boldsymbol{M}_A = \boldsymbol{A}(\infty)$ and $\boldsymbol{B}(\infty)$ are the constant infinite frequency added mass and potential damping matrices. Notice that $\boldsymbol{B}(\infty) = 0$ for zero–speed applications. As the frame used is not inertial, the Coriolis and centripetal terms for the rigid body $\boldsymbol{C}_{RB}$ and the added mass $\boldsymbol{C}_A$ are accounted for, and appears as

$$\boldsymbol{C}_{RB} \triangleq \boldsymbol{M}_{RB}U\boldsymbol{L} \quad \text{and} \quad \boldsymbol{C}_{A} \triangleq \boldsymbol{M}_{A}U\boldsymbol{L}, \tag{3.60}$$

where $U = \|\boldsymbol{v}^e\|$, and

$$\boldsymbol{L} \triangleq \begin{bmatrix} 0 & \cdots & 0 & 0 \\ 0 & \cdots & 0 & 1 \\ 0 & \cdots & -1 & 0 \\ \vdots & \ddots & \vdots & \vdots \\ 0 & \cdots & 0 & 0 \end{bmatrix} \in \mathbb{R}^{6\times 6}. \tag{3.61}$$

The matrix $\boldsymbol{G}$ is the restoring matrix. The external forces acting on the pipelay vessel are the control forces $\boldsymbol{\tau}$, typically from thrusters controlled by a DP system, the forces and moments from the pipe string extending from the vessel $\boldsymbol{\chi}$, and the environmental loads $\boldsymbol{\upsilon}$. For the remainder of this paper $\boldsymbol{\upsilon} = 0$ is assumed.

For t the term $\boldsymbol{\mu}$ is a convolution term representing the fluid memory effects and given for low–speed, i.e. $U = 0$, as

$$\boldsymbol{\mu} \triangleq \int_0^t \boldsymbol{K}(t-\xi)\,\boldsymbol{\nu}(\xi)\,d\xi, \tag{3.62}$$

where $\boldsymbol{K}(t)$ is a matrix of retardation functions (Ogilvie, 1964):

$$\boldsymbol{K}(t) = \int_0^\infty \boldsymbol{B}(\omega)\cos(\omega t)\,d\omega. \tag{3.63}$$

The resulting linear state–space model becomes

$$\boldsymbol{M}\dot{\boldsymbol{\nu}} + \boldsymbol{C}_{RB}\boldsymbol{\nu} + \boldsymbol{C}_A\boldsymbol{\nu} + \boldsymbol{\mu} + \boldsymbol{G}\boldsymbol{\eta} = \boldsymbol{\tau} + \boldsymbol{\chi} + \boldsymbol{\upsilon}. \tag{3.64}$$

In hydrodynamics it is common to assume linear superposition (Faltinsen, 1990), hence nonlinear Coriolis and damping terms can be added directly in the time–domain model (3.64) according to:

$$\boldsymbol{M}\dot{\boldsymbol{\nu}} + \boldsymbol{C}(\boldsymbol{\nu})\,\boldsymbol{\nu} + \boldsymbol{D}(\boldsymbol{\nu})\,\boldsymbol{\nu} + \boldsymbol{g}(\boldsymbol{\varphi}, \boldsymbol{R}_b^e) = \boldsymbol{\tau} + \boldsymbol{\chi} + \boldsymbol{\upsilon}, \tag{3.65}$$

with relaxations, such that nonlinear effects are considered,

$$\boldsymbol{G}\boldsymbol{\eta} \longleftarrow \boldsymbol{g}(\boldsymbol{\varphi}, \boldsymbol{R}_b^e), \tag{3.66}$$

$$\boldsymbol{C}_{RB} \longleftarrow \boldsymbol{C}_{RB}(\boldsymbol{\nu}), \tag{3.67}$$

$$\boldsymbol{C}_A \longleftarrow \boldsymbol{C}_A(\boldsymbol{\nu}), \tag{3.68}$$

and

$$\boldsymbol{C}(\boldsymbol{\nu}) \triangleq \boldsymbol{C}_{RB}(\boldsymbol{\nu}) + \boldsymbol{C}_A(\boldsymbol{\nu}), \tag{3.69}$$

$$\boldsymbol{D}(\boldsymbol{\nu}) \triangleq \boldsymbol{\mu} + \boldsymbol{D}_v(\boldsymbol{\nu}), \tag{3.70}$$

where $\boldsymbol{D}_v(\boldsymbol{\nu})$ is quadratic viscous damping due to cross–flow drag and surge resistance.

Chapter 4

The Catenary Equation

By the introduction of tension based installation methods, see Section 2.2, there was a need to perform analysis of the sagbend stresses and strains to ensure the integrity of the pipe, as well as to determine the required equipment capacity. The natural catenary equation became the starting point for such analysis, and is still used for several applications. The motivation for introducing this equation here is that it will serve as a benchmark for validation of the models developed in the following chapters.

The natural catenary equation is the classical nonlinear solution of the static deflection curve for a string loaded by its own weight. A string has by definition no bending stiffness, only geometrical stiffness. It is nevertheless a good approximation of the curvature in the sagbend of a pipe with stiffness, when the axial tension dominates the bending stiffness. The catenary model has many favorable advantages (Lenci and Callegari, 2005):

- The extreme conceptual simplicity,
- the solution can be written with simple formulas,
- the results are reliable far away from the ends, and
- it is a good starting point for more refined methods.

The main drawbacks are:

- It is inaccurate close to the pipe ends,
- the bending moment is discontinuous at the touchdown point,
- it does not account for dynamic loads.

A general correction to the natural catenary accounting for the bending stiffness influences were proposed by Plunkett (1967), called *the stiffened catenary solution*. This solution was adopted for pipelay vessel operations by Dixon and Rutledge (1968), based on the analysis of pipe stresses induced in laying offshore pipelines (Wilhoit and Merwin, 1967).

The natural catenary is extensively treated in the literature on cable mechanics in general, e.g., Irvine (1981); Triantafyllou (1990) and the references therein, and also on the study on risers, e.g., Aranha et al. (2001); Chatjigeorgiou (2008).

4.1 The Natural Catenary Equation in Pipelaying

The equation for the natural catenary can be derived in the same way as for the elastic beam, but without the flexural terms (Irvine, 1981). Hence the equation of equilibrium can be obtain by canceling the flexural forces F of (3.15), or equivalently the bending stiffness EI of (3.20), to obtain

$$T\frac{\mathrm{d}\theta}{\mathrm{d}s} = w_s \cos(\theta), \tag{4.1}$$

where the solution under the assumptions that the seabed is flat, and axial elongation is ignored, is simply

$$\theta(s) = \tan^{-1}\left(\frac{H}{w_s s}\right), \tag{4.2}$$

where $H = H_0$. Conversion to the x–y frame is obtained by substituting (4.2) into

$$\frac{\mathrm{d}y}{\mathrm{d}s} = \cos(\theta), \quad \frac{\mathrm{d}x}{\mathrm{d}s} = \sin(\theta), \tag{4.3}$$

which yields the classic solution for the shape of a natural catenary

$$y(x) = \frac{H}{w}\left(\cosh\left(\frac{x w_s}{H}\right) - 1\right), \tag{4.4}$$

where x is the horizontal distance from touchdown point, and y is the height above the seabed. The curvature along the pipe is

$$\frac{\mathrm{d}\theta}{\mathrm{d}s} = \frac{\mathrm{d}^2 z}{\mathrm{d}x^2}\cos(\theta) = \frac{w_s}{H}\cosh\left(\frac{x w_s}{H}\right)\cos(\theta). \tag{4.5}$$

The greatest curvature is seen from (4.5) to be at the touchdown point

$$\frac{1}{R} = \frac{w_s}{H}, \tag{4.6}$$

which coincides with the maximum moment. The relationship between curvature and strain for the pipe is

$$\varepsilon = \frac{r}{R}. \tag{4.7}$$

The axial tension at any point s along the catenary is given by

$$T(s) = \sqrt{V^2(s) + H^2(s)}, \quad V(s) = s\, w_s. \tag{4.8}$$

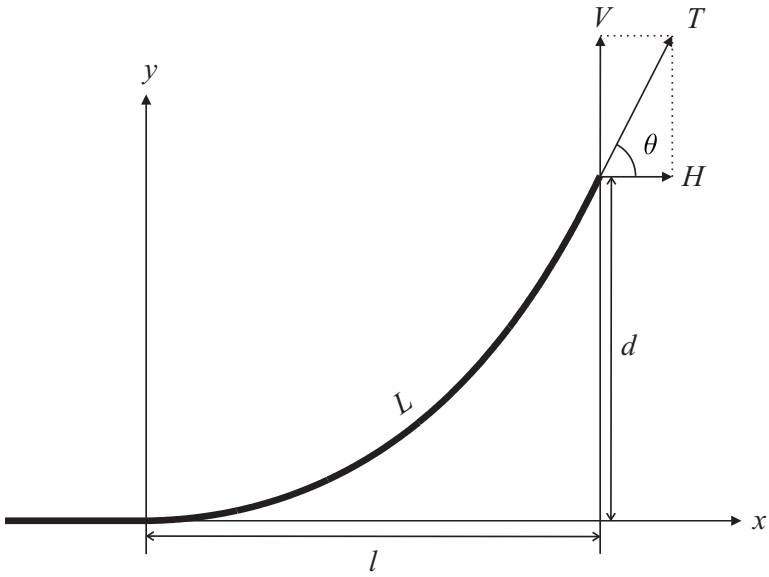

Figure 4.1: The natural catenary.

The expression for the overall length L of the suspended pipe as a function of tension and the water depth is

$$L = d\left(\sqrt{\frac{2T}{w_s d} - 1}\right) = d\left(\sqrt{\frac{2H}{w_s d} + 1}\right), \tag{4.9}$$

where the last transformation can easily bee seen from using (3.6).

The natural catenary for pipeline applications are derived in e.g., Seyed and Patel (1992), which also consider elongation of pipes, and pipes under pressure. A set of useful formulas derived from the catenary equation applicable to design of pipelines are found in e.g., Bai and Bai (2005).

4.2 Quasi–Static Nonlinear Tension

In this section, a nonlinear approximation for the tension T, acting on the pipelay vessel from the pipeline, is derived as a nonlinear spring with spring stiffness found from the natural catenary equation. The model is valid for pipes and cables with relatively small bending stiffness compared to the water depth, which makes it suitable for flexible cables and small diameter pipelines in relative deep water. This quasi–static approach is still frequently used to model loads on ocean structures from connected risers and pipes despite that that the model does not account for dynamic effects.

The vertical tension $V(T, d)$ is readily seen to be a nonlinear spring where the water depth d at the touchdown point is considered the displacement, by inserting

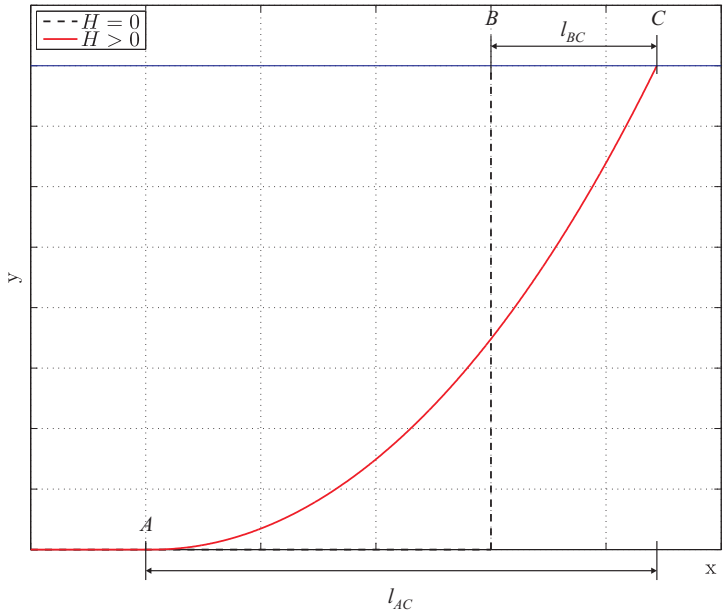

Figure 4.2: Dashed line indicates case where $H(T,d)=0$, and solid line indicates case where $H(T,d)>0$.

(4.9) into (3.5) to obtain

$$V(T,d)=w_s d\left(\sqrt{\frac{2T}{w_s d}-1}\right)=w_s d\left(\sqrt{\frac{2H}{w_s d}+1}\right). \tag{4.10}$$

When no horizontal tension is applied, $H=H(T,d)=0$, (4.8) implies that $T=V$, and that the pipe will be vertical as illustrated by the dashed line *(AB)* in Figure 4.2. For $H(T,d)>0$ the catenary shape is obtained, illustrated by the solid line *(AC)*. Inserting $H(T,d)=0$ in (4.9) it is found that

$$H(T,d)=0 \quad \Rightarrow \quad L=d. \tag{4.11}$$

When the top point of the pipe is subject to a horizontal force $H(T,d)>0$, it moves to *(C)*. The horizontal distance from the vessel to the touchdown point, the so–called *the touchdown distance*, denoted by l_{AC}, is found to be (Irvine, 1981)

$$l_{AC}=d\ln\left(\gamma+\sqrt{\gamma^2+1}\right)^{\delta}, \tag{4.12}$$

where

$$\delta=\frac{H}{w_s d} \quad \text{and} \quad \gamma=\frac{\sqrt{2\delta+1}}{\delta}. \tag{4.13}$$

To model the horizontal tension as a spring force, the position where the spring is at rest is found at *(B)* in the figure. The extension of the spring is given by the

displacement l_{BC} on the surface. For a vessel in *(C)* the tension and depth are measured, and thus l_{AC} can be computed.

From the geometric considerations in Figure 4.2, the extra length in the pipe compared to the equilibrium for the spring is defined by $l_{AB} = L - d$, which by insertion is seen to be

$$l_{AB} = -d\left(1 - \sqrt{\frac{2T}{w_s d} - 1}\right), \tag{4.14}$$

and thus the touchdown distance may be used as the spring displacement in place of l_{AC}, is given as

$$l_{BC} = l_{AC} - l_{AB}, \tag{4.15}$$

and thus the function for the touchdown distance $l_{BC}(T)$ is found to be

$$l_{BC}(T) = d\left(1 - \sqrt{2\delta - 1} + \ln\left(\gamma + \sqrt{\gamma^2 + 1}\right)^{\delta}\right). \tag{4.16}$$

By using (3.6), the equivalent function $l_{BC}(H)$ is found. Inversion will yield a function $H(l_{BC})$ which is a nonlinear spring function for the horizontal pipe force. For verification at $H = 0$ we find that $l_{AC} = l_{BC} = 0$.

The values of l_{AC} and l_{BC} are plotted in Figure 4.3 for a given constant water depth $d = 500\ m$ and $H = 0 \ldots 100\,kN$. The nonlinearity of the spring is evident from the figure.

For a fixed water depth, a polynomial expression $H(x, z)$ can be obtained by polynomial fitting. The polynomial will be on the form

$$H(\tilde{x}) = p_1\tilde{x}^n + p_2\tilde{x}^{n-1} + ... + p_n\tilde{x} + p_{n+1}, \tag{4.17}$$

where $p_1 ... p_{n+1}$ are scalar coefficients and $\tilde{x} = l_{BC} = x - x_0$. Applying the Matlab function `polyfit` to fit a polynomial of order $n = 6$ to the plotted values in Figure 4.3, yields the coefficients

$$\begin{aligned}
p_1 &: \quad 3.1494e-009 \\
p_2 &: -2.1046e-006 \\
p_3 &: \quad 6.4073e-004 \\
p_4 &: -0.0850e-000 \\
p_5 &: \quad 1.0344e+001 \\
p_6 &: \quad 2.2933e+002 \\
p_7 &: \quad 5.0276e+002
\end{aligned}$$

If the horizontal tension is increased from H_1 to H_2, by ΔH where $H_1 < H_2$, l_{AC} will increase. The length of the suspended pipe will increase by ΔL

$$\Delta L = d\left[\left(\sqrt{\frac{2H_2}{mgd} + 1}\right) - \left(\sqrt{\frac{2H_1}{mgd} + 1}\right)\right]. \tag{4.18}$$

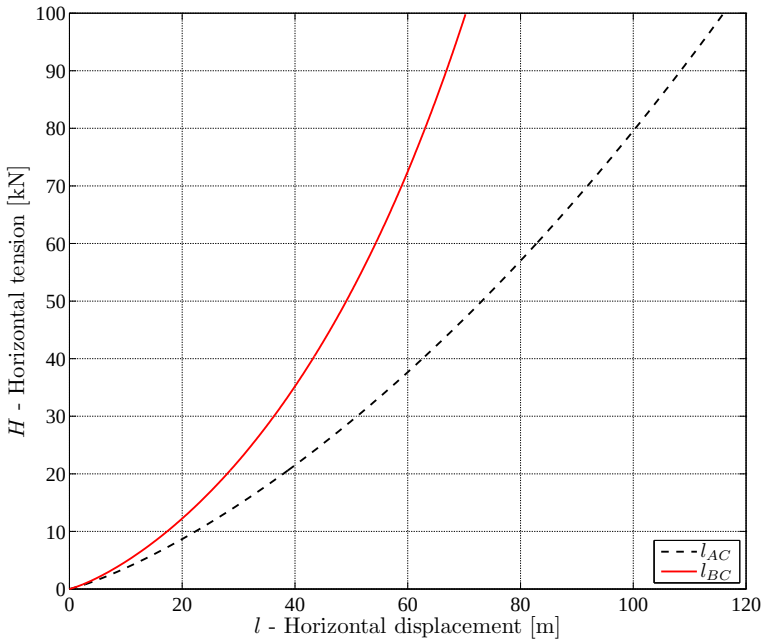

Figure 4.3: Plot of l_{BC} and l_{AC} where $H \in [0, 100]$ kN.

The increase in tension will also yield an increase in the touchdown distance by $\Delta l_{AC} = l_{AC_2} - l_{AC_1}$, which is found to be

$$\Delta l_{AC} = d \ln \left[\frac{\left(\alpha + \left(\alpha^2 + 1\right)^{1/2}\right)^{\beta}}{\left(\gamma + \left(\gamma^2 + 1\right)^{1/2}\right)^{\delta}} \right], \tag{4.19}$$

where

$$\delta = \frac{H_1}{mgd}, \qquad \gamma = \frac{\sqrt{2\delta + 1}}{\delta}, \tag{4.20}$$

$$\beta = \frac{H_2}{mgd}, \qquad \alpha = \frac{\sqrt{2\beta + 1}}{\beta}. \tag{4.21}$$

Finally, $H_1 \to H_2 \Longrightarrow l_{BC_1} \to l_{BC_2}$ where $\Delta l_{BC} = l_{BC_2} - l_{BC_1}$, defined as

$$\Delta l_{BC} = \Delta l_{AC} - \Delta L. \tag{4.22}$$

This work shows that the spring equivalent of a pipe freely suspended from a pipelay vessel during pipeline installation is described by a nonlinear spring. It seems reasonable that the nonlinear spring force will be more accurate than a linear spring force.

4.3 The Stiffened Catenary Equation

The idea of the stiffened catenary solution is that the bending stiffness causes secondary effects in boundary regions only, and that the deviation from the simple catenary solution can be found as a rapid converging series (Larsen, 1976). The first improvements were suggested to mend the inaccuracy of the pipe end points by Wilhoit and Merwin (1967), and in 1967, Plunkett (1967) suggested the Stiffened Catenary model to find an analytical approximation of the pipe laying problem by introducing an asymptotic expansion to the catenary equation. In the decade to follow, the method was given much attention, and applied to pipelay applications in Dixon and Rutledge (1968); Brewer and Dixon (1969); Palmer et al. (1974); Larsen (1976).

Both catenary models meet the real–time requirement for control and observer models, but lacks the dynamic behavior of the pipe string. The methods are best used to compute an approximation of the lay–tension and curvature, or as initial condition for more advanced models. The performance of control systems based on these models will be best at zero speed, and decrease with increasing speed.

Chapter 5

A Robotic Pipe Model

The elastic pipe spanning from the pipelay vessel to the seabed can be approximated as a slender structure of many rigid links connected by rotational joints. In a robotic context such systems are known as a hyper–redundant manipulator. The compact robotic system formulation (Spong and Vidyasagar, 1989; Sciavicco and Siciliano, 2001) is used for a variety of systems, e.g. marine vessels (3.44), (Fossen, 2002). An extensive toolbox for system analysis is readily available for such systems, and the model can effectively be implemented in a computer code. In this chapter a nonlinear dynamic pipe model is developed on the robotic form,

$$\boldsymbol{M}(\boldsymbol{q})\,\ddot{\boldsymbol{q}} + \boldsymbol{C}(\boldsymbol{q},\dot{\boldsymbol{q}})\,\dot{\boldsymbol{q}} + \boldsymbol{D}(\boldsymbol{q},\dot{\boldsymbol{q}})\,\dot{\boldsymbol{q}} + \boldsymbol{f}(\boldsymbol{q}) + \boldsymbol{g}(\boldsymbol{q}) + \boldsymbol{\sigma}(\boldsymbol{q}) = \boldsymbol{\tau}(\boldsymbol{q}), \tag{5.1}$$

where

$\boldsymbol{M}(\boldsymbol{q})$	- system inertia matrix,
$\boldsymbol{C}(\boldsymbol{q},\dot{\boldsymbol{q}})$	- Coriolis–centripetal matrix,
$\boldsymbol{g}(\boldsymbol{q})$	- vector of gravitational forces,
$\boldsymbol{f}(\boldsymbol{q})$	- vector of flexural effects,
$\boldsymbol{\sigma}(\boldsymbol{q})$	- vector of seabed interaction forces,
$\boldsymbol{\tau}(\boldsymbol{q})$	- vector of control inputs.

This model captures the main dynamics of the pipe, including its geometric configuration and top tension. All the main internal and external loads discussed in Chapter 3 are accounted for, e.g., inertial forces, Coriolis and centripetal forces, restoring forces, hydrodynamic damping, bending stiffness and seabed interaction. However, environmental loads are not accounted for. The model is in the state–space, and on a vectorial form using minimal coordinates, and the quasi–static assumptions are relaxed.

In pipelay operation simulation, pipe tension is computed and applied as an input to the pipelay vessel. This tension is commonly computed by quasi–static methods based on the catenary equation, as shown in Figure 5.1. The catenary equation is static, and not able to capture the dynamics of the pipe or flexural effects. The quasi–static assumptions are relaxed in the developed robotic pipe

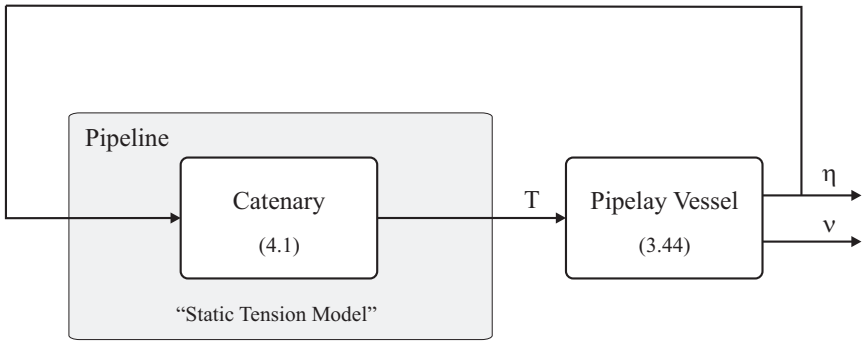

Figure 5.1: Simulation of a pipelay vessel using the catenary equation to compute the pipe tension vector $\boldsymbol{T}$. The models for pipe and vessel are connected in a master–slave configuration. The vessel is the master system, as it is actuated by thrusters and the pipe is the slave system, taking the vessel position as input.

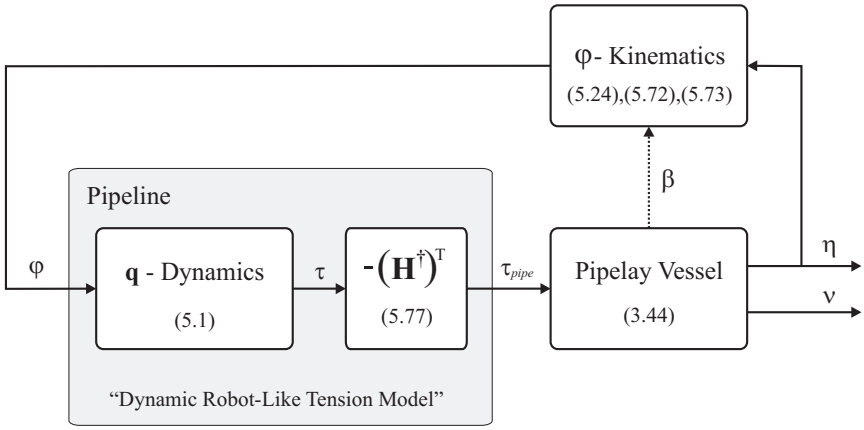

Figure 5.2: Simulation of a pipelay vessel using a dynamic robot–like model to compute the pipe tension. Equation references are given in parentheses for each block.

model. By replacing the catenary pipe tension model by the robotic pipe model the dynamic tension can be computed, see Figure 5.2. The notation in the figure will be presented in later sections. The proposed model can also replace computationally slower finite element models in applications with real–time requirements.

The presented robotic pipe model is fast, and should able to meet real–time requirements. These features classify this model as a *control model* with respect to Figure 1.2. T model is also suitable for e.g. real–time decision support systems, in simulators and training simulators, motion prediction systems, Hardware–In–the–Loop (HIL) testing, for operability analysis to determine acceptable working conditions for the pipelay operation and in pre–design of ships. This chapter is based on the publications Jensen et al. (2008) and Jensen and Fossen (2009).

5.1 Kinematics

The kinematics for the pipe in the vertical plane is derived in this section. Direct and inverse kinematic equations establish the relationship between the joint variables and the corresponding positions and orientations in the operational space. Differential kinematics gives the relationship between the joint velocity, and the corresponding linear and angular velocity.

5.1.1 Assumptions

Let the pipe string be divided into n rigid links, each denoted by $i = 1 \dots n$, of length l_i and mass m_i connected by one degree of freedom (DOF) revolute joints. Assume that the links are cylindrical with uniform density, and point masses, located in the link mass centers, see Figure 5.3.

Let frame 0, spanned by $\{x_0, y_0\}$, be inertial and fixed to the seabed. Let the pipe be fixed at the origin of 0. An orthogonal reference frame $i = 1 \dots n$, spanned by $\{x_i, y_i\}$, is fixed to each link in the structure, such that its x–axis is pointing toward link $i + 1$ in accordance with the *Denavit–Hartenberg convention*. Vectors given with respect to these frames are in the *operational space*. However, when a vector is said to be in the operational space in this text, it implies that it is given in reference frame 0. The configuration of the pipe is given in the *joint space* or *configuration space*, by the vector of generalized coordinates,

$$\boldsymbol{q} = \begin{bmatrix} q_1 & q_2 & \dots & q_n \end{bmatrix}^{\mathrm{T}} \in \mathbb{R}^n, \tag{5.2}$$

where q_i denote the angle of joint i. Let the general rotation matrix $\boldsymbol{R}_i^0$ from frame 0 to i be defined as

$$\boldsymbol{R}_i^0(\boldsymbol{q}) = \begin{bmatrix} \cos(\alpha_i) & -\sin(\alpha_i) \\ \sin(\alpha_i) & \cos(\alpha_i) \end{bmatrix}, \tag{5.3}$$

where

$$\alpha_i = \sum_{k=1}^{i} q_k. \tag{5.4}$$

5.1.2 Direct and Differential Kinematics

Let the position of joint $i = 1 \dots n$ in the operational space be

$$\boldsymbol{p}_i^j = \begin{bmatrix} x_i^j & y_i^j \end{bmatrix}^{\mathrm{T}}, \tag{5.5}$$

where

$$x_i^j = \sum_{j=1}^{i-1} l_j \cos(\alpha_j), \tag{5.6}$$

$$y_i^j = \sum_{j=1}^{i-1} l_j \sin(\alpha_j). \tag{5.7}$$

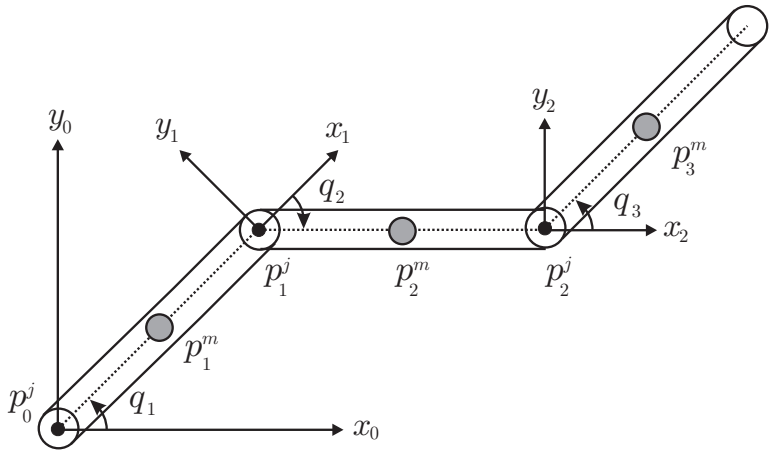

Figure 5.3: The first three links of a planar robotic manipulator with corresponding body–fixed reference frames. The joint $\boldsymbol{p}_0^j$ is at the base of the robot.

The linear velocity $\boldsymbol{v}_i^j$ of joint i in the operational space is derived as the time derivative of the joint position (5.5),

$$\boldsymbol{v}_i^j = \begin{bmatrix} \dot{x}_i^j & \dot{y}_i^j \end{bmatrix}^{\mathrm{T}}, \tag{5.8}$$

where

$$\dot{x}_i^j = \sum_{j=1}^{i-1} \left(-l_j \sin\left(\alpha_j\right) \dot{\alpha}_j\right), \tag{5.9}$$

$$\dot{y}_i^j = \sum_{j=1}^{i-1} \left(l_j \cos\left(\alpha_j\right) \dot{\alpha}_j\right), \tag{5.10}$$

and

$$\dot{\alpha}_i = \sum_{k=1}^{i} \dot{q}_k. \tag{5.11}$$

For each joint i, the Jacobian matrix $\boldsymbol{J}_i^j(\boldsymbol{q}) \in \mathbb{R}^{2\times n}$ represents the mapping from the time–derivative of the generalized coordinates, to the linear velocity of the joint. Hence

$$\boldsymbol{v}_i^j = \boldsymbol{J}_i^j(\boldsymbol{q})\, \dot{\boldsymbol{q}}, \tag{5.12}$$

where

$$\boldsymbol{J}_i^j(\boldsymbol{q}) = \begin{bmatrix} \left(\boldsymbol{J}_i^j(\boldsymbol{q})\right)_1 & \left(\boldsymbol{J}_i^j(\boldsymbol{q})\right)_2 & \cdots & \left(\boldsymbol{J}_i^j(\boldsymbol{q})\right)_n \end{bmatrix}, \tag{5.13}$$

and the columns of the matrix are found from (5.8) to be

$$\left(\boldsymbol{J}_i^j\left(\boldsymbol{q}\right)\right)_k = \begin{cases} \begin{bmatrix} -\sum_{j=k}^{i-1} l_j \sin\left(\alpha_j\right) \\ \sum_{j=k}^{i-1} l_j \cos\left(\alpha_j\right) \end{bmatrix} & , k < i \\ \begin{bmatrix} 0 \\ 0 \end{bmatrix} & , k \geqslant i. \end{cases} \tag{5.14}$$

The kinematics for the masses are slightly more involving than for the joints. Let the position of mass i in the operational space be

$$\boldsymbol{p}_i^m = \begin{bmatrix} x_i^m & y_i^m \end{bmatrix}^{\mathrm{T}}, \tag{5.15}$$

where

$$x_i^m = \sum_{j=1}^{i-1} l_j \cos\left(\alpha_j\right) + \frac{1}{2} l_i \cos\left(\alpha_i\right), \tag{5.16}$$

$$y_i^m = \sum_{j=1}^{i-1} l_j \sin\left(\alpha_j\right) + \frac{1}{2} l_i \sin\left(\alpha_i\right). \tag{5.17}$$

The linear velocity $\boldsymbol{v}_i^m$ of mass i in the operational space is the time derivative of the position of the mass (5.15),

$$\boldsymbol{v}_i^m = \begin{bmatrix} \dot{x}_i^m & \dot{y}_i^m \end{bmatrix}^{\mathrm{T}}, \tag{5.18}$$

where

$$\dot{x}_i^m = \sum_{j=1}^{i-1} \left(-l_j \sin\left(\alpha_j\right) \dot{\alpha}_j\right) - \frac{1}{2} l_i \sin\left(\alpha_i\right) \dot{\alpha}_i, \tag{5.19}$$

$$\dot{y}_i^m = \sum_{j=1}^{i-1} \left(l_j \cos\left(\alpha_j\right) \dot{\alpha}_j\right) + \frac{1}{2} l_i \cos\left(\alpha_i\right) \dot{\alpha}_i. \tag{5.20}$$

For each mass i, the Jacobian matrix $\boldsymbol{J}_i^m\left(\boldsymbol{q}\right) \in \mathbb{R}^{2\times n}$ represents the mapping from the time–derivative of the generalized coordinate vector, to the linear velocity of the mass center. Hence

$$\boldsymbol{v}_i^m = \boldsymbol{J}_i^m\left(\boldsymbol{q}\right) \dot{\boldsymbol{q}}, \tag{5.21}$$

where

$$\boldsymbol{J}_i^m\left(\boldsymbol{q}\right) = \begin{bmatrix} \left(\boldsymbol{J}_i^m\left(\boldsymbol{q}\right)\right)_1 & \left(\boldsymbol{J}_i^m\left(\boldsymbol{q}\right)\right)_2 & \dots & \left(\boldsymbol{J}_i^m\left(\boldsymbol{q}\right)\right)_n \end{bmatrix}, \tag{5.22}$$

and the columns of the matrix are found from (5.18) to be

$$\left(\boldsymbol{J}_i^m\left(\boldsymbol{q}\right)\right)_k = \begin{cases} \begin{bmatrix} -\sum_{j=k}^{i-1} l_j \sin\left(\alpha_j\right) - \frac{1}{2} l_i \sin\left(\alpha_i\right) \\ \sum_{j=k}^{i-1} l_j \cos\left(\alpha_j\right) + \frac{1}{2} l_i \cos\left(\alpha_i\right) \end{bmatrix} & , k < i \\ \begin{bmatrix} -\frac{1}{2} l_i \sin\left(\alpha_i\right) \\ \frac{1}{2} l_i \cos\left(\alpha_i\right) \end{bmatrix} & , k = i \\ \begin{bmatrix} 0 \\ 0 \end{bmatrix} & , k > i. \end{cases} \tag{5.23}$$

The direct and differential kinematics for the pipe have now been derived.

5.1.3 Inverse Kinematics of the Pipe–Tip

What is commonly referred to as the *manipulator* or *end–effector* in robotics is in this paper called *the pipe–tip*, and this section deals with the inverse kinematics of the pipe–tip.

Let the position and orientation of the pipe–tip in the operational space be denoted by

$$\boldsymbol{\varphi} = \begin{bmatrix} \left(\boldsymbol{p}_n^j\right)^{\mathrm{T}}, & \alpha_n \end{bmatrix}^{\mathrm{T}} \in \mathbb{R}^2 \times \mathcal{S}. \tag{5.24}$$

Accounting for the dependence of position and orientation of the joint variables, the direct kinematic equation is

$$\boldsymbol{\varphi} = h\left(\boldsymbol{q}\right), \tag{5.25}$$

where $h\left(\cdot\right)$ allows computation of the operational space variables from the joint space variables. Assume that the inverse kinematics exists, and follows from (5.25)

$$\boldsymbol{q} = h^{-1}\left(\boldsymbol{\varphi}\right). \tag{5.26}$$

For $n > 3$, there is no unique solution to (5.26). By choosing $n = 3$, the model will only have three links, and will not be applicable for practical applications. Generally, there is not a well defined way to find the inverse kinematics, and it might not even be possible. However, the inverse kinematics can be consider as an optimization problem of nonlinear zero finding of the form

$$\min_q \left\{J = \boldsymbol{\varphi} - h\left(\boldsymbol{q}\right)\right\}. \tag{5.27}$$

By choosing a good initial condition and constraints on the solutions of $\boldsymbol{q}$, the solution can be found. The derivative is defined as

$$\dot{\boldsymbol{\varphi}} = \frac{\partial h\left(\boldsymbol{q}\right)}{\partial \boldsymbol{q}} \dot{\boldsymbol{q}} \triangleq \boldsymbol{H}\left(\boldsymbol{q}\right) \dot{\boldsymbol{q}}, \tag{5.28}$$

where $\boldsymbol{H}(\boldsymbol{q}) \in \mathbb{R}^{3\times n}$ is a mapping from the joint space to the operational space found to be

$$\boldsymbol{H}(\boldsymbol{q}) = \left[\begin{array}{cc} \left(\boldsymbol{J}_n^j(\boldsymbol{q})\right)^{\mathrm{T}}, & \mathbf{1}^{\mathrm{T}} \end{array} \right]^{\mathrm{T}}. \tag{5.29}$$

For readability, $\boldsymbol{H}(\boldsymbol{q})$ will be denoted by $\boldsymbol{H}$, omitting the argument for the remainder of this chapter. The inverse kinematics are assumed to exist, and are found from (5.28) as

$$\dot{\boldsymbol{q}} = \boldsymbol{H}^{\dagger}\dot{\boldsymbol{\varphi}}, \tag{5.30}$$

where $\boldsymbol{H}^{\dagger}$ is the right pseudo–inverse,

$$\boldsymbol{H}^{\dagger} = \boldsymbol{H}^{\mathrm{T}}\left(\boldsymbol{H}\boldsymbol{H}^{\mathrm{T}}\right)^{-1}, \tag{5.31}$$

with the second derivative found to be

$$\ddot{\boldsymbol{\varphi}} = \dot{\boldsymbol{H}}\dot{\boldsymbol{q}} + \boldsymbol{H}\ddot{\boldsymbol{q}}, \tag{5.32}$$

$$\ddot{\boldsymbol{q}} = \boldsymbol{H}^{\dagger}\ddot{\boldsymbol{\varphi}} - \boldsymbol{H}^{\dagger}\dot{\boldsymbol{H}}\boldsymbol{H}^{\dagger}\dot{\boldsymbol{\varphi}}, \tag{5.33}$$

where $\dot{\boldsymbol{H}}$ can be computed by time differentiation of (5.29) using (5.13). Hence,

$$\dot{\boldsymbol{H}} = \left[\begin{array}{ccc} \dot{\boldsymbol{H}}_1, & \ldots, & \dot{\boldsymbol{H}}_n \end{array} \right]. \tag{5.34}$$

5.2 Dynamics

The kinematic relationships for the model has now been established. This section considers the model kinetics, which deals with the relationship between the motion of the links and the motion generating forces and torques.

5.2.1 Equations of Motion

A Lagrangian formulation is used to develop the equations of motion for the pipe in the vertical plane. Following Sciavicco and Siciliano (2001), the equation of motion for a robot manipulator in the joint space, excluding friction terms, can be written in the compact matrix form

$$\boldsymbol{M}(\boldsymbol{q})\ddot{\boldsymbol{q}} + \boldsymbol{C}(\boldsymbol{q},\dot{\boldsymbol{q}})\dot{\boldsymbol{q}} + \boldsymbol{g}(\boldsymbol{q}) = \boldsymbol{\tau}(\boldsymbol{q}), \tag{5.35}$$

where

$\boldsymbol{M}(\boldsymbol{q})$	- system inertia matrix,
$\boldsymbol{C}(\boldsymbol{q},\dot{\boldsymbol{q}})$	- Coriolis–centripetal matrix,
$\boldsymbol{g}(\boldsymbol{q})$	- vector of gravitational forces,
$\boldsymbol{\tau}(\boldsymbol{q})$	- vector of control inputs.

In the following, this formulation is adopted for an elastic pipeline completely submerged in water by including buoyancy, hydrodynamic effects of drag (and added mass), bending stiffness and seabed interaction, to obtain (5.1). Buoyancy

and added mass terms belong in $\boldsymbol{g}(\boldsymbol{q})$ and $\boldsymbol{M}(\boldsymbol{q})$ respectively, while drag, bending stiffness and seabed interaction is included by superposition.

The inertia matrix for the rigid body $\boldsymbol{M}(\boldsymbol{q}) \in \mathbb{R}^{n\times n}$ for the planar manipulator with point masses m_i is symmetric, positive definite, configuration dependent, and given by

$$\boldsymbol{M}(\boldsymbol{q}) = \sum_{i=1}^{n} \left(m_i \left(\boldsymbol{J}_i^m(\boldsymbol{q}) \right)^{\mathrm{T}} \boldsymbol{J}_i^m(\boldsymbol{q}) \right). \tag{5.36}$$

The added mass is not considered here. The choice of Coriolis–centripetal matrix $\boldsymbol{C}(\boldsymbol{q}, \dot{\boldsymbol{q}}) \in \mathbb{R}^{n\times n}$ is not unique, and alternative representations can be found. One particular choice for $\boldsymbol{C}(\boldsymbol{q}, \dot{\boldsymbol{q}})$ is found where the generic element are

$$c_{ij} = \sum_{k=1}^{n} c_{ijk} \dot{q}_k, \tag{5.37}$$

where the coefficients c_{ijk} are termed *Christoffel symbols of the first type*. By choosing the matrix $\boldsymbol{C}(\boldsymbol{q}, \dot{\boldsymbol{q}})$ in this way, $\dot{\boldsymbol{M}}(\boldsymbol{q}) - 2\boldsymbol{C}(\boldsymbol{q}, \dot{\boldsymbol{q}})$ is skew–symmetric, i.e.

$$\boldsymbol{\nu}^{\mathrm{T}} \left[\dot{\boldsymbol{M}}(\boldsymbol{q}) - 2\boldsymbol{C}(\boldsymbol{q}, \dot{\boldsymbol{q}}) \right] \boldsymbol{\nu} = 0 \quad \forall \quad \boldsymbol{\nu} \in \mathbb{R}^n. \tag{5.38}$$

Note that the complexity of $\boldsymbol{M}(\boldsymbol{q})$ and hence $\boldsymbol{C}(\boldsymbol{q}, \dot{\boldsymbol{q}})$, will grow significantly when the number of links increase. However, as the links are considered to be point masses the complexity is kept down. Also, the *Recursive Newton–Euler Algorithm* can be employed for numerical treatment of large systems since $\boldsymbol{C}(\boldsymbol{q}, \dot{\boldsymbol{q}})$ is then no longer required to be found analytically.

Each link is subject to gravity and buoyancy. As the links are assumed to be completely submerged in water, the centers of gravity and buoyancy coincide with the mass center. Hence, for link i, the gravity $\boldsymbol{g}_{g_i} \in \mathbb{R}^n$ and buoyancy $\boldsymbol{g}_{b_i} \in \mathbb{R}^n$, both attacks in $\boldsymbol{p}_i^m$, and are given in the operational space as

$$\boldsymbol{g}_{g_i} = m_i \begin{bmatrix} 0, & g \end{bmatrix}^{\mathrm{T}}, \tag{5.39}$$

$$\boldsymbol{g}_{b_i} = -V_i \rho_w \begin{bmatrix} 0, & g \end{bmatrix}^{\mathrm{T}}, \tag{5.40}$$

where V_i is the link volume, ρ_w is water density, and g is the acceleration of gravity. Hence, the vector $\boldsymbol{g}(\boldsymbol{q})$ in (5.35) is the combined restoring forces of the n links represented in the generalized coordinates, found to be

$$\boldsymbol{g}(\boldsymbol{q}) = \sum_{i=1}^{n} \left(\boldsymbol{J}_i^m(\boldsymbol{q}) \right)^{\mathrm{T}} \left(\boldsymbol{g}_{g_i} + \boldsymbol{g}_{b_i} \right). \tag{5.41}$$

In robotic manipulators, actuators placed in the joints are used to control the configuration, and the actuator control forces are given in the vector $\boldsymbol{\tau}(\boldsymbol{q})$. In the pipelay operation, control forces are only actively applied to the pipe–tip, denoted in the operational space by $\boldsymbol{T} = \begin{bmatrix} H & V \end{bmatrix}^{\mathrm{T}} \in \mathbb{R}^2$, which converted to general coordinates and denoted by $\boldsymbol{\tau}(\boldsymbol{q})$ in (5.35) is given by

$$\boldsymbol{\tau}(\boldsymbol{q}) = \left(\boldsymbol{J}_n^j(\boldsymbol{q}) \right)^{\mathrm{T}} \boldsymbol{T}. \tag{5.42}$$

The pipe is elastic and deforms under stress. Stiffness is the resistance of an elastic body to deformation by an applied force, and this property is implemented in the model by linear springs in the rotational joints. For joint i, with spring constant $k_i \in \mathbb{R}$, and displacement q_i, the spring force $f_i(q_i)$ is given by

$$f_i(q_i) = k_i q_i. \tag{5.43}$$

The magnitude of the $k_i = k_i(EI, l_i)$ depends on the unit bending stiffness of the pipe (EI), and the length l_i, of the link. Let

$$\boldsymbol{K} = diag\left[\ k_1, \quad k_2, \quad \ldots, \quad k_n\ \right]^{\mathrm{T}}, \tag{5.44}$$

such that the flexural effects $\boldsymbol{f}(\boldsymbol{q})$ are given by

$$\boldsymbol{f}(\boldsymbol{q}) = \boldsymbol{K}\boldsymbol{q}. \tag{5.45}$$

Note that the elasticity effect is modeled directly on the states and not the mass centers of the links.

Motivated by Morison equation (3.28), the quadratic damping force on vectorial form for a pipe link i is

$$\boldsymbol{d}_i\left(\bar{\boldsymbol{v}}_i^j\right) = -C_D \frac{1}{2}\rho_w d_o \left\|\bar{\boldsymbol{v}}_i^j\right\| \bar{\boldsymbol{v}}_i^j, \tag{5.46}$$

where C_D is the drag coefficient (found from experiments), d_o is the outer pipe diameter, $\bar{\boldsymbol{v}}_i^j$ is the undisturbed velocity normal to link i, and $\|\cdot\|$ is the Euclidean norm. Positive force is defined in the wave propagation direction. The vector $\bar{\boldsymbol{v}}_i^j$ denotes the component of $\boldsymbol{v}_i^j$ normal to link i, and it is found by applying a coordinate transformation of $\boldsymbol{v}_i^j$ from frame 0 to the body fixed frame i, selecting the normal component and a second coordinate transformation back to the 0 frame. The formulation of $\bar{\boldsymbol{v}}_i^j$ in generalized coordinates is

$$\bar{\boldsymbol{v}}_i^j = \boldsymbol{P}_i(\boldsymbol{q})\,\boldsymbol{J}_i^j(\boldsymbol{q})\,\dot{\boldsymbol{q}}, \tag{5.47}$$

where

$$\boldsymbol{P}_i(\boldsymbol{q}) = \left(\boldsymbol{R}_i^0(\boldsymbol{q})\right)\begin{bmatrix} 0 & 0 \\ 0 & 1 \end{bmatrix}\left(\boldsymbol{R}_i^0(\boldsymbol{q})\right)^{\mathrm{T}}, \tag{5.48}$$

is a linear mapping from $\boldsymbol{v}_i^j$ to $\bar{\boldsymbol{v}}_i^j$, where the rotation matrix $\boldsymbol{R}_i^0(\boldsymbol{q})$, given in (5.3) is used as a coordinate transformations of vectors from i to 0, following Egeland and Gravdahl (2002). Note that $\boldsymbol{P}_i^{-1}$ does not exist. Let $\gamma_i = \frac{1}{2}C_D\rho_w d\ l_i \geq 0$, and apply (5.47) to (5.46) to express the drag force on a link i in general coordinates. This yields

$$\boldsymbol{d}_i(\boldsymbol{q}, \dot{\boldsymbol{q}}) = -\gamma_i \left\|\boldsymbol{v}_i^j\right\| \boldsymbol{P}_i(\boldsymbol{q})\,\boldsymbol{J}_i^j(\boldsymbol{q})\,\dot{\boldsymbol{q}}. \tag{5.49}$$

The total hydrodynamic damping effects on the system $\boldsymbol{D}(\boldsymbol{q}, \dot{\boldsymbol{q}}) \in \mathbb{R}^{n\times n}$ are given by

$$\boldsymbol{D}(\boldsymbol{q}, \dot{\boldsymbol{q}}) = \sum_{i=1}^{n}\left(-\gamma_i \left\|\boldsymbol{v}_i^j\right\| \left(\boldsymbol{J}_i^j(\boldsymbol{q})\right)^{\mathrm{T}} \boldsymbol{P}_i(\boldsymbol{q})\,\boldsymbol{J}_i^j(\boldsymbol{q})\right). \tag{5.50}$$

Note that if the drag force is computed based on the velocity of the point masses rather than the joints, and the links are of equal length, as in Jensen et al. (2008), standing waves of wavelength close to $2l_i$ is not damped out. This oscillation is however rapidly damped out by making the drag force depend on the transversal link velocity at the joints.

The interaction with the seabed is modeled by a spring and damper in each pipe joint that is touching the seabed. For a joint i, the force from the seabed σ_i is given by

$$\sigma_i = \begin{cases} -k_\sigma y_i^j - d_\sigma \dot{y}_i^j & , \; y_i^j \leqslant 0 \\ 0 & , \; y_i^j > 0 \end{cases} \tag{5.51}$$

where k_σ is the soil spring constant, and d_σ is the soil damper constant. k_σ is determined such that equilibrium for pipe penetration equals 1/8 of the pipe diameter. The total seabed force $\boldsymbol{\sigma}$ in general coordinates given by

$$\boldsymbol{\sigma}(\boldsymbol{q}) = \sum_{i=1}^{n} \left(\boldsymbol{J}_i^j(\boldsymbol{q}) \right)^{\mathrm{T}} \begin{bmatrix} 0 \\ \sigma_i \end{bmatrix}. \tag{5.52}$$

The complete set of equations of motion for the approximated submerged pipeline can now be found by imposing the hydrodynamic, flexural and environmental effects onto (5.35) to obtain (5.1).

5.2.2 Pipe–Tip Tension

The inverse kinematics can be used to compute the force in the operational space at the pipe–tip for a given pipe configuration given in the joint space. A dynamic formulation for this force is developed in this section. This is obtained by substituting equations (5.26,5.30,5.33) into (5.1) and pre–multiplying by $\left(\boldsymbol{H}^\dagger\right)^{\mathrm{T}}$,

$$\widetilde{\boldsymbol{M}}(\boldsymbol{\varphi})\,\ddot{\boldsymbol{\varphi}} + \widetilde{\boldsymbol{C}}(\boldsymbol{\varphi})\,\dot{\boldsymbol{\varphi}} + \widetilde{\boldsymbol{D}}(\boldsymbol{\varphi})\,\dot{\boldsymbol{\varphi}} + \widetilde{\boldsymbol{f}}(\boldsymbol{\varphi}) + \widetilde{\boldsymbol{g}}(\boldsymbol{\varphi}) + \widetilde{\boldsymbol{\sigma}}(\boldsymbol{\varphi}) = \left(\boldsymbol{H}^\dagger\right)^{\mathrm{T}} \boldsymbol{\tau}, \tag{5.53}$$

where

$$\widetilde{\boldsymbol{M}}(\boldsymbol{\varphi}) = (\boldsymbol{H}^\dagger)^{\mathrm{T}} \boldsymbol{M}(\boldsymbol{q})\, \boldsymbol{H}^\dagger \tag{5.54}$$

$$\widetilde{\boldsymbol{C}}(\boldsymbol{\varphi}) = \left(\boldsymbol{H}^\dagger\right)^{\mathrm{T}} \left(\boldsymbol{C}(\boldsymbol{q}, \dot{\boldsymbol{q}}) - \boldsymbol{M}(\boldsymbol{q})\, \boldsymbol{H}^\dagger \dot{\boldsymbol{H}} \right) \boldsymbol{H}^\dagger \tag{5.55}$$

$$\widetilde{\boldsymbol{D}}(\boldsymbol{\varphi}) = \left(\boldsymbol{H}^\dagger\right)^{\mathrm{T}} \boldsymbol{D}(\boldsymbol{q}, \dot{\boldsymbol{q}})\, \boldsymbol{H}^\dagger \tag{5.56}$$

$$\widetilde{\boldsymbol{f}}(\boldsymbol{\varphi}) = \left(\boldsymbol{H}^\dagger\right)^{\mathrm{T}} \boldsymbol{f}(\boldsymbol{q}) \tag{5.57}$$

$$\widetilde{\boldsymbol{g}}(\boldsymbol{\varphi}) = \left(\boldsymbol{H}^\dagger\right)^{\mathrm{T}} \boldsymbol{g}(\boldsymbol{q}) \tag{5.58}$$

$$\widetilde{\boldsymbol{\sigma}}(\boldsymbol{\varphi}) = \left(\boldsymbol{H}^\dagger\right)^{\mathrm{T}} \boldsymbol{\sigma}(\boldsymbol{q}) \tag{5.59}$$

which can be solved for $\boldsymbol{T}$. If the control requirement on the orientation in (5.53) is relaxed, so that the departure–angle is no longer controlled, (5.25) and (5.29) are relaxed, such that

$$\boldsymbol{H}(\boldsymbol{q}) \Rightarrow \boldsymbol{J}_n^j(\boldsymbol{q}) \quad \text{and} \quad \boldsymbol{\varphi} \Rightarrow \boldsymbol{p}_n^j. \tag{5.60}$$

5.2.3 Model Limitations

This pipe model is designed to be compact and computationally effective to meet real–time requirements, and to replace the catenary equation in simulations and control applications. In order to achieve this, several simplifications are made at the expense of accuracy which can be obtained by e.g. FEM pipe models.

1. **Planar model** – The model is like the catenary equation limited to the vertical plane. Replacing the 1 DOF joints with 2 DOF ball joints will give the full three–dimensional dynamics, while doubling the degrees of freedom of the system.

2. **Coriolis matrix** – The Coriolis matrix chosen relies on Christoffel symbols. Employing the Recursive Newton–Euler Algorithm may speed up the computation of $\boldsymbol{C}(\boldsymbol{q}, \dot{\boldsymbol{q}})$.

3. **Point masses** – A result of using point masses is that the links have no moments. Introducing rigid links with distributed mass and moment may improve on the accuracy of the simulations.

4. **Bending stiffness** – There is no direct mapping between the spring constants k_i in the modeling of the bending stiffness, and the real bending stiffness. One way of determining k_i is to compare simulation results to a more advanced model, e.g., FEM, and choose k_i that yields the smallest error. This approach can be used to tune the model in a controller.

5.3 Passivity

Passivity provides a powerful tool for the stability analysis of nonlinear systems. Let the input be given by $\boldsymbol{\tau}$ and let the output $\boldsymbol{y}$ be defined as

$$\boldsymbol{y} = \dot{\boldsymbol{q}}. \tag{5.61}$$

For the storage function $V(\boldsymbol{q}, \dot{\boldsymbol{q}})$ defined as

$$V(\boldsymbol{q}, \dot{\boldsymbol{q}}) = \frac{1}{2}\dot{\boldsymbol{q}}^{\mathrm{T}}\boldsymbol{M}(\boldsymbol{q})\dot{\boldsymbol{q}} + \frac{1}{2}\boldsymbol{q}^{\mathrm{T}}\boldsymbol{K}\boldsymbol{q} + \int_0^{\boldsymbol{q}(t)} (\boldsymbol{g}(\zeta) + \boldsymbol{\sigma}(\zeta))\, d\zeta, \tag{5.62}$$

the system is input–output passive. Here, V can be interpreted as the sum of kinetic and potential energy of the pipe, where zero energy corresponds to the equilibrium point $\boldsymbol{q} = \boldsymbol{0}$ and $\dot{\boldsymbol{q}} = \boldsymbol{0}$. From the previous section it is known that

the inertia matrix is positive definite, $\boldsymbol{M}(\boldsymbol{q}) > 0$, $\boldsymbol{K} > 0$, and $\boldsymbol{K} = \boldsymbol{K}^{\mathrm{T}}\ \forall \boldsymbol{q}$ which implies that

$$V(\boldsymbol{q}, \dot{\boldsymbol{q}}) > 0, \quad \forall \boldsymbol{q}, \dot{\boldsymbol{q}} \in \mathbb{R}^n \setminus \{\boldsymbol{0}\}. \tag{5.63}$$

The time derivative of $V(\boldsymbol{q}, \dot{\boldsymbol{q}})$ along the system trajectories of (5.1) is found by taking the time derivative of the cost function (5.62), and substituting for $\boldsymbol{M}(\boldsymbol{q})\,\ddot{\boldsymbol{q}}$ using (5.1). This choice of cost function, along with the property (5.38) yields

$$\begin{aligned}
\dot{V}(\boldsymbol{q}, \dot{\boldsymbol{q}}) &= \frac{1}{2}\dot{\boldsymbol{q}}^{\mathrm{T}}\dot{\boldsymbol{M}}(\boldsymbol{q})\,\dot{\boldsymbol{q}} + \dot{\boldsymbol{q}}^{\mathrm{T}}\boldsymbol{M}(\boldsymbol{q})\,\ddot{\boldsymbol{q}} + \dot{\boldsymbol{q}}^{\mathrm{T}}\boldsymbol{K}\boldsymbol{q} + \dot{\boldsymbol{q}}^{\mathrm{T}}\boldsymbol{g}(\boldsymbol{q}) + \dot{\boldsymbol{q}}^{\mathrm{T}}\boldsymbol{\sigma}(\boldsymbol{q}) \\
&= \frac{1}{2}\dot{\boldsymbol{q}}^{\mathrm{T}}\dot{\boldsymbol{M}}(\boldsymbol{q})\,\dot{\boldsymbol{q}} - \dot{\boldsymbol{q}}^{\mathrm{T}}\boldsymbol{C}(\boldsymbol{q}, \dot{\boldsymbol{q}})\,\dot{\boldsymbol{q}} - \dot{\boldsymbol{q}}^{\mathrm{T}}\boldsymbol{D}(\boldsymbol{q}, \dot{\boldsymbol{q}})\,\dot{\boldsymbol{q}} + \dot{\boldsymbol{q}}^{\mathrm{T}}\boldsymbol{\tau}(\boldsymbol{q}) \\
&= -\dot{\boldsymbol{q}}^{\mathrm{T}}\boldsymbol{D}(\boldsymbol{q}, \dot{\boldsymbol{q}})\,\dot{\boldsymbol{q}} + \dot{\boldsymbol{q}}^{\mathrm{T}}\boldsymbol{\tau}(\boldsymbol{q}).
\end{aligned} \tag{5.64}$$

Since $\boldsymbol{D}(\boldsymbol{q}, \dot{\boldsymbol{q}})$ is positive semidefinite,

$$\dot{V} \leq \dot{\boldsymbol{q}}^{\mathrm{T}}\boldsymbol{\tau}(\boldsymbol{q}), \tag{5.65}$$

which implies that the system is input–output passive.

Positive definiteness of $\boldsymbol{D}(\boldsymbol{q}, \dot{\boldsymbol{q}})$ can be proved by reformulating (5.50) by inserting (5.48) such that

$$\boldsymbol{D}(\boldsymbol{q}, \dot{\boldsymbol{q}}) = \gamma \sum_{i=1}^{n} \left(\left\| \boldsymbol{v}_i^j \right\| \boldsymbol{\Lambda}_i^{\mathrm{T}}(\boldsymbol{q})\,\boldsymbol{\Lambda}_i(\boldsymbol{q}) \right), \tag{5.66}$$

where

$$\boldsymbol{\Lambda}_i(\boldsymbol{q}) = \begin{bmatrix} 0 & 0 \\ 0 & 1 \end{bmatrix} \left(\boldsymbol{R}_i^0(\boldsymbol{q})\right)^{\mathrm{T}} \boldsymbol{J}_i^j(\boldsymbol{q}). \tag{5.67}$$

The matrix $\boldsymbol{\Lambda}_i(\boldsymbol{q})$ is rank deficient, and $\boldsymbol{\Lambda}_i^{\mathrm{T}}(\boldsymbol{q})\,\boldsymbol{\Lambda}_i(\boldsymbol{q})$ is symmetric, so it follows from Strang (1986) that $\boldsymbol{D}(\boldsymbol{q}, \dot{\boldsymbol{q}})$ is positive semidefinite. To get a physical understanding of this recall that the drag force defined in (5.46) only damps the motions normal to the pipe elements. The tangential motion is not damped and thus there will be zero damping for longitudinal velocities, thus there exists $\dot{\boldsymbol{q}} \neq \boldsymbol{0}$ such that $\boldsymbol{D}(\boldsymbol{q}, \dot{\boldsymbol{q}}) = \boldsymbol{0}$. If surface friction of the pipe in the tangential direction is introduced, the matrix $\boldsymbol{\Lambda}_i(\boldsymbol{q})$ will have full rank and $\boldsymbol{D}(\boldsymbol{q}, \dot{\boldsymbol{q}})$ would be positive definite, such that $\dot{\boldsymbol{q}}^{\mathrm{T}}\boldsymbol{D}(\boldsymbol{q}, \dot{\boldsymbol{q}})\,\dot{\boldsymbol{q}} \geq \boldsymbol{0}$, $\boldsymbol{q}, \dot{\boldsymbol{q}} \in \mathbb{R}^n$.

By choosing a passive controller such as a PD–controller the closed–loop system is by Theorem 6.1 in Khalil (2002), also passive.

5.4 Model Validation

The motivation for developing the robotic pipe model is to replace the natural catenary equation by it in simulations to improve performance. In this section we will compare the model to the natural catenary equation. The static geometric configurations are considered, as well as a dynamic scenario to emphasize the effect of the dynamic terms in the robotic model.

All simulations are performed on a 30 inch steel pipe where $n = 9$ is installed at a water depth of 900 meters using Matlab. The physical pipe properties and constants are given in Table 5.1.

Parameter	*Notation*	*Value*	*Unit*
Outer pipe diameter (OD)	d	0.762	m
Wall thickness	WT	0.033	m
Undeformed pipe length	L	1500	m
Unit mass of empty pipe	m	593.2818	kg/m
Submerged unit weight	w	$1.2341 \cdot 10^3$	N/m
Spring stiffness	k	$1.0 \cdot 10^7$	N/m
Water depth	h	900	m
Density of steel	ρ_s	$7.850 \cdot 10^6$	kg/m^3
Density of water	ρ_w	$1.025 \cdot 10^3$	kg/m^3
Acceleration of gravity	g	9.81	m/s^2

Table 5.1: Numerical values for the parameters applied in the validation scenarios.

5.4.1 The Static Case

For the static case, where $\ddot{\boldsymbol{q}} = \dot{\boldsymbol{q}} = \mathbf{0}$, the robotic model (5.1) is reduced to

$$\boldsymbol{f}(\boldsymbol{q}) + \boldsymbol{g}(\boldsymbol{q}) + \boldsymbol{\sigma}(\boldsymbol{q}) = \boldsymbol{\tau}(\boldsymbol{q}). \tag{5.68}$$

where the configuration of the pipe is shaped only by the bending stiffness, gravity, buoyancy and seabed interaction forces.

Case 1

The static geometric configuration of the robotic model (5.68) is compared to the geometric configuration obtained by the natural catenary equation (4.4), where the parameters of Table 5.1 are used in both cases. Since the natural catenary does not account for flexural effects, $\boldsymbol{f}(\boldsymbol{q}) = \mathbf{0}$ of (5.68). A constant top tension is applied, where $H = (200, 400, 800)\ kN$, and V is given on a controller like structure as

$$V = -\rho_w A_{wp} \left(y_n^j - h\right) g, \tag{5.69}$$

where y_n^j is heave position of the pipe–tip, to keep the pipe tip at the nominal surface. See Figure 5.4 for the configurations, and Table 5.2 for a comparison of the hang–off angles α_n, and lay–back distances l_h, which are the horizontal distance from the touchdown point to the pipe–tip. The configurations and the hang–off angles corresponds well, however the lay–back distance is seen to become inaccurate for $n = 9$, which must be expected for $l_i = 167$ meters.

Case 2

For the case where $\boldsymbol{f}(\boldsymbol{q}) \neq \mathbf{0}$, the spring constant k_i must be determined. There is no direct mapping between the bending stiffness EI and k_i. However, k_i can be

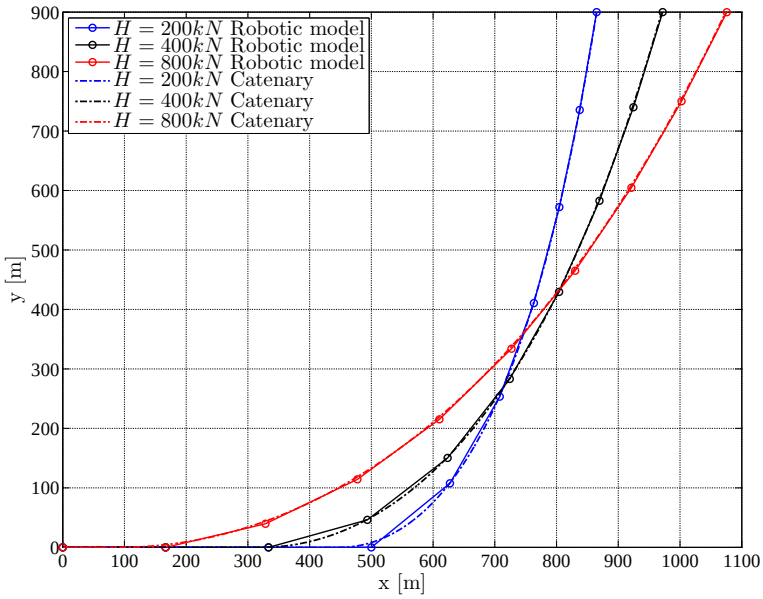

Figure 5.4: Robotic model (5.68) configuration where $n = 9$ compared to the natural catenary equation (4.4) for different top–tension values H.

determined by computing the static configurations using a FEM program, and take k_i such that the configurations from (5.68) overlap. For $n = 9$, k_i is approximated to be $10^7\ N/m$ using the FEM program RIFLEX (Fylling et al., 2008), see Figure 5.5. Note that this should only be considered a rough approximation for k_i. The system seems to be robust with respect to the value chosen for k_i. However, this is based on a small set of data, and more work needs to be done to establish this property.

5.4.2 The Dynamic Case

The pipe–tip tension $\boldsymbol{T}$ is for the dynamic case found from (5.1) and (5.42) under assumption (5.60) to be

$$\boldsymbol{T} = \left(\left(\boldsymbol{J}_n^j \left(\boldsymbol{q} \right) \right)^{\dagger} \right)^{\mathrm{T}} \left(\boldsymbol{M} \left(\boldsymbol{q} \right) \ddot{\boldsymbol{q}} + \boldsymbol{C} \left(\boldsymbol{q}, \dot{\boldsymbol{q}} \right) \dot{\boldsymbol{q}} + \boldsymbol{D} \left(\boldsymbol{q}, \dot{\boldsymbol{q}} \right) \dot{\boldsymbol{q}} + \boldsymbol{f} \left(\boldsymbol{q} \right) + \boldsymbol{g} \left(\boldsymbol{q} \right) - \boldsymbol{\sigma} \left(\boldsymbol{q} \right) \right), \tag{5.70}$$

and for the static case, $\ddot{\boldsymbol{q}} = \dot{\boldsymbol{q}} = \boldsymbol{0}$, with no bending stiffness, $\boldsymbol{f} \left(\boldsymbol{q} \right) = \boldsymbol{0}$, to be

$$\boldsymbol{T} = \left(\left(\boldsymbol{J}_n^j \left(\boldsymbol{q} \right) \right)^{\dagger} \right)^{\mathrm{T}} \left(\boldsymbol{g} \left(\boldsymbol{q} \right) - \boldsymbol{\sigma} \left(\boldsymbol{q} \right) \right), \tag{5.71}$$

In this section the contribution of the different terms in the robotic formulation (5.70) are investigated by simulating the system by applying a known time–varying horizontal top tension $H\left(t\right)$. The implementation is done in Matlab, using the embedded solver `ode15`.

Horizontal tension	H	200	400	800	kN
Robot pipe model					
Hang–off angle	α_n	80.5	73.5	63.9	deg
Lay–back distance	l_h	365	638	909	m
Catenary					
Hang–off angle	α_n	81.2	74.7	65.2	deg
Lay–back distance	l_h	416	649	983	m

Table 5.2: Static analysis results without the flexural effects, i.e, $\boldsymbol{f}(\boldsymbol{q}) = \boldsymbol{0}$.

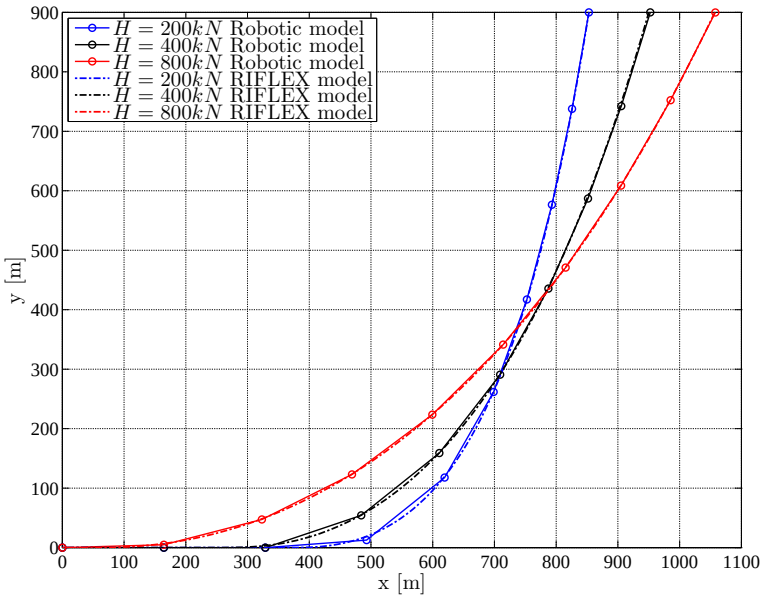

Figure 5.5: Determining k_i by comparing configurations of the robotic model (5.68) and RIFLEX.

Case 1

Let static equilibrium solution for horizontal tension $H = 400\,kN$ be the initial condition for the pipe. To simulate the effect of vessel motion due to waves, H is linearly increased by $\dot{H} = 20\,kN/s$ to $H = 500\,kN$, kept constant for $20\,s$, before it is linearly decreased by $\dot{H} = -20\,kN/s$ to $400\,kN$, see Figure 5.6.

Case 2

The scenario of the previous case is repeated, now with $\dot{H} = \pm 80\,kN/s$ in three consecutive repetitions. See Figure 5.7. The figures indicate that approximating

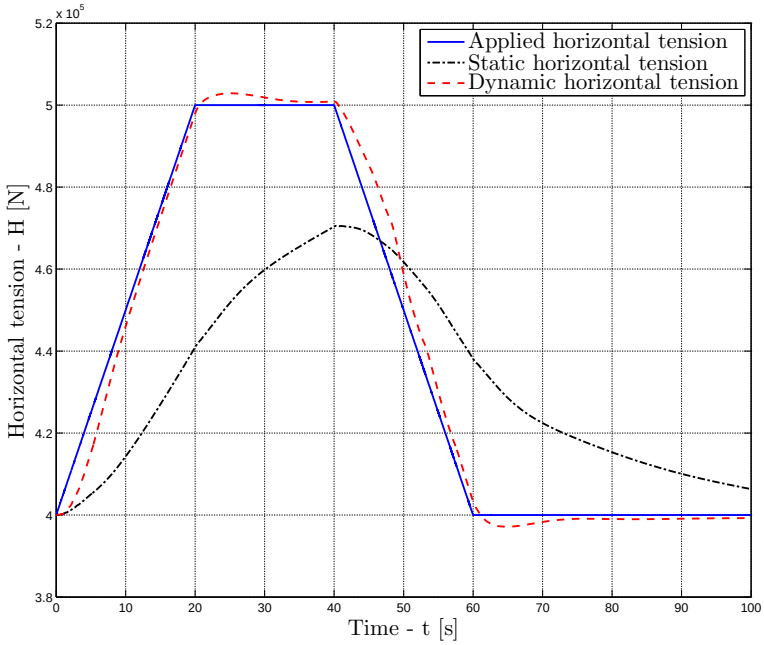

Figure 5.6: Horizontal tension computed for a slowly moving vessel from (5.70).

the tension by the position dependent terms only, which is comparable to the catenary equation, is not so good. However, when the tension is approximated using the position and velocity dependent terms, the results are considerably better. This implies that for low speed applications, the acceleration dependent terms may be neglected.

This dynamic simulation has been performed with $n = 9$, which seems to be too few nodes, as motion of the pipe–tip propagates to the touchdown point near instantly. The simulations should be repeated with more elements to obtain more accurate results.

5.5 Control Applications

The pipeline and pipelay vessel are two connected mechanical systems, see Figure 5.8, where the motion of the pipe is highly influenced by the vessel motion. The equations of motion for the pipelay vessel (3.44) is about the center of gravity of the vessel. However, the forces from the pipe will have to be moved to act on the same point by using the parallel axis theorem. The pipelay vessel model (3.44) and the robotic model (5.1) are given in different inertial frames, such that the relations between these must be established before the systems are combined. Let $\boldsymbol{p}_{pipe} \in \mathbb{R}^2$ be the position of the pipe–tip in b, such that

$$\boldsymbol{p}_n^j = \boldsymbol{p}_v + \boldsymbol{R}_b^0(\boldsymbol{q})\,\boldsymbol{p}_{pipe}, \tag{5.72}$$

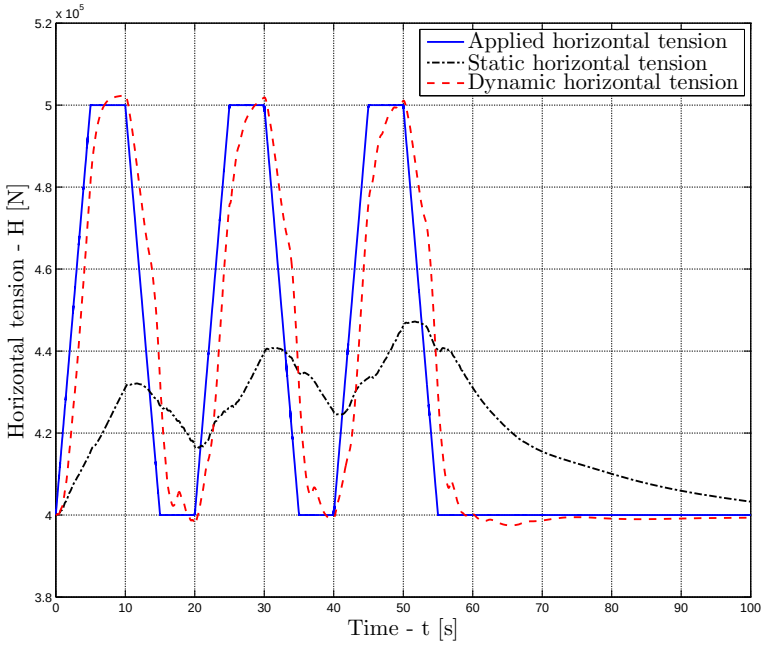

Figure 5.7: Horizontal tension computed for a faster moving vessel from (5.70).

where $\boldsymbol{R}_b^0(\boldsymbol{q}) \in SO(2)$ denotes the rotation matrix from frames 0 to b. The pipe lift–off angle in the operational space $\alpha_n(\boldsymbol{q})$, is given by the pitch of the vessel and the departure angle β as

$$\alpha_n(\boldsymbol{q}) = \theta_v + \beta. \tag{5.73}$$

Hence, the rotation matrix $\boldsymbol{R}_b^0(\alpha_n(\boldsymbol{q})) \in SO(2)$ from 0 to b is

$$\boldsymbol{R}_b^0(\theta_v) = \begin{bmatrix} \cos(\theta_v) & -\sin(\theta_v) \\ \sin(\theta_v) & \cos(\theta_v) \end{bmatrix} \boldsymbol{R}_{x,\pi}. \tag{5.74}$$

where $\boldsymbol{R}_{x,\pi}$ defines a rotation by π about the x–axis in the vertical plane,

$$\boldsymbol{R}_{x,\pi} = \begin{bmatrix} 1 & 0 \\ 0 & -1 \end{bmatrix}. \tag{5.75}$$

In the SNAME notation (SNAME, 1950), the z–axis is positive downwards, while in robotic notation, it is positive upwards. If the vessel position is given with positive heave upwards, $\boldsymbol{R}_{x,\pi} = \boldsymbol{0}$, due to the following relationships for the rotations holds:

$$\boldsymbol{R}_n^0 = \boldsymbol{R}_b^0 \boldsymbol{R}_n^b \quad \Leftrightarrow \quad \boldsymbol{R}_n^b = \left(\boldsymbol{R}_b^0\right)^{\mathrm{T}} \boldsymbol{R}_n^0. \tag{5.76}$$

The pipe and vessel are connected based on first–principles into a total system. such that

$$\boldsymbol{\chi} = -\left(\boldsymbol{H}^{\dagger}\right)^{\mathrm{T}} \boldsymbol{\tau}(\boldsymbol{q}). \tag{5.77}$$

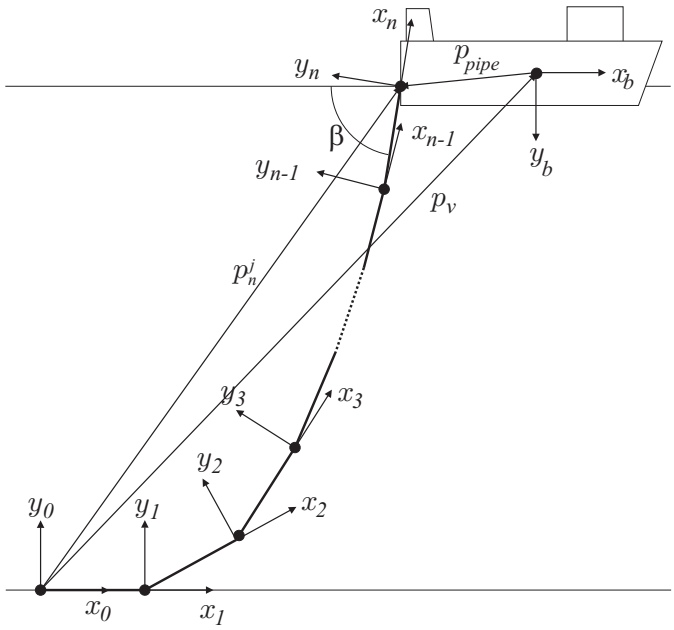

Figure 5.8: Connecting the robot pipe to a pipelay vessel.

An example of a PD and PID–controllers implementing a DP system based on an early version of this model is implemented in Jensen et al. (2008).

5.6 Conclusions

The concepts of robotics have been applied to develop a pipe model for a suspended pipe. The model is designed to be fast, and include the main dynamics of the pipe. Hence, with respect to the classification of models presented in Figure 1.2, this model is applicable as a *controller model*. The provided passivity proof also supports this application. These results indicate that the proposed robot–like pipe model will be suitable for implementation in model based controllers. However, more work to improve and validate the model is required.

Further work to improve this model and make it more accurate and faster are:

- Extend the number of nodes that can be simulated,
- Extend to full 3D,
- Add seabed friction, lateral and longitudinal,
- Include added mass,
- Develop a generic way to map bending stiffness spring constants.

Additionally, a complete dynamic validation against a FEM model should be performed to supplement the dynamic simulation results presented here.

Chapter 6

A PDE Pipe Model

6.1 Introduction

In this chapter a nonlinear formulation for the dynamics of an elastic pipe string is developed. A three–dimensional finite strain beam formulation, capable of undergoing finite extension, shearing, twisting and bending, is extend to account for the effects of gravity and buoyancy, hydrodynamic drag and seabed contact forces by applying the principle of superposition. This model is expressed as a partial differential equation (PDE), which in Chapter 7 will be solved by a finite element method and validated against the catenary equation, presented in Chapter 4, and the commercial computer code RIFLEX (Fylling et al., 2008).

A potential theory formulation of a surface vessel, suited for dynamic positioning and low speed maneuvering, is used as the upper boundary condition to form a system encompassing both pipe and vessel. Hence, analyses where the dynamics of the vessel is integrated can be performed with vessel control forces as inputs.

A passivity analysis of the pipe model is performed, where the system is found to be input–output passive. By careful discretization, this property can be preserved, and the closed–loop system will be stable. This model feature indicates that it may be a suitable candidate for implementation in a model–based controller. The passivity analysis is extended to the complete system including the vessel as the upper boundary condition. This result is a necessary property for implementing the model in a model–based controller.

6.2 Model Properties

RIFLEX is a recognized FEM program for static and dynamic analysis of slender marine structures developed by MARINTEK and SINTEF in cooperation with the Norwegian University of Science and Technology (NTNU) as a joint industry project. RIFLEX currently holds an international leading position in dynamic FEM analysis for slender marine structures, and is the ultimate benchmark for the pipe formulation proposed in this thesis. The model proposed in this chapter

has similarities with RIFLEX. However, there are differences that justifies the development of a new formulation.

RIFLEX is a classical FEM code, where the equations of motion are derived based on Lagrangian mechanics, which following the development of quantum mechanics dominated in the 1960s. The slender structure is divided into beam and bar elements, and these elements are based on small strain theory. From this choice of elements, RIFLEX is not capable of computing the shear forces on each elements. The procedure for solving the equations is to use generalized coordinates, and solved the equations by linearizing the dynamics at the current time step in order to compute an increment. This increment is then used to compute the solution for the next time step, and the procedure is then repeated for each time step.

The equations of motion for the proposed model are on the Newton–Euler form as the linear and angular momentum balance equations for the elastic beam. The Newton–Euler form was favored over the Lagrangian form in the development of robotics in the 1970s and 1980s, and still has a strong position. This form allows external forces, and forces as boundary conditions, to be added directly. Compared to RIFLEX, the proposed model applies a different finite strain beam formulation, which is capable of undergoing finite shearing in addition to finite extension, twisting and bending (Simo, 1985). The complete PDE model is then completely semi–discretized in space, and an explicit set of ordinary differential equations (ODE) are generated. This semi–discretized model can then be solved by using standard integrators for time.

Both the proposed model and RIFLEX are based on a PDE description for the beam elements, and they apply a Galerkin method to derive the FEM model. The most important difference is in the discretization and derivation of the final nonlinear FEM model. The set of ODEs generated from the proposed model are directly applicable for simulation and control applications. RIFLEX performs discretization in one step, and the explicit set of ODEs are not available, except for on incremental form. Also, by linearizing the equations of motion in RIFLEX, the energy property of the system is lost. In the proposed model, linearizing is avoided to preserve this property.

This formulation will have several applications related to dynamic pipeline installation analysis, e.g., simulation of the installation operation, operabilitiy analysis, HIL testing for vessel control systems, and pipelay operation automation. This can also be extended to encompass model–based controllers and observers. It seems also plausible that the model is not limited to pipelines, but is valid for many slender marine structures.

6.3 Mathematical Model

The model of the pipe extends the nonlinear beam formulation developed and investigated by Simo et al. in a series of papers (Simo, 1985; Simo and Vu–Quoc, 1986; Simo and Vu–Quoc, 1988; Simo et al., 1995). The formulation is a reparametrization of the formulation originally developed by Reissner (1982), where this model again can be regarded as a generalization of a three–dimensional extension of the

classical Kirchhoff–Love rod model (Love, 1944). The extension includes finite extension and finite shearing of the rod. New to the model in this paper is the hydrodynamic and hydrostatic effects caused by the marine environment as well as the seabed interaction.

A vessel model in the time domain, suitable for low speed maneuvering and station keeping, is fixed to the surface end of the pipe string as the upper boundary condition. The vessel model is obtained by considering the forces and moments on a rigid body as well as hydrodynamic radiation forces and wave loads and the resulting state space model is a system of ordinary differential equations in the time domain.

6.3.1 Reference Frames

Three Cartesian reference frames denoted by $\boldsymbol{e}$, $\boldsymbol{t}$ and $\boldsymbol{b}$ are required in the development of the pipelay system model, see Figure 6.1. Let $\boldsymbol{e}$ be an inertial frame with base $\boldsymbol{e}_1, \boldsymbol{e}_2, \boldsymbol{e}_3$, where the origin O_e is fixed to the seabed at $S = 0$. Let $\boldsymbol{t}(S)$ be a body–fixed frame with base $\boldsymbol{t}_1(S), \boldsymbol{t}_2(S), \boldsymbol{t}_3(S)$ and origin $O_t(S)$ located at the centroid of the pipe cross–section at S, where $S \in [0, L]$ is the scalar spatial pipe variable, and L is the total length of the undeformed pipe. The base vector $\boldsymbol{t}_1(S)$ is directed normal to the cross–section plane, and $\boldsymbol{t}_2(S)$ and $\boldsymbol{t}_3(S)$ are directed along the principal axis of it. Let $\boldsymbol{b}$ be body–fixed with origin O_b at the pipelay vessel center of mass, and with its basis $\boldsymbol{b}_1, \boldsymbol{b}_2, \boldsymbol{b}_3$ along the principle axes of symmetry for the vessel, in accordance with (SNAME, 1950). The $\boldsymbol{e}$ and $\boldsymbol{t}$ frames are frequently referred to as the *spatial* and *material* frames, respectivly.

Transformations between the defined frames $\boldsymbol{e}$, $\boldsymbol{t}$ and $\boldsymbol{b}$ are handled by the rotation matrices

$$\boldsymbol{R}_t^e(S), \boldsymbol{R}_b^e, \boldsymbol{R}_b^t \in SO(3), \tag{6.1}$$

where e.g. $\boldsymbol{R}_t^e$ transforms coordinate vectors from frame $\boldsymbol{t}$ to frame $\boldsymbol{e}$. Equivalent interpretations are given for $\boldsymbol{R}_b^e$ and $\boldsymbol{R}_b^t$ such that

$$\boldsymbol{t}_i^e(S) = \boldsymbol{R}_t^e(S)\boldsymbol{e}_i^e, \quad \boldsymbol{b}_i^e = \boldsymbol{R}_b^e\boldsymbol{e}_i^e, \quad \boldsymbol{b}_i^t = \boldsymbol{R}_b^t\boldsymbol{t}_i^t. \tag{6.2}$$

6.3.2 Model Preliminaries

From a classical point of view the pipeline can be considered similar to a hollow rod, a three–dimensional slender body with uniform density and circular cross–sections. The reference configuration of the pipe is described by a smooth curve $\boldsymbol{\varphi}_r$, connecting the centroids of the cross–section planes, where the tangent of $\boldsymbol{\varphi}_r$ is normal to each cross–section, see Figure 6.2. Any configuration of the pipe can then be given by a smooth curve $\boldsymbol{\varphi} : [0, L] \to \mathbb{R}^3$, the so–called *line of centroids*. The cross–sections are assumed to remain unchanged in shape while the pipe is undergoing motion, but the assumption that the cross–sections remain normal to the tangent $\partial_S\boldsymbol{\varphi}$ known from the Euler–Bernoulli beam theory is relaxed to account for shearing effects. The position of any point along the line of centroids is given by $\boldsymbol{\varphi}(S)$, and the orientation of the cross–section at $\boldsymbol{\varphi}(S)$ is given by $\boldsymbol{R}_t^e(S)$. Hence, the configurations of the pipe are completely defined by specifying $\boldsymbol{\varphi}(S, t)$ and

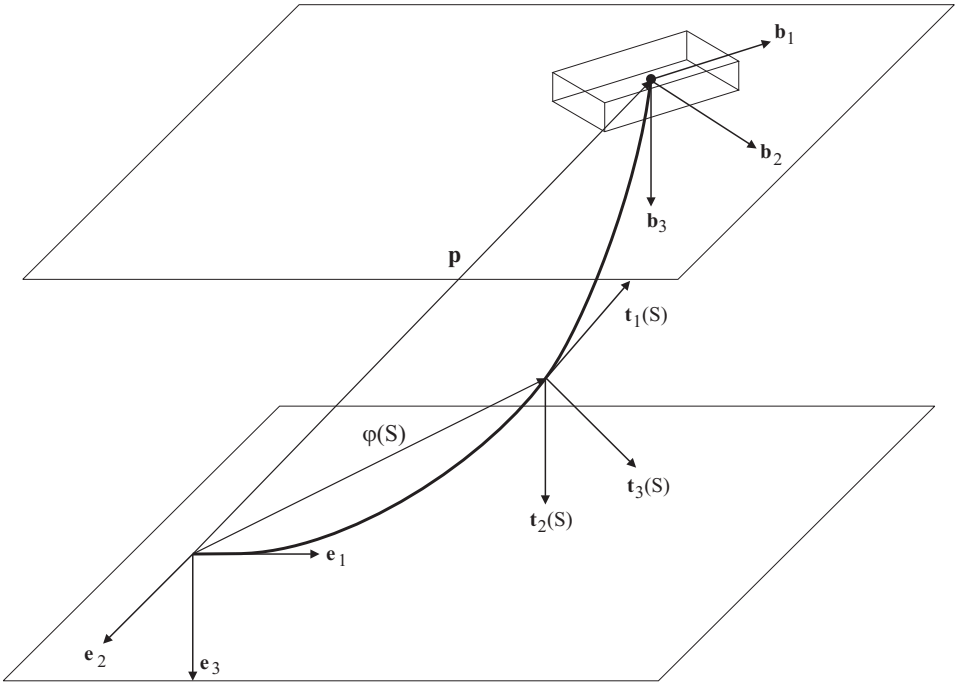

Figure 6.1: Illustration of a J–lay installation in three dimensions with the three reference frames applied. The position of the pipelay vessel center of mass, illustrated by the box, is in the spatial frame $\boldsymbol{e}$ given by $\boldsymbol{p}$.

$\boldsymbol{R}_t^e(S,t)$ along the material variable S and time t. The *configuration space* for the elastic pipe is given by

$$\mathcal{C} \triangleq \left\{ (\boldsymbol{\varphi}, \boldsymbol{R}_t^e) \,|S \in [0,L] \to \mathbb{R}^3 \times SO(3) \,|\, \langle \partial_S \boldsymbol{\varphi}(S), \boldsymbol{R}_t^e \boldsymbol{e}_1^e \rangle > 0 \right\}, \tag{6.3}$$

and the reference configuration is taken as $\left(\boldsymbol{\varphi}_r, \boldsymbol{R}_{t,r}^e\right) \in \mathcal{C}$ such that

$$\boldsymbol{\varphi}_r(S) = S\boldsymbol{e}_1^e, \quad \boldsymbol{R}_{t,r}^e(S) = \boldsymbol{I}_{3\times 3}. \tag{6.4}$$

The pipe is a continuous elastic body, where the matrix $\boldsymbol{R}_t^e(S,t)$ is used to represent the orientation of the pipe cross–section at position $\boldsymbol{\varphi}(S,t)$ along the pipe. Parametrization of $\boldsymbol{R}_t^e(S,t)$ is not performed until the PDE is discretized in S as part of implementing the pipe model in Chapter 7. The arguments of $\boldsymbol{R}_t^e(S,t)$ are omitted for the remainder of this thesis for readability.

6.3.3 Kinematics

The partial derivatives of $\boldsymbol{\varphi}(S,t)$ and $\boldsymbol{R}_t^e(S,t)$ with respect to time t and space S (curve parameter), and the material stress resultant and stress couple are derived in this section.

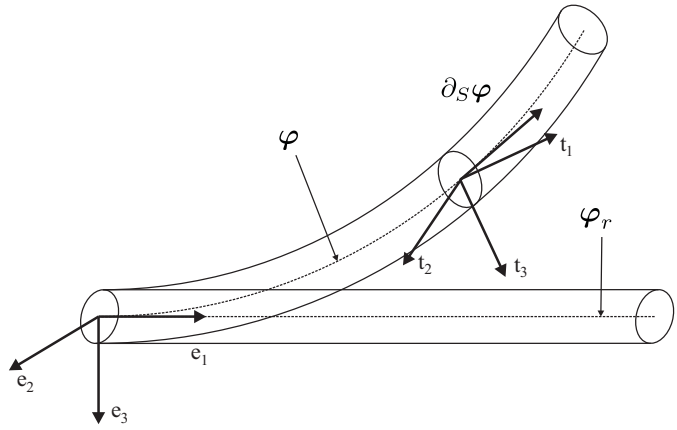

Figure 6.2: The pipe configuration is given by the line of centroids $\boldsymbol{\varphi}$, where the reference configuration is given as $\boldsymbol{\varphi}_r$. The cross–section of the pipe at $\boldsymbol{\varphi}(S)$ is spanned by $\boldsymbol{t}_2(S)$ and $\boldsymbol{t}_3(S)$.

Time and Space Derivatives

Differentiating (6.2) with respect to time t yields

$$\dot{\boldsymbol{t}}_i^e = \boldsymbol{S}\left(\mathbf{w}^e\right)\boldsymbol{t}_i^e, \quad \boldsymbol{S}\left(\mathbf{w}^e\right) = \dot{\boldsymbol{R}}_t^e\left(\boldsymbol{R}_t^e\right)^{\mathrm{T}}, \tag{6.5}$$

where $\boldsymbol{S}(\cdot) : \mathbb{R}^3 \to T_I SO(3)$, is the skew–symmetric map, defined as

$$\boldsymbol{S}(\mathbf{v}) \triangleq \begin{bmatrix} 0 & -v_3 & v_2 \\ v_3 & 0 & -v_1 \\ -v_2 & v_1 & 0 \end{bmatrix}, \quad \mathbf{v} \in \mathbb{R}^3. \tag{6.6}$$

The *spin* of the moving frame is defined as the skew–symmetric tensor $\boldsymbol{S}\left(\mathbf{w}^e(S,t)\right)$, and the associated axial vector $\mathbf{w}^e(S,t)$ defines the *vorticity*. The time derivative of $\boldsymbol{R}_t^e$ is thus given by the two alternative forms

$$\dot{\boldsymbol{R}}_t^e = \boldsymbol{R}_t^e \boldsymbol{S}\left(\mathbf{w}^t\right), \tag{6.7}$$

$$\dot{\boldsymbol{R}}_t^e = \boldsymbol{S}\left(\mathbf{w}^e\right)\boldsymbol{R}_t^e. \tag{6.8}$$

The linear velocity vector is given in the spatial and material frames respectively as

$$\dot{\boldsymbol{\varphi}} \in \mathbb{R}^3, \qquad \boldsymbol{v}^t = \left(\boldsymbol{R}_t^e\right)^{\mathrm{T}}\dot{\boldsymbol{\varphi}}, \tag{6.9}$$

where differentiating (6.9) yields the linear acceleration

$$\ddot{\boldsymbol{\varphi}} \in \mathbb{R}^3, \qquad \dot{\boldsymbol{v}}^t = \left(\boldsymbol{R}_t^e\right)^{\mathrm{T}}\ddot{\boldsymbol{\varphi}} - \left(\boldsymbol{R}_t^e\right)^{\mathrm{T}}\left[\mathbf{w}^e \times \dot{\boldsymbol{\varphi}}\right]. \tag{6.10}$$

The space derivative of the position vector is simply denoted $\partial_S \boldsymbol{\varphi}(S,t) \in \mathbb{R}^3$, and the corresponding material derivative of $\boldsymbol{R}_t^e$ is, like the time derivative, ob-

tained from (6.2). Hence,

$$\partial_S \boldsymbol{R}_t^e = \boldsymbol{R}_t^e \boldsymbol{S}\left(\boldsymbol{\omega}^t\right), \tag{6.11}$$

$$\partial_S \boldsymbol{R}_t^e = \boldsymbol{S}\left(\boldsymbol{\omega}^e\right) \boldsymbol{R}_t^e, \tag{6.12}$$

where $\boldsymbol{\omega}^t$ and $\boldsymbol{\omega}^e$ represent the curvature or bending in material and spatial form, respectively. Since derivation with respect to time and space are commutative operations, evaluating the identity

$$\partial_S\left(\partial_t \boldsymbol{R}_t^e\right) = \partial_t\left(\partial_S \boldsymbol{R}_t^e\right), \tag{6.13}$$

by taking the spatial derivative of (6.7) and the time derivative of (6.11), yields the following expression relating $\boldsymbol{\omega}$ and $\mathbf{w}$,

$$\dot{\boldsymbol{\omega}}^t = \partial_S \mathbf{w}^t + \boldsymbol{\omega}^t \times \mathbf{w}^t = \left(\boldsymbol{R}_t^e\right)^{\mathrm{T}}\left[\partial_S \mathbf{w}^e + \boldsymbol{\omega}^e \times \mathbf{w}^e\right]. \tag{6.14}$$

Stress

The material stress resultant $\boldsymbol{n}^t$ and stress couple $\boldsymbol{m}^t$ are obtained from the bilinear quadratic energy function $\boldsymbol{\Psi}(\boldsymbol{\gamma}^t, \boldsymbol{\omega}^t)$ (Simo, 1985),

$$\boldsymbol{n}^t = \frac{\partial}{\partial \boldsymbol{\gamma}^t}\boldsymbol{\Psi}, \quad \boldsymbol{m}^t = \frac{\partial}{\partial \boldsymbol{\omega}^t}\boldsymbol{\Psi}, \tag{6.15}$$

where

$$\boldsymbol{\Psi}(\boldsymbol{\gamma}^t, \boldsymbol{\omega}^t) \triangleq \frac{1}{2}\begin{bmatrix} \boldsymbol{\gamma}^t \\ \boldsymbol{\omega}^t \end{bmatrix}^{\mathrm{T}} \begin{bmatrix} \boldsymbol{C}_T & \mathbf{0}_{3\times 3} \\ \mathbf{0}_{3\times 3} & \boldsymbol{C}_R \end{bmatrix} \begin{bmatrix} \boldsymbol{\gamma}^t \\ \boldsymbol{\omega}^t \end{bmatrix}, \tag{6.16}$$

and where extension and shearing $\boldsymbol{\gamma}^t$, defined as

$$\boldsymbol{\gamma}^t = \left(\boldsymbol{R}_t^e\right)^{\mathrm{T}}\left(\partial_s \boldsymbol{\varphi} - \boldsymbol{t}_1\right), \tag{6.17}$$

see Figure 6.3, and curvature $\boldsymbol{\omega}^t$ are the material strain measures, and

$$\boldsymbol{C}_T = \operatorname{diag}\left[EA, GA_2, GA_3\right] > 0, \tag{6.18}$$

$$\boldsymbol{C}_R = \operatorname{diag}\left[GJ, EI_2, EI_3\right] > 0. \tag{6.19}$$

The constants E and G are interpreted as the Young's modulus and the shear modulus, A is the cross–sectional area of the pipe, A_2 and A_3 are the effective shear areas, I is the unit polar moment of inertia of the cross–section plane, and J is the Saint Venant torsional modulus. Hence, in material form

$$\boldsymbol{n}^t = \boldsymbol{C}_T \boldsymbol{\gamma}^t, \tag{6.20}$$

$$\boldsymbol{m}^t = \boldsymbol{C}_R \boldsymbol{\omega}^t, \tag{6.21}$$

and in spatial form

$$\boldsymbol{n}^e = \boldsymbol{R}_t^e \boldsymbol{n}^t = \boldsymbol{R}_t^e \boldsymbol{C}_T \left(\boldsymbol{R}_t^e\right)^{\mathrm{T}}\left[\partial_S \boldsymbol{\varphi} - \boldsymbol{t}_1^e\right], \tag{6.22}$$

$$\boldsymbol{m}^e = \boldsymbol{R}_t^e \boldsymbol{m}^t = \boldsymbol{R}_t^e \boldsymbol{C}_R \left(\boldsymbol{R}_t^e\right)^{\mathrm{T}} \boldsymbol{\omega}^e. \tag{6.23}$$

Taking the time derivative of (6.17) yields $\dot{\boldsymbol{\gamma}}^t$ to be

$$\dot{\boldsymbol{\gamma}}^t = -\boldsymbol{S}\left(\mathbf{w}^t\right)\left(\boldsymbol{R}_t^e\right)^{\mathrm{T}}\left(\partial_S \boldsymbol{\varphi}\right) + \left(\boldsymbol{R}_t^e\right)^{\mathrm{T}}\left(\partial_S \dot{\boldsymbol{\varphi}}\right) = \left(\boldsymbol{R}_t^e\right)^{\mathrm{T}}\left[\partial_S \dot{\boldsymbol{\varphi}} - \mathbf{w}^e \times \left(\partial_S \boldsymbol{\varphi}\right)\right]. \tag{6.24}$$

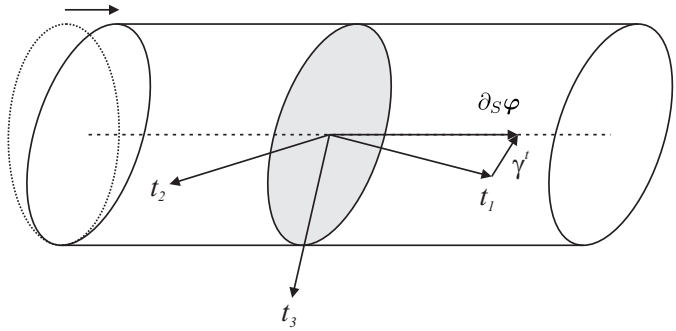

Figure 6.3: Extension and shearing $\boldsymbol{\gamma}^t$ for a pipe cross–section.

6.3.4 Dynamics

The linear and angular momentum balance equations for a nonlinear elastic beam are derived in Simo (1985) as

$$m_P \ddot{\boldsymbol{\varphi}} = \partial_S \boldsymbol{n}^e + \widetilde{\boldsymbol{n}}^e \tag{6.25}$$

$$\boldsymbol{I}_\rho^e \dot{\mathbf{w}}^e + \mathbf{w}^e \times \boldsymbol{I}_\rho^e \mathbf{w}^e = \partial_S \boldsymbol{m}^e + (\partial_S \boldsymbol{\varphi}) \times \boldsymbol{n}^e + \widetilde{\boldsymbol{m}}^e \tag{6.26}$$

where m_P is the mass per unit length, $\widetilde{\boldsymbol{n}}^e$ and $\widetilde{\boldsymbol{m}}^e$ are the resultant external force and torque per unit length, and $\boldsymbol{I}_\rho^e(S,t)$ is the state dependent inertia tensor given by

$$\boldsymbol{I}_\rho^e = \boldsymbol{R}_t^e \boldsymbol{J}_\rho^t \left(\boldsymbol{R}_t^e\right)^{\mathrm{T}}, \quad \boldsymbol{J}_\rho^t = \operatorname{diag}\left[J_1, J_2, J_3\right] \geq 0, \tag{6.27}$$

where $\boldsymbol{J}_\rho^t$ is the constant inertia tensor for the cross–sections in the reference configuration.

This model can be adopted for pipes submerged in water by approximating $\widetilde{\boldsymbol{n}}^e$ and $\widetilde{\boldsymbol{m}}^e$ by

$$\widetilde{\boldsymbol{n}}^e = -\boldsymbol{f}_g^e - \boldsymbol{f}_d^e - \boldsymbol{f}_s^e \tag{6.28}$$

$$\widetilde{\boldsymbol{m}}^e = -\boldsymbol{D}_R \mathbf{w}^e \tag{6.29}$$

where

$\boldsymbol{f}_g^e$ – restoring forces vector (gravitation and buoyancy),
$\boldsymbol{f}_d^e$ – transversal hydrodynamic damping,
$\boldsymbol{D}_R$ – constant damping matrix of rotation,
$\boldsymbol{f}_s^e$ – seabed interaction force.

Hence, the equations of motion for a nonlinear elastic pipe submerged in water, given as a PDE in the spatial frame, is found by substituting (6.28)–(6.29) into (6.25)–(6.26),

$$m_P \ddot{\boldsymbol{\varphi}} = \partial_S \boldsymbol{n}^e - \boldsymbol{f}_g^e - \boldsymbol{f}_d^e - \boldsymbol{f}_s^e \tag{6.30}$$

$$\boldsymbol{I}_\rho^e \dot{\mathbf{w}}^e + \mathbf{w}^e \times \boldsymbol{I}_\rho^e \mathbf{w}^e = \partial_S \boldsymbol{m}^e + (\partial_S \boldsymbol{\varphi}) \times \boldsymbol{n}^e - \boldsymbol{D}_R \mathbf{w}^e. \tag{6.31}$$

Hydrostatic Restoring Terms

The pipe is assumed to be completely submerged in water such that the restoring forces per unit length are the sum of the gravitation and the buoyancy as defined by Archimedes. The restoring forces acts only in the vertical direction $\boldsymbol{e}_3$, and is given in $\boldsymbol{e}$ by

$$\boldsymbol{f}_g^e = (m_P - \rho_w A)\, g \boldsymbol{e}_3, \tag{6.32}$$

where ρ_w is the mass density of ambient water, A is the pipe cross–section area and g is the acceleration of gravity.

Hydrodynamic Damping Terms

The hydrodynamic forces on a submerged slender body are given by Morison's equation as the sum of added mass and drag (Morison et al., 1950). For applications involving low velocities such as e.g., risers, mooring lines and pipelay operations, the added mass term is small and can be neglected. An estimate for the remaining drag forces acting on a cylindrical shape in three dimensions are

$$\boldsymbol{f}_d^t\left(\boldsymbol{v}_r^t\right) = \frac{1}{2} d_o \rho_w \boldsymbol{D}_T \begin{bmatrix} \left|v_{r_1}^t\right| v_{r_1}^t \\ \left(\left(v_{r_2}^t\right)^2 + \left(v_{r_3}^t\right)^2\right)^{1/2} v_{r_2}^t \\ \left(\left(v_{r_2}^t\right)^2 + \left(v_{r_3}^t\right)^2\right)^{1/2} v_{r_3}^t \end{bmatrix}, \tag{6.33}$$

where d_o is the outer pipe diameter and

$$\boldsymbol{D}_T = \mathrm{diag}[D_1, D_2, D_3] \geq 0, \tag{6.34}$$

where $D_1, D_2, D_3 \geq 0$ are damping coefficients, which are constant if a constant Reynold's number is assumed. The vector $\boldsymbol{v}_r^t$ is the relative velocity of the pipe in the water,

$$\boldsymbol{v}_r^t = \left(\boldsymbol{R}_{\boldsymbol{t}}^{\boldsymbol{e}}\right)^{\mathrm{T}} \left(\dot{\boldsymbol{\varphi}}^e - \boldsymbol{v}_c^e\right), \tag{6.35}$$

where $\boldsymbol{v}_c^e = \boldsymbol{v}_c^e\left(\boldsymbol{\varphi}^{\mathrm{T}} \boldsymbol{e}_3, t\right)$ is the water current vector given in the spatial frame. Let the rotational damping in (6.31) be directly proportional to the angular velocity $\mathbf{w}$, where

$$\boldsymbol{D}_R = \mathrm{diag}[D_4, D_5, D_6] \geq 0, \tag{6.36}$$

and where $D_4, D_5, D_6 \geq 0$ are the damping coefficients.

Seabed Interaction

A seabed interaction force is commonly modeled by a spring and damper pair or simply a spring, since the spring effect will usually dominate the damping effect. In this paper the damping effect is neglected, and we propose that the seabed interaction force $\boldsymbol{f}_s^e$ is modeled by a nonlinear spring, acting on the pipeline section

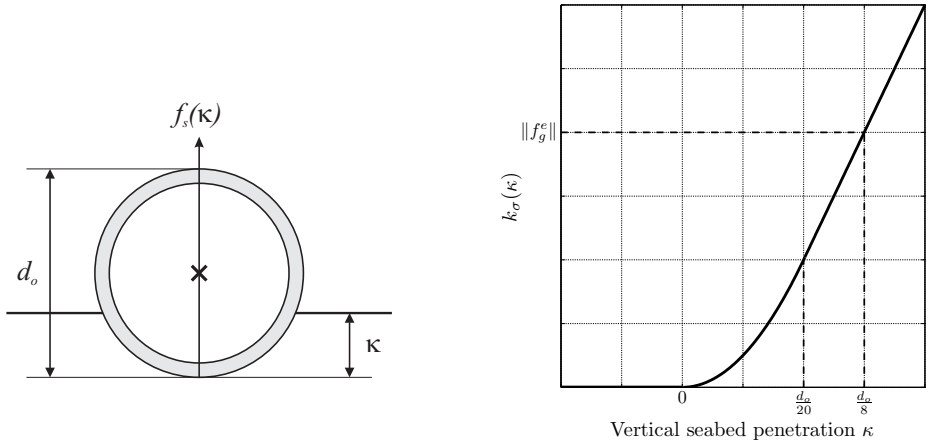

(a) Pipe resting on the seabed.

(b) The nonlinear spring function for seabed penetration.

Figure 6.4: Seabed interaction

that is in contact with the seabed, given by

$$\boldsymbol{f}_s^e = k_\kappa(\kappa)\,\boldsymbol{e}_3, \qquad k_\kappa(\kappa) = \begin{cases} 0 & , \ \kappa < 0 \\ \dfrac{\|\boldsymbol{f}_g^e\|_2}{(d_o/8 - d_o/40)} \dfrac{10\kappa^2}{d_o} & , \ 0 \leqslant \kappa \leqslant d_o/20 \\ \dfrac{\|\boldsymbol{f}_g^e\|_2}{(d_o/8 - d_o/40)}(\kappa - d_o/40) & , \ \kappa > d_o/20, \end{cases} \tag{6.37}$$

where $\kappa = \boldsymbol{\varphi}^{\mathrm{T}}\boldsymbol{e}_3 + d_o/2$ denotes the vertical seabed penetration, see Figure 6.4. The nonlinear spring $\boldsymbol{f}_s^e \in \mathcal{C}^1$ is defined such that the pipe is at rest for seabed penetration equal to $1/8$ of the outer pipe diameter, $\kappa = d_o/8$. The spring becomes linear for $\kappa > d_o/20$ and the constants are chosen so that $\boldsymbol{f}_s^e$ becomes continuously differentiable over $\mathbb{R}$. Seabed friction is not considered in the model.

6.3.5 Boundary Conditions

The model (6.30)–(6.31) is clamped to the seabed at the lower end and fixed to a surface vessel at the upper end. These boundary conditions are presented in this section, mainly focusing on the surface vessel model.

Seabed

The lower end of the pipe is assumed to be fixed to the seabed, and the boundary condition for $S = 0$ is thus given by

$$\boldsymbol{\varphi}(0,t) = \boldsymbol{\varphi}_0 = 0, \quad \boldsymbol{R}_t^e(0,t) = \boldsymbol{R}_{t,0}^e = \boldsymbol{I}_{3\times 3}, \quad \forall\, t. \tag{6.38}$$

Vessel

Consider the pipelay vessel model (3.65) in Chapter 3. This model applies Euler angle parametrization of the vessel orientation in the generalized position vector $\boldsymbol{\eta}$, which is relaxed by (3.66). In the following section an approximation of restoring forces and moments independent of Euler angles, $\boldsymbol{g}(\boldsymbol{\eta}) \to \boldsymbol{g}(\boldsymbol{\phi}, \boldsymbol{R}_t^e)$, are derived.

A metacentric stable surface vessel has restoring forces and moments in heave (z), roll (ϕ) and pitch (θ) that will resist inclinations away from the steady–state equilibrium. The restoring forces and moments will depend on the vessel's metacentric height, the location of the center of gravity, the center of buoyancy, and the shape and size of the water plane, denoted by A_{wp}. For every vessel and load a transversal metacentric height $\overline{GM}_T \in \mathbb{R}$ and a longitudinal metacentric height $\overline{GM}_L \in \mathbb{R}$ can be computed (Fossen, 2002).

The equilibrium in heave is obtained when the gravity and buoyancy forces balance. A force $\boldsymbol{g}_l^e \in \mathbb{R}^3$ is generated to restore this balance if the heave position $\boldsymbol{\varphi}^{\mathrm{T}}(L,t)\,\boldsymbol{e}_3$ changed due to external forces, or the heave equilibrium z_{eq} changes due to e.g. waves. This force is modeled in the $\boldsymbol{e}$ frame as

$$\boldsymbol{g}_l^e = -A_{wp}\rho_w g\left(\boldsymbol{\varphi}^{\mathrm{T}}(L,t)\,\boldsymbol{e}_3 - z_{eq}\right)\boldsymbol{e}_3, \tag{6.39}$$

where the A_{wp} is assumed to be constant for small changes in heave.

From geometric considerations, the moment arms in roll and pitch can be found to be

$$\boldsymbol{r}_r^b = \begin{bmatrix} -\overline{GM}_L \sin\theta \\ \overline{GM}_T \sin\phi \\ 0 \end{bmatrix}. \tag{6.40}$$

The dependence of Euler angles are removed from (6.40) by observing that

$$\sin\theta = -\left(\boldsymbol{R}_b^e \boldsymbol{e}_1\right)^{\mathrm{T}} \boldsymbol{e}_3, \tag{6.41}$$

$$\sin\phi \approx \cos\theta \sin\phi = \left(\boldsymbol{R}_b^e \boldsymbol{e}_2\right)^{\mathrm{T}} \boldsymbol{e}_3, \tag{6.42}$$

where the applied approximation $\cos\theta = 1$ is generally true for small pitch angles, hence (6.40) is approximated without Euler angles as

$$\widetilde{\boldsymbol{r}}_r^b \triangleq \begin{bmatrix} \overline{GM}_L \left(\boldsymbol{R}_b^e \boldsymbol{e}_1\right)^{\mathrm{T}} \boldsymbol{e}_3 \\ \overline{GM}_T \left(\boldsymbol{R}_b^e \boldsymbol{e}_2\right)^{\mathrm{T}} \boldsymbol{e}_3 \\ 0 \end{bmatrix} \approx \boldsymbol{r}_r^b, \tag{6.43}$$

such that the restoring moment term becomes

$$\begin{aligned} \boldsymbol{g}_r^e &= \widetilde{\boldsymbol{r}}_r^e \times \boldsymbol{f}_r^e \\ &= \left(\boldsymbol{R}_b^e \widetilde{\boldsymbol{r}}_r^b\right) \times \left(m_V g \boldsymbol{e}_3\right). \end{aligned} \tag{6.44}$$

It is assumed that there is no moment due to heave. Consequently, the nonlinear restoring forces term of (3.65) is given in the body frame $\boldsymbol{b}$ as

$$\boldsymbol{g}^b\left(\boldsymbol{\varphi}(L,t), \boldsymbol{R}_b^e(t)\right) = \begin{bmatrix} \left(\boldsymbol{R}_b^e\right)^{\mathrm{T}} \boldsymbol{g}_t^e \\ \left(\boldsymbol{R}_b^e\right)^{\mathrm{T}} \boldsymbol{g}_r^e \end{bmatrix}. \tag{6.45}$$

For the remainder of this paper, let the pipe be fixed to the center of gravity of the vessel such that

$$\boldsymbol{\nu} = \begin{bmatrix} (\boldsymbol{R}_b^e)^{\mathrm{T}} \dot{\boldsymbol{\varphi}}(L,t) \\ (\boldsymbol{R}_b^e)^{\mathrm{T}} \mathbf{w}^e(L,t) \end{bmatrix} \quad \text{and} \quad \dot{\boldsymbol{\nu}} = \begin{bmatrix} (\boldsymbol{R}_b^e)^{\mathrm{T}} \ddot{\boldsymbol{\varphi}}(L,t) \\ (\boldsymbol{R}_b^e)^{\mathrm{T}} \dot{\mathbf{w}}^e(L,t) \end{bmatrix}. \tag{6.46}$$

Forces and moments acting between the pipe and the vessel (3.65), are considered as internal forces in the total system, and by Newton's third law the following relationship holds:

$$\begin{bmatrix} \overline{\boldsymbol{n}}^e(L,t) \\ \overline{\boldsymbol{m}}^e(L,t) \end{bmatrix} = -\begin{bmatrix} \boldsymbol{R}_b^e & \mathbf{0}_{3\times3} \\ \mathbf{0}_{3\times3} & \boldsymbol{R}_b^e \end{bmatrix} \boldsymbol{\chi}. \tag{6.47}$$

6.4 Passivity

The passivity properties of the developed model, with and without boundary conditions, are considered in this section. Passivity provides a useful tool for the analysis of nonlinear systems which relates nicely to Lyapunov and $\mathcal{L}_2$ stability (Khalil, 2002). The main passivity theorem states that the negative feedback connection of two passive systems is passive. By proving passivity of the pipelay system and choosing a passive controller, the feedback connection is thus known to be stable, which is necessary for control applications.

Theorem 6.4.1 *The system* (6.30)–(6.31) *is input–output passive, where the input* $\overline{\boldsymbol{\tau}}$ *and output* $\overline{\boldsymbol{\nu}}$ *are taken as*

$$\overline{\boldsymbol{\tau}} \triangleq \left[\overline{\boldsymbol{n}}^e(0,t), \overline{\boldsymbol{m}}^e(0,t), \overline{\boldsymbol{n}}^e(L,t), \overline{\boldsymbol{m}}^e(L,t)\right]^T \in \mathbb{R}^{12} \tag{6.48}$$

$$\overline{\boldsymbol{\nu}} \triangleq \left[-\dot{\boldsymbol{\varphi}}(0,t), -\mathbf{w}^e(0,t), \dot{\boldsymbol{\varphi}}(L,t)\, \mathbf{w}^e(L,t)\right]^T \in \mathbb{R}^{12} \tag{6.49}$$

and assuming that $|v_{c,i}^e| \leq |\dot{\varphi}_i|$, *for* $i = 1, \ldots, 3$ (6.35).

Proof 6.4.1 *The total system energy* $\mathcal{E}_P$ *of* (6.30)–(6.31), *is given by*

$$\mathcal{E}_P = \mathcal{T}_P + \mathcal{U}_P, \tag{6.50}$$

where this pipe energy function is the sum of kinetic energy $\mathcal{T}_P$ *and potential energy* $\mathcal{U}_P$ *(Simo and Vu–Quoc, 1986),*

$$\mathcal{T}_P = \frac{1}{2}\int_0^L m_p \|\dot{\boldsymbol{\varphi}}\|_2^2 + \left\langle \mathbf{w}^e, \boldsymbol{I}_\rho^e \mathbf{w}^e \right\rangle dS, \tag{6.51}$$

$$\mathcal{U}_P = \int_0^L \boldsymbol{\Psi}\left(\boldsymbol{\gamma}^t, \boldsymbol{\omega}^t\right) dS + \int_0^L \left(\left\langle \boldsymbol{f}_g^e, \boldsymbol{\varphi} \right\rangle + \int_0^\kappa k_\kappa(\xi)\, d\xi \right) dS. \tag{6.52}$$

Differentiating (6.50) *with respect to time, the kinetic energy term yields*

$$\dot{\mathcal{T}}_P = \int_0^L \left\langle \dot{\boldsymbol{\varphi}}, m_p \ddot{\boldsymbol{\varphi}} \right\rangle + \left\langle \mathbf{w}^e, \boldsymbol{I}_\rho^e \dot{\mathbf{w}}^e \right\rangle dS, \tag{6.53}$$

which by substituting by (6.30)–(6.31) *can be rewritten as*

$$\dot{\mathcal{T}}_P = \int_0^L \left\langle \dot{\boldsymbol{\varphi}}, \left[\partial_S \boldsymbol{n}^e - \boldsymbol{f}_g^e - \boldsymbol{f}_d^e - \boldsymbol{f}_s^e\right]\right\rangle \, dS + \int_0^L \left\langle \mathbf{w}^e, \left[(\boldsymbol{I}_\rho^e \mathbf{w}^e) \times \mathbf{w}^e + \partial_S \boldsymbol{m}^e + (\partial_S \boldsymbol{\varphi}) \times \boldsymbol{n}^e - \boldsymbol{D}_R \mathbf{w}^e\right]\right\rangle \, dS. \tag{6.54}$$

The potential energy rate of change yields by differentiation

$$\dot{\mathcal{U}}_P = \int_0^L \left\langle \boldsymbol{n}^t, \partial_t \boldsymbol{\gamma}^t \right\rangle + \left\langle \boldsymbol{m}^t, \partial_t \boldsymbol{\omega}^t \right\rangle \, dS + \int_0^L \left\langle \boldsymbol{f}_g^e, \dot{\boldsymbol{\varphi}} \right\rangle + \left\langle \boldsymbol{f}_s^e, \dot{\boldsymbol{\varphi}} \right\rangle \, dS \tag{6.55}$$

which by substituton of (6.24) *for* $\partial_t \boldsymbol{\gamma}^t$ *and* (6.14) *for* $\partial_t \boldsymbol{\omega}^t$*, is rewritten as*

$$\dot{\mathcal{U}}_P = \int_0^L \langle \boldsymbol{n}^e, [\partial_S \dot{\boldsymbol{\varphi}} - (\mathbf{w}^e \times (\partial_S \boldsymbol{\varphi}))] \rangle \, dS + \int_0^L \left\langle \boldsymbol{m}^t, \left[\partial_S \mathbf{w}^t + (\boldsymbol{\omega}^t \times \mathbf{w}^t)\right]\right\rangle \, dS + \int_0^L \left\langle \boldsymbol{f}_g^e, \dot{\boldsymbol{\varphi}} \right\rangle + \langle \boldsymbol{f}_s^e, \dot{\boldsymbol{\varphi}} \rangle \, dS. \tag{6.56}$$

Since

$$\partial_S \mathbf{w}^e = \partial_S \left(\boldsymbol{R}_t^e \mathbf{w}^t\right) = \boldsymbol{R}_t^e \boldsymbol{S}\left(\boldsymbol{\omega}^t\right) \mathbf{w}^t + \boldsymbol{R}_t^e \partial_S \mathbf{w}^t = \boldsymbol{R}_t^e \left[\partial_S \mathbf{w}^t + \left(\boldsymbol{\omega}^t \times \mathbf{w}^t\right)\right], \tag{6.57}$$

and the fact that $\left\langle \boldsymbol{m}^t, (\boldsymbol{R}_t^e)^T \partial_S \mathbf{w}^e \right\rangle = \langle \boldsymbol{m}^e, \partial_S \mathbf{w}^e \rangle$*, the second term in* (6.56) *is simplified, and by partial integration, the equation* (6.56) *is finally rewritten as*

$$\begin{aligned} \dot{\mathcal{U}}_P = \; & \langle \overline{\boldsymbol{n}}^e, \dot{\boldsymbol{\varphi}} \rangle \Big|_0^L + \langle \overline{\boldsymbol{m}}^e, \mathbf{w}^e \rangle \Big|_0^L \\ & - \int_0^L \langle \partial_S \boldsymbol{n}^e, \dot{\boldsymbol{\varphi}} \rangle + \langle \partial_S \boldsymbol{m}^e, \mathbf{w}^e \rangle + \langle \mathbf{w}^e, (\partial_S \boldsymbol{\varphi}) \times \boldsymbol{n}^e \rangle \, dS \\ & + \int_0^L \left\langle \boldsymbol{f}_g^e, \dot{\boldsymbol{\varphi}} \right\rangle + \langle \boldsymbol{f}_s^e, \dot{\boldsymbol{\varphi}} \rangle \, dS. \end{aligned} \tag{6.58}$$

Hence, the change of energy of the pipe string $\dot{\mathcal{E}}_P$ *can then be found by summing* (6.54) *and* (6.58) *as*

$$\dot{\mathcal{E}}_P = \langle \overline{\boldsymbol{n}}^e, \dot{\boldsymbol{\varphi}} \rangle \Big|_0^L + \langle \overline{\boldsymbol{m}}^e, \mathbf{w}^e \rangle \Big|_0^L - \int_0^L \langle \dot{\boldsymbol{\varphi}}, \boldsymbol{f}_d^e \rangle \, dS - \int_0^L \langle \mathbf{w}^e, \boldsymbol{D}_R \mathbf{w}^e \rangle \, dS, \tag{6.59}$$

where the energy is seen to depend on the boundary conditions and the transversal and rotational damping. Investigating the integral term for the rotational damping it is readily seen that

$$\int_0^L \langle \mathbf{w}^e, \boldsymbol{D}_R \mathbf{w}^e \rangle \, dS = \int_0^L \left(\sum_{i=1}^{3} D_{i+3} \left(\mathbf{w}_i^e \right)^2 \right) dS \geq 0, \quad \forall \, \mathbf{w}^e, \tag{6.60}$$

such that this term will always dissipate energy. The restoring term is rewritten into

$$\int_0^L \langle \dot{\boldsymbol{\varphi}}, \boldsymbol{f}_d^e \rangle \, dS = \frac{1}{2} d \rho_w \int_0^L \langle \dot{\boldsymbol{\varphi}}, \boldsymbol{\Pi} (\dot{\boldsymbol{\varphi}} - \boldsymbol{v}_c^e) \rangle \, dS \geq 0, \quad \forall \, \left| v_{c,i}^e \right| \leq |\dot{\varphi}_i| \,, \tag{6.61}$$

where

$$\boldsymbol{\Pi} = \boldsymbol{R}_t^e \boldsymbol{D}_T \boldsymbol{\Gamma} \left(\boldsymbol{R}_t^e \right)^T \geq 0, \tag{6.62}$$

$$\boldsymbol{\Gamma} = \operatorname{diag} \left[\left| v_{r_1}^t \right|, \left(\left(v_{r_2}^t \right)^2 + \left(v_{r_3}^t \right)^2 \right)^{1/2}, \left(\left(v_{r_2}^t \right)^2 + \left(v_{r_3}^t \right)^2 \right)^{1/2} \right] \geq 0. \tag{6.63}$$

Hence, from (6.59) *and the assumption* $\left| v_{c,i}^e \right| \leq |\dot{\varphi}_i|$*, it follows*

$$\dot{\mathcal{E}}_P \leq \langle \overline{\boldsymbol{n}}^e, \dot{\boldsymbol{\varphi}} \rangle \Big|_0^L + \langle \overline{\boldsymbol{m}}^e, \mathbf{w}^e \rangle \Big|_0^L = \overline{\boldsymbol{\tau}}^T \overline{\boldsymbol{\nu}}. \tag{6.64}$$

□

This theorem can be extended to also include the boundary conditions.

Theorem 6.4.2 *The system* (6.30)–(6.31) *with boundary condition* (6.38) *for* $S = 0$ *and* (6.47) *for* $S = L$ *is input–output passive, with input* $\boldsymbol{\tau}$ *and output* $\boldsymbol{\nu}$ (3.46)*, and assuming that* $|v_{c,i}^e| \leq |\dot{\varphi}_i|$*, for* $i = 1, \ldots, 3$*.*

Proof 6.4.2 *The total energy* $\mathcal{E}$ *of the pipelay system is given by the sum of the total energy of the pipe* $\mathcal{E}_P$ *and the surface vessel* $\mathcal{E}_V$*,*

$$\mathcal{E} = \mathcal{E}_P + \mathcal{E}_V \geq 0, \tag{6.65}$$

$$\mathcal{E}_V = \mathcal{T}_V + \mathcal{U}_V, \tag{6.66}$$

The vessel energy function is the sum of kinetic $\mathcal{T}_V$ *and potential energy* $\mathcal{U}_V$*,*

$$\mathcal{T}_V = \frac{1}{2} \boldsymbol{\nu}^T \boldsymbol{M} \boldsymbol{\nu} \tag{6.67}$$

$$\begin{aligned} \mathcal{U}_V = {} & \frac{1}{2} A_{wp} \rho_w g \left(\boldsymbol{\varphi}^T (L,t) \, e_3 + h_{ref} \right)^2 + \\ & \frac{1}{2} m_V g \left\{ \overline{GM}_L \left[\left(\boldsymbol{R}_b^e \boldsymbol{e}_1 \right)^T \boldsymbol{e}_3 \right]^2 + \overline{GM}_T \left[\left(\boldsymbol{R}_b^e \boldsymbol{e}_2 \right)^T \boldsymbol{e}_3 \right]^2 \right\}, \end{aligned} \tag{6.68}$$

where $\mathcal{U}_V$ is the sum of the potential functions derived from (6.39) *and* (6.45)*. By differentiating* (6.67) *and* (6.68) *with respect to time, and substituting in* (3.65) *and finally applying property* ***P2****, the change of energy for the vessel is found to be*

$$\dot{\mathcal{T}}_V = \boldsymbol{\nu}^T(\boldsymbol{\tau} + \boldsymbol{\chi}) - \boldsymbol{\nu}^T \boldsymbol{D}\boldsymbol{\nu} - \boldsymbol{\nu}^T \boldsymbol{g}^b, \tag{6.69}$$

$$\dot{\mathcal{U}}_V = \boldsymbol{\nu}^T \boldsymbol{g}^b, \tag{6.70}$$

which is summed to express $\dot{\mathcal{E}}_V$ by

$$\dot{\mathcal{E}}_V = \boldsymbol{\nu}^T(\boldsymbol{\tau} + \boldsymbol{\chi}) - \boldsymbol{\nu}^T \boldsymbol{D}\boldsymbol{\nu}. \tag{6.71}$$

Applying property ***P3*** *to* (6.71) *yields $\dot{\mathcal{E}}_V \leq \boldsymbol{\nu}^T(\boldsymbol{\tau} + \boldsymbol{\chi})$ showing that the vessel is itself input–output passive with input $(\boldsymbol{\tau} + \boldsymbol{\chi})$ and output $\boldsymbol{\nu}$. Hence, the derivative of the energy* (6.65) *can be found by summing* (6.59) *and* (6.71)*,*

$$\begin{aligned}\dot{\mathcal{E}} = &\langle \overline{\boldsymbol{n}}^e, \dot{\boldsymbol{\varphi}} \rangle \,|_0^L + \langle \overline{\boldsymbol{m}}^e, \mathbf{w}^e \rangle \,|_0^L - \int_0^L \langle \dot{\boldsymbol{\varphi}}, \boldsymbol{f}_d^e \rangle \, dS \\ &- \int_0^L \langle \mathbf{w}^e, \boldsymbol{D}_R \mathbf{w}^e \rangle \, dS + \boldsymbol{\nu}^T(\boldsymbol{\tau} + \boldsymbol{\chi}) - \boldsymbol{\nu}^T \boldsymbol{D}\boldsymbol{\nu},\end{aligned} \tag{6.72}$$

where the lower boundary condition $S = 0$, known from (6.38)*, implies*

$$\langle \overline{\boldsymbol{n}}^e, \dot{\boldsymbol{\varphi}} \rangle \,|_0 = \langle \overline{\boldsymbol{m}}^e, \mathbf{w}^e \rangle \,|_0 = 0, \tag{6.73}$$

and the upper boundary condition is given by (6.47) *where the pipe is connected to the vessel in the center of gravity, as defined in* (6.46)*, such that the total rate of change of energy of the pipe and vessel system reduces to*

$$\dot{\mathcal{E}} = -\int_0^L \langle \dot{\boldsymbol{\varphi}}, \boldsymbol{f}_d^e \rangle \, dS - \int_0^L \langle \mathbf{w}^e, \boldsymbol{D}_R \mathbf{w}^e \rangle \, dS - \boldsymbol{\nu}^T \boldsymbol{D}\boldsymbol{\nu} + \boldsymbol{\nu}^T \boldsymbol{\tau}, \tag{6.74}$$

which implies that $\dot{\mathcal{E}} \leq \boldsymbol{\nu}^T \boldsymbol{\tau}$, and the system is input–output passive.

□

Corollary 6.4.3 *Finally, it can be concluded the combined system of pipeline and vessel is stable since $\mathcal{E} \geq 0$, $\|\mathcal{E}\| \to \infty$ due to unbounded system states, and $\dot{\mathcal{E}} \leq 0$ which implies that*

$$\mathcal{E}(t) - \mathcal{E}(0) \leq 0. \tag{6.75}$$

If a *passive* controller $\boldsymbol{\tau}$ is applied, this analysis shows that the complete system is input–output passive and stable.

6.5 Position Controller

A PDE formulation for an elastic pipeline and surface vessel has been developed so far in this chapter. In order to get a complete closed–loop system, as illustrated in Figure 2.7 in Section 2.3, only the controller is missing. Hence, a nonlinear DP controller is suggested here. In the motion control hierarchy, see Figure 2.8, the controller is found at the *intermediate level of control*, taking position and velocity references as inputs. This controller is described further in (Jensen et al., 2009).

6.5.1 Nonlinear PID–controller

A nonlinear PID–controller for computing the vector of control inputs $\boldsymbol{\tau}$ for the vessel (3.65) taken the desired vessel position $\boldsymbol{\eta}_{ref}(t)$ and velocity $\boldsymbol{\nu}_{ref}(t)$ as inputs, is suggested,

$$\boldsymbol{\tau} = -\mathbf{J}^{\mathrm{T}}(\boldsymbol{\eta})\,\boldsymbol{\tau}_{PID}, \tag{6.76}$$

$$\boldsymbol{\tau}_{PID} = \mathbf{K}_p\tilde{\boldsymbol{\eta}} + \mathbf{K}_d\dot{\tilde{\boldsymbol{\eta}}} + \mathbf{K}_i \int_{t_0}^{t} \tilde{\boldsymbol{\eta}}(\tau)\, d\tau, \tag{6.77}$$

where the position error is given by $\tilde{\boldsymbol{\eta}} = \boldsymbol{\eta} - \boldsymbol{\eta}_{ref}$, and the matrices $\mathbf{K}_p$, $\mathbf{K}_d$, $\mathbf{K}_i \in \mathbb{R}^{6\times 6}$ are controller gains.

For COTS DP controllers, 1st order waves are removed by using a wave filter. The integrator term of (6.77) removes the bias introduced by the current and 2nd order waves, which have a non–zero mean. It is common to add feedforward terms to the controller to account for the wind, and in pipelaying operations, for the pipe tension, since these can be measured. If the pipe tension can not be measured, it can be computed by e.g., the robotic tension model (5.77), developed in Chapter 5. However, due to the feedback term, these terms are optional. Assuming the vessel to be fully actuated, the available control inputs are the vessel thrusters, which are limited to surge, sway and yaw.

By choosing a passive controller such as a PD–controller ($\mathbf{K}_i = \mathbf{0}_{3\times 3}$), the closed loop system is stable by the condition of feedback connection of two passive systems, found in Theorem 6.1 in Khalil (2002). However, this property is generally not guaranteed for the PID–controller due to the integrator term, unless the integral action term of the controller is bounded.

6.5.2 Simulations

In the dynamic validation of the proposed PDE pipe model in Chapter 7 (6.77) will be applied. To validate the performance of the controller, this simple simulation scenario is considered here:

- $t = 0\,s$ – The static equilibrium for the pipe and vessel, $\boldsymbol{\eta}_0$, is taken as the initial condition. No environmental loads or control loads are applied, and the vessel remains in this equilibrium.

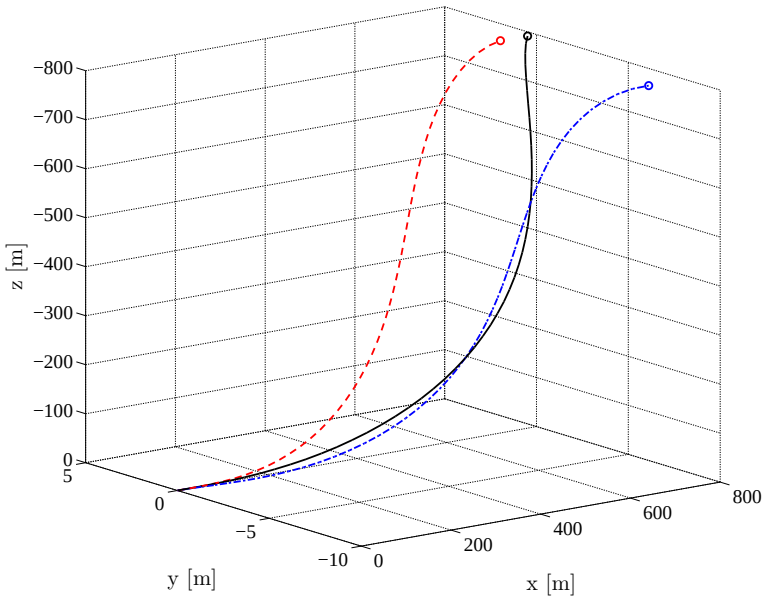

Figure 6.5: The dashed red line is the initial static configuration. Dash dot blue line is at $t = 30s$ where the controller is turned on. Solid black line is configuration at $t = 200s$.

- $t = 10\,s$ – A current load in the $-y$ direction is applied to the vessel and the pipe. The current has a linearly shared current velocity profile with surface velocity $0.8\,m/s$.
- $t = 30\,s$ – The controller is turned on, and starts to move the pipelay vessel to the desired surface reference position $\boldsymbol{\eta}_{ref}$.
- $t = 200\,s$ – The simulation is finished.

The configurations at the different times are illustrated in Figure 6.5. The parameters required for simulation are listed in Table 6.1. A more extensive list of parameters are found in Jensen et al. (2009). The simulation scenario is simulated twice, applying a PD–controller the first time, and a PID–controller the second time.

PD–controller

Figure 6.6 show the elements of $\boldsymbol{\eta}$ for the vessel when the PD–controller is applied with the following controller gains:

$$\mathbf{K}_p = \text{diag}[0.5 \cdot 10^6, 0.5 \cdot 10^6, 0, 0, 0, 0]^{\mathrm{T}}, \tag{6.78}$$

$$\mathbf{K}_d = \text{diag}[0.4 \cdot 10^7, 0.4 \cdot 10^7, 0, 0, 0, 0]^{\mathrm{T}}. \tag{6.79}$$

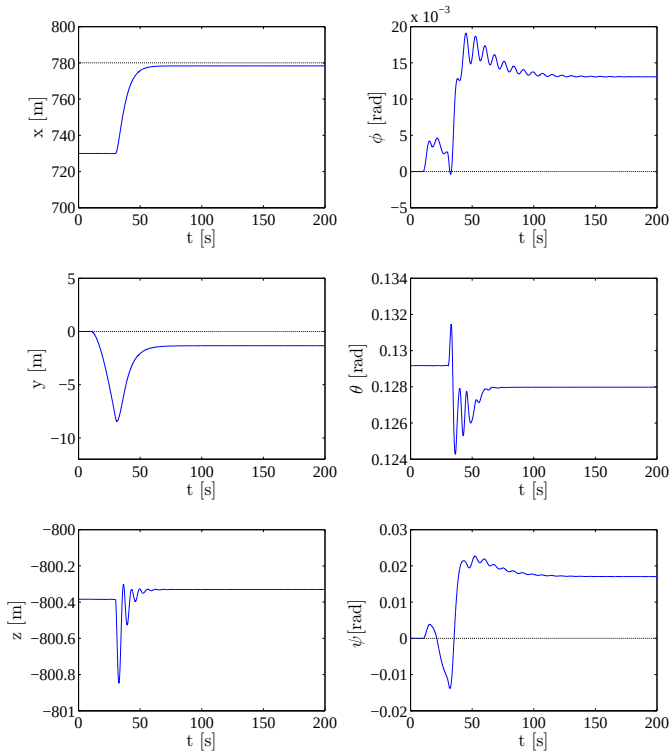

Figure 6.6: *PD–controller* – The position and orientation $\boldsymbol{\eta}(t)$ over the course of the simulation. The controller is enabled at $t = 30\,s$. Note the bias in sway, y.

PID–controller

Applying a PID–controller, the integrator term cancels the bias terms seen in the PD–controller simulation. In Figure 6.7 a PID–controller has been applied with the following controller gains:

$$\mathbf{K}_p = \mathrm{diag}[0.4 \cdot 10^6, 0.4 \cdot 10^6, 0, 0, 0, 10^5]^{\mathrm{T}}, \tag{6.80}$$

$$\mathbf{K}_d = \mathrm{diag}[0.5 \cdot 10^7, 0.4 \cdot 10^7, 0, 0, 0, 10^5]^{\mathrm{T}}, \tag{6.81}$$

$$\mathbf{K}_i = \mathrm{diag}[0.1 \cdot 10^4, 0.5 \cdot 10^4, 0, 0, 0, 0.2 \cdot 10^4]^{\mathrm{T}}. \tag{6.82}$$

6.6 Conclusions

A nonlinear dynamic pipe model for a freely suspended pipe string with bending stiffness has been developed. This pipe model has been shown to be input–output passive by a passivity check. Further, the model has been extended to include the dynamics of a surface pipelay vessel, and passivity and stability of the combined

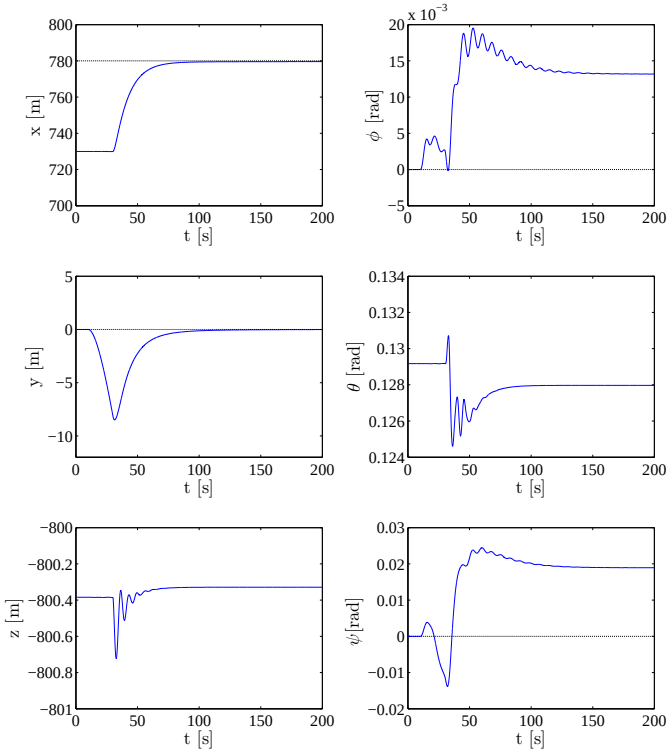

Figure 6.7: *PID–controller* – The position and orientation $\boldsymbol{\eta}(t)$ over the course of the simulation. The integrator term removes the bias in sway, y, seen in the PD–controller simulation.

system has been shown from considering the total energy of the system. Further extensions to the model to improve the accurate and usability are:

- Include the pipe *added mass*.
- Include lateral and axial seabed friction.
- Uneven seabed by using bathymatri maps.
- pipe elongation my relaxing the fixed pipe length property so that $L = L\,(t)$.
- Introduce a small linear damping in the $\boldsymbol{f}_d^e$ to ensure damping effect for very small velocities.

Table 6.1: List of simulation parameters.

Parameter	*Notation*	*Value*	*Unit*
Pipe properties			
Outer pipe diameter	d_o	0.60	m
Wall thickness	WT	0.03	m
Undeformed length	L	1200	m
Water depth	d	800	m
Lift–off angle	β	0	rad
Inertia tensor	$\boldsymbol{J}_\rho$	$10^2 \cdot \text{diag}[1,1,2]^{\text{T}}$	m^4
Linear stiffness	$\boldsymbol{C}_T$	$10^9 \cdot \text{diag}[1,1,1]^{\text{T}}$	Nm^2
Rotational stiffness	$\boldsymbol{C}_R$	$10^{11} \cdot \text{diag}[1,1,1]^{\text{T}}$	Nm^2
Linear damping	$\boldsymbol{D}_T$	$1.5 \cdot \text{diag}[1,1,1]^{\text{T}}$	N/m
Rotational damping	$\boldsymbol{D}_R$	$1.5 \cdot \text{diag}[1,1,1]^{\text{T}}$	Nm/rad
Position references			
Equilibrium position	$\boldsymbol{\eta}_0$	$[729.96, 0, -800.38, 0, 0.13, 0]^{\text{T}}$	m
Reference position	$\boldsymbol{\eta}_{ref}$	$[780, 0, -800, 0, 0, 0]^{\text{T}}$	m

Chapter 7

PDE Pipe Model Validation Against RIFLEX

The difference between *validation* and *verification* is usually not well known, and the terms are frequently used interchangeably or together refereeing to the process of checking that a product, service, or system meets specifications, and that it fulfills its intended purpose. The terms are frequently linked to *quality management systems*, such as e.g. the ISO 9000, and to software development and computer modeling and simulation.

- *Verfication* refers to the process of evaluating whether or not a product, service or system complies with regulations, specifications, or conditions imposed at the start of a development phase.

- *Validation* refers to the process of establishing documented evidence that a product, service, or system accomplishes its intended requirement.

A frequently quoted rule–of–thumb is that validation is about building the right system, whereas verification is about building the system right.

Applying these terms to the PDE pipe model (6.30)–(6.31) developed in Chapter 6, verification should ensure that the right effects are included in the model, and that it is implemented correctly. Validation is to ensure that the model represent, and correctly reproduce the static and dynamic behaviors of the the simulated system including its boundary conditions, which is an offshore pipeline and the pipelay vessel.

A model validation of (6.30)–(6.31) is performed in this chapter to evaluate how accurate the model approximates the simulated system. Since a physical system is not available, the model is validated against other models, that in turn are validated against real systems. For static validation, the *natural catenary equation*, from Chapter 4, is applied. For static and dynamic validation, the FEM code RIFLEX is applied. The model is validated for a representative, but limit set of scenarios, which are considered as the validation tests.

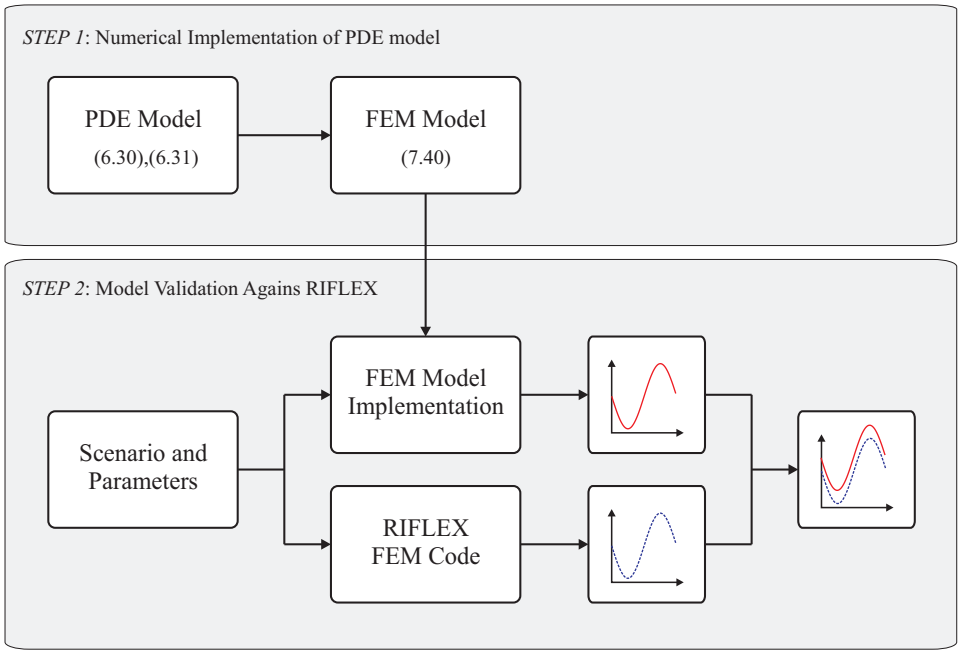

Figure 7.1: A breakdown of the contents of this chapter.

The pipe model (6.30)–(6.31) is a continuous operator problem, that must be converted into a discrete problem to approximate the solution. The model validation is performed in two main steps, as illustrated in Figure 7.1. These are

1. *FEM model implementation* – A FEM model suitable for simulation is derived from the PDE (6.30)–(6.31) by application of a numerical finite element method. (Section 7.1.)

2. *Numerical simulation* – A set simulation scenarios are defined for a chosen pipeline, including corresponding material properties and pipelay parameters. The pipeline scenarios are simulated using the FEM model, the natural catenary equation, and RIFLEX. The obtained simulation results are then compared. (Section 7.2.)

7.1 FEM Implementation

Galerkin methods are a class of methods in numerical analysis for converting a continuous operator problem into a discrete problem. The finite element method is such a method, where the solution approach is based on rendering the PDE into an approximating system of ordinary differential equations, which are then numerically integrated. The method is performed in two steps:

1. Turn the PDE formulation, called the *strong formulation*, into its equivalent

variational form, or *weak formulation*, and parametrize the rotation matrix $\boldsymbol{R}_t^e$ in Euler angles.

2. Semi–discretize the weak formulation in the curve parameter S, into a finite dimensional space to obtain a large set of ordinary differential equations (ODE) which approximates the original boundary value problem.

In this section, a finite element method is applied on (6.30)–(6.31) for the numerical simulations, following the same procedure as in Simo and Vu–Quoc (1988).

7.1.1 Galerkin Weak Formulation

In general, *weak formulations* are an important tool for the analysis of mathematical equations that permit the transfer of concepts of linear algebra to solve problems in other fields such as the PDE for the pipe. When the equation is given in a weak formulation, it has weak solutions with respect to certain admissible *test functions*. A Galerkin weak form of the initial boundary problem (6.30)–(6.31) with boundary conditions (6.38) and (6.47), is developed by taking the inner product with admissible test functions $\boldsymbol{u}, \boldsymbol{\vartheta}$. Let the space of test functions $\mathcal{V}$ be defined as

$$\mathcal{V} = \{(\boldsymbol{u}, \boldsymbol{\vartheta}) \,|\, S \in [0, L] \to \mathbb{R}^3 \times \mathbb{R}^3 \,|\, (\boldsymbol{u}, \boldsymbol{\vartheta})\big|_{S=0} = (\mathbf{0}, \mathbf{0})\}. \tag{7.1}$$

Admissible variations associated with any pipe configuration $(\boldsymbol{\varphi}, \boldsymbol{R}_t^e) \in \mathcal{C}$ span the tangent space $T_{(\boldsymbol{\varphi}, \boldsymbol{R}_t^e)}\mathcal{C}$ given by

$$T_{(\boldsymbol{\varphi}, \boldsymbol{R}_t^e)}\mathcal{C} \triangleq \{(\boldsymbol{u}, \boldsymbol{S}(\boldsymbol{\vartheta})\boldsymbol{R}_t^e) \,|\, (\boldsymbol{u}, \boldsymbol{\vartheta}) \in \mathcal{V}\}. \tag{7.2}$$

The obtain the weak formulation, the equations are multiplied by the test functions $\boldsymbol{u}$, $\boldsymbol{\vartheta}$ for the linear and rotational parts respectively, and integrated over S

$$\begin{aligned} &\int_0^L m_P \left\langle \ddot{\boldsymbol{\varphi}}, \boldsymbol{u} \right\rangle + \left\langle \left[\boldsymbol{I}_\rho \dot{\mathbf{w}}^e + \mathbf{w}^e \times (\boldsymbol{I}_\rho \mathbf{w}^e) \right], \boldsymbol{\vartheta} \right\rangle \, dS \\ &- \int_0^L \left\langle \partial_S \boldsymbol{n}^e, \boldsymbol{u} \right\rangle + \left\langle \partial_S \boldsymbol{m}^e, \boldsymbol{\vartheta} \right\rangle \, dS - \int_0^L \left\langle (\partial_S \boldsymbol{\varphi}) \times \boldsymbol{n}^e, \boldsymbol{\vartheta} \right\rangle \, dS \qquad (7.3) \\ &- \int_0^L \left\langle \widetilde{\boldsymbol{n}}^e, \boldsymbol{u} \right\rangle + \left\langle \widetilde{\boldsymbol{m}}^e, \boldsymbol{\vartheta} \right\rangle \, dS = 0 \qquad (7.4) \end{aligned}$$

which can be reformulated using integration by parts to

$$\begin{aligned}
&\int_0^L m_P \left\langle \ddot{\boldsymbol{\varphi}}, \boldsymbol{u} \right\rangle + \left\langle \left[\boldsymbol{I}_\rho \dot{\mathbf{w}}^e + \mathbf{w}^e \times (\boldsymbol{I}_\rho \mathbf{w}^e) \right], \boldsymbol{\vartheta} \right\rangle \, dS \\
&+ \int_0^L \left\langle \boldsymbol{n}^e, \partial_S \boldsymbol{u} \right\rangle + \left\langle \boldsymbol{m}^e, \partial_S \boldsymbol{\vartheta} \right\rangle \, dS - \int_0^L \left\langle \widetilde{\boldsymbol{n}}^e, \boldsymbol{u} \right\rangle + \left\langle \widetilde{\boldsymbol{m}}^e, \boldsymbol{\vartheta} \right\rangle \, dS \\
&+ \int_0^L \left\langle (\partial_S \boldsymbol{\varphi}) \times \boldsymbol{\vartheta}, \boldsymbol{n}^e \right\rangle \, dS - \left[\left\langle \boldsymbol{n}^e, \boldsymbol{u} \right\rangle + \left\langle \boldsymbol{m}^e, \boldsymbol{\vartheta} \right\rangle \right]_0^L = 0
\end{aligned} \tag{7.5}$$

where the triple product

$$\left\langle (\partial_S \boldsymbol{\varphi}) \times \boldsymbol{n}^e, \boldsymbol{\vartheta} \right\rangle = - \left\langle (\partial_S \boldsymbol{\varphi}) \times \boldsymbol{\vartheta}, \boldsymbol{n}^e \right\rangle, \tag{7.6}$$

has been applied. The pipe is fixed tangential to the flat seabed, such that the boundary conditions for $S = 0$ is

$$\left\langle \boldsymbol{n}^e, \boldsymbol{u} \right\rangle \big|_{S=0} = \left\langle \boldsymbol{m}^e, \boldsymbol{\vartheta} \right\rangle \big|_{S=0} = 0, \tag{7.7}$$

which for the expression of the boundary conditions in (7.5) yields

$$\left[\left\langle \boldsymbol{n}^e, \boldsymbol{u} \right\rangle + \left\langle \boldsymbol{m}^e, \boldsymbol{\vartheta} \right\rangle \right]_0^L = \left\langle \boldsymbol{n}^e, \boldsymbol{u} \right\rangle \big|_{S=L} + \left\langle \boldsymbol{m}^e, \boldsymbol{\vartheta} \right\rangle \big|_{S=L}. \tag{7.8}$$

Hence, the weak formulation can be expressed by a static (G_{stat}), and a dynamical part, (G_{dyn}). Applying (6.28) and (6.29) for $\widetilde{\boldsymbol{n}}^e$ and $\widetilde{\boldsymbol{m}}^e$, and the upper boundary condition (3.65) transformed according to (6.47), it can be written out,

$$\begin{aligned}
G_{\text{dyn}}(\boldsymbol{\varphi}, \boldsymbol{R}_t^e; \boldsymbol{u}, \boldsymbol{\vartheta}) \triangleq &\int_0^L \left\langle m_P \ddot{\boldsymbol{\varphi}}, \boldsymbol{u} \right\rangle + \left\langle \left[\boldsymbol{I}_\rho \dot{\mathbf{w}}^e + \mathbf{w}^e \times (\boldsymbol{I}_\rho \mathbf{w}^e) \right], \boldsymbol{\vartheta} \right\rangle \, dS + \\
&\int_0^L \left\langle \boldsymbol{f}_D^e, \boldsymbol{u} \right\rangle + \left\langle \boldsymbol{D}_R \mathbf{w}^e, \boldsymbol{\vartheta} \right\rangle dS + G_{\text{stat}}(\boldsymbol{\varphi}, \boldsymbol{R}_t^e; \boldsymbol{u}, \boldsymbol{\vartheta}) + \\
&\left\langle \left[\boldsymbol{M} \dot{\boldsymbol{\nu}} + \boldsymbol{C}(\boldsymbol{\nu}) \boldsymbol{\nu} + \boldsymbol{D}(\boldsymbol{\nu}) \boldsymbol{\nu} \right], (\boldsymbol{u}^{\mathrm{T}}, \boldsymbol{\vartheta}^{\mathrm{T}})^{\mathrm{T}} \right\rangle \Big|_{S=L} = 0,
\end{aligned} \tag{7.9}$$

for all test functions $(\boldsymbol{u}, \boldsymbol{\vartheta}) \in \mathcal{V}$, where the static part G_{stat} is given by

$$\begin{aligned}
G_{\text{stat}}(\boldsymbol{\varphi}, \boldsymbol{R}_t^e; \boldsymbol{u}, \boldsymbol{\vartheta}) \triangleq &\int_0^L \left\langle \boldsymbol{n}^e, \left[\partial_S \boldsymbol{u} + \boldsymbol{S}(\partial_S \boldsymbol{\varphi}) \boldsymbol{\vartheta} \right] \right\rangle + \left\langle \boldsymbol{m}^e, \partial_S \boldsymbol{\vartheta} \right\rangle dS + \\
&\int_0^L \left\langle \left[\boldsymbol{f}_g^e + \boldsymbol{\sigma}^e \right], \boldsymbol{u} \right\rangle dS + \left\langle \boldsymbol{g}(\boldsymbol{\varphi}, \boldsymbol{R}_b^e), (\boldsymbol{u}^{\mathrm{T}}, \boldsymbol{\vartheta}^{\mathrm{T}})^{\mathrm{T}} \right\rangle \Big|_{S=L}.
\end{aligned} \tag{7.10}$$

7.1.2 Rotation Matrix Parametrization

The next step is to introduce the Euler angles parametrization for rotation into the formulation. Let the rotation matrix $\boldsymbol{R}_t^e$ be parameterized in Euler angles $\boldsymbol{\Theta} = (\phi, \theta, \psi)^{\mathrm{T}} \rightarrow \boldsymbol{R}_t^e(\boldsymbol{\Theta})$ by the zxy–convention, which is locally diffeomorphic to $SO(3)$. Hence, $\boldsymbol{R}_t^e$ is given by

$$\boldsymbol{R}_t^e(\boldsymbol{\Theta}) = \boldsymbol{R}_{\boldsymbol{e}_2}(\theta)\boldsymbol{R}_{\boldsymbol{e}_1}(\phi)\boldsymbol{R}_{\boldsymbol{e}_3}(\psi), \tag{7.11}$$

where the elementary rotations about the $\boldsymbol{e}_1$, $\boldsymbol{e}_2$ and $\boldsymbol{e}_3$ axes are given by (A.6). Adopting the zxy–convention instead of the more common xyz–convention (A.7), moves the singularity inherent to Euler angles from pitch to roll, which is more suitable for the presented model.

This choice of parametrization yields the transformations

$$\mathbf{w}^e = \boldsymbol{\Pi}_e \dot{\boldsymbol{\Theta}}, \tag{7.12}$$

$$\dot{\mathbf{w}}^e = \boldsymbol{\Pi}_e \ddot{\boldsymbol{\Theta}} + \dot{\boldsymbol{\Pi}}_e \dot{\boldsymbol{\Theta}}, \tag{7.13}$$

$$\partial_S \boldsymbol{\omega}^e = \boldsymbol{\Pi}_e (\partial_S \boldsymbol{\Theta}), \tag{7.14}$$

where

$$\boldsymbol{\Pi}_e = \begin{bmatrix} \mathrm{c}\,\theta & 0 & \mathrm{c}\,\phi\,\mathrm{s}\,\theta \\ 0 & 1 & -\mathrm{s}\,\phi \\ -\mathrm{s}\,\theta & 0 & \mathrm{c}\,\phi\,\mathrm{c}\,\theta \end{bmatrix}. \tag{7.15}$$

Following the parametrization in Euler angles, the configuration space $\mathcal{C}$, defined in (6.3), can be reformulated as

$$\widetilde{\mathcal{C}} \triangleq \{(\boldsymbol{\varphi}, \boldsymbol{\Theta}) \,|\, S \in [0, L] \rightarrow \mathbb{R}^3 \times \mathbb{R}^3 \,|\, \langle \partial_S \boldsymbol{\varphi}(S), \boldsymbol{R}_t^e(\boldsymbol{\Theta}) \boldsymbol{e}_1 > 0\}, \tag{7.16}$$

with test functions

$$\widetilde{\mathcal{V}} \triangleq \{(\boldsymbol{u}, \widetilde{\boldsymbol{\vartheta}}) \,|\, S \in [0, L] \rightarrow \mathbb{R}^3 \times \mathbb{R}^3 \,|\, (\boldsymbol{u}, \widetilde{\boldsymbol{\vartheta}})\big|_{S=0} = (\mathbf{0}, \mathbf{0})\}, \tag{7.17}$$

and the new tangent space becomes

$$T_{(\boldsymbol{\varphi}, \boldsymbol{\Theta})} \widetilde{\mathcal{C}} \triangleq \{(\boldsymbol{u}, \widetilde{\boldsymbol{\vartheta}}) \,|\, (\boldsymbol{u}, \widetilde{\boldsymbol{\vartheta}}) \in \widetilde{\mathcal{V}}\}. \tag{7.18}$$

Hence, (7.9) and (7.10) becomes

$$
\begin{aligned}
G_{\mathrm{dyn}}(\boldsymbol{\varphi},\boldsymbol{\Theta};\boldsymbol{u},\boldsymbol{\vartheta}) \triangleq & \int_0^L m_P \left\langle \ddot{\boldsymbol{\varphi}},\boldsymbol{u}\right\rangle \, dS \\
& + \int_0^L \left\langle \left[\boldsymbol{R}_t^e \boldsymbol{J}_\rho^t \left(\boldsymbol{R}_t^e\right)^{\mathrm{T}} \left(\boldsymbol{\Pi}_e \ddot{\boldsymbol{\Theta}} + \dot{\boldsymbol{\Pi}}_e \dot{\boldsymbol{\Theta}}\right)\right], \boldsymbol{\vartheta}\right\rangle \, dS \\
& + \int_0^L \left\langle \left(\boldsymbol{\Pi}_e \dot{\boldsymbol{\Theta}}\right) \times \left(\boldsymbol{R}_t^e \boldsymbol{J}_\rho^t \left(\boldsymbol{R}_t^e\right)^{\mathrm{T}} \boldsymbol{\Pi}_e \dot{\boldsymbol{\Theta}}\right), \boldsymbol{\vartheta}\right\rangle \, dS \\
& + \int_0^L \left\langle \boldsymbol{f}_D^e, \boldsymbol{u}\right\rangle + \left\langle \boldsymbol{D}_R \boldsymbol{\Pi}_e \dot{\boldsymbol{\Theta}}, \boldsymbol{\vartheta}\right\rangle dS + G_{\mathrm{stat}}(\boldsymbol{\varphi},\boldsymbol{\Theta};\boldsymbol{u},\boldsymbol{\vartheta}) \\
& + \left\langle \left[\boldsymbol{M}\dot{\boldsymbol{\nu}} + \boldsymbol{C}(\boldsymbol{\nu})\boldsymbol{\nu} + \boldsymbol{D}(\boldsymbol{\nu})\boldsymbol{\nu}\right], \left(\boldsymbol{u}^{\mathrm{T}}, \boldsymbol{\vartheta}^{\mathrm{T}}\right)^{\mathrm{T}} \right\rangle \Bigg|_{S=L} = 0, \qquad (7.19)
\end{aligned}
$$

$$
\begin{aligned}
G_{\mathrm{stat}}(\boldsymbol{\varphi},\boldsymbol{\Theta};\boldsymbol{u},\boldsymbol{\vartheta}) \triangleq & \int_0^L \left\langle \boldsymbol{n}^e, \left[\partial_S \boldsymbol{u} + \boldsymbol{S}(\partial_S \boldsymbol{\varphi})\boldsymbol{\vartheta}\right] \right\rangle + \left\langle \boldsymbol{m}^e, \partial_S \boldsymbol{\vartheta} \right\rangle dS \\
& + \int_0^L \left\langle \left[\boldsymbol{f}_g^e + \boldsymbol{\sigma}^e\right], \boldsymbol{u}\right\rangle dS + \left\langle \boldsymbol{g}(\boldsymbol{\varphi},\boldsymbol{\Theta}), \left(\boldsymbol{u}^{\mathrm{T}}, \boldsymbol{\vartheta}^{\mathrm{T}}\right)^{\mathrm{T}} \right\rangle \Bigg|_{S=L}. \qquad (7.20)
\end{aligned}
$$

which is the weak formulation of the pipe written out, where (6.27) has been applied to the state dependent inertia tensor $\boldsymbol{I}_\rho^e(S,t)$.

7.1.3 Discretization

The basic idea of discretization is to replace the infinite dimensional problem with a finite dimensional version. Any continuous function $f(S,t)$ can be approximated with n nodes by

$$
f_h = \sum_{i=1}^{n} N_i(S) \; f_i(t) \approx f(S,t), \qquad (7.21)
$$

where N_i is the basis function. Let the weak formulation (7.19) for the configuration space (7.16) be semi discretized in N nodes with uniform sub intervals $\bigcup_{i=1}^{N-1}[S_i, S_{i+1}] = [0, L]$, with interval length h, where N_i is the piecewise linear shape function

$$
N_i(S) = \begin{cases} \dfrac{S - S_{i-1}}{h} & , \; S \in [S_{i-1}, S_i] = I_{i-1} \\ \dfrac{S_{i+1} - S}{h} & , \; S \in [S_i, S_{i+1}] = I_i \\ 0 & , \text{ otherwise,} \end{cases} \qquad (7.22)
$$

$$\partial_S N_i(S) = \begin{cases} \dfrac{1}{h} & , S \in I_{i-1} \\ -\dfrac{1}{h} & , S \in I_i \\ 0 & , \text{otherwise,} \end{cases} \tag{7.23}$$

which is frequently known as hat or *tent* functions, see Figure 7.2. Hence the displacement state vectors and weighting functions are interpolated in the spatial variable S as

$$\boldsymbol{\varphi} \approx \boldsymbol{\varphi}_h = \sum_{i=1}^{N} \boldsymbol{\varphi}_i(t) N_h^i(S), \tag{7.24}$$

$$\boldsymbol{\Theta} \approx \boldsymbol{\Theta}_h = \sum_{i=1}^{N} \boldsymbol{\Theta}_i(t) N_h^i(S), \tag{7.25}$$

$$\boldsymbol{u} \approx \boldsymbol{u}_h = \sum_{i=1}^{N} \boldsymbol{u}_i N_h^i(S), \tag{7.26}$$

$$\widetilde{\boldsymbol{\vartheta}} \approx \widetilde{\boldsymbol{\vartheta}}_h = \sum_{i=1}^{N} \widetilde{\boldsymbol{\vartheta}}_i N_h^i(S). \tag{7.27}$$

Hence, the Galerkin equivalent for $(n-1)$ nodes, since the pipe is fixed at the seabed, where $i = 2, \cdots, n$ is

$$\begin{aligned}
&\int_0^L \begin{bmatrix} m_P N_i(S) N_j(S) I_{3\times 3} & 0 \\ 0 & N_i(S) N_j(S) I_\rho^e \boldsymbol{\Pi}_e \end{bmatrix} dS \begin{bmatrix} \ddot{\boldsymbol{\varphi}}_j \\ \ddot{\boldsymbol{\Theta}}_j \end{bmatrix} = \\
&- \int_0^L \begin{bmatrix} \left(\partial_S N_i(S)\right) I_{3\times 3} & 0 \\ -N_i(S)\, \boldsymbol{S}\left(\partial_S \boldsymbol{\varphi}\right) & \partial_S N_i(S)\, I_{3\times 3} \end{bmatrix} \begin{bmatrix} \boldsymbol{n}^e \\ \boldsymbol{m}^e \end{bmatrix} dS \\
&- \int_0^L \begin{bmatrix} 0 \\ N_i(S)\, I_\rho^e \dot{\boldsymbol{\Pi}}_e \dot{\boldsymbol{\Theta}} \end{bmatrix} dS - \int_0^L \begin{bmatrix} 0 \\ N_i(S)\, \boldsymbol{S}\left(\boldsymbol{\Pi}_e \dot{\boldsymbol{\Theta}}\right)\left(I_\rho^e \boldsymbol{\Pi}_e \dot{\boldsymbol{\Theta}}\right) \end{bmatrix} dS \\
&- \int_0^L \begin{bmatrix} N_i(S)\, \boldsymbol{f}_g^e \\ 0 \end{bmatrix} dS - \int_0^L \begin{bmatrix} N_i(S)\, \boldsymbol{R}_t^e \boldsymbol{f}_d^t \\ N_i(S)\, \boldsymbol{D}_R \boldsymbol{\Pi}_e \dot{\boldsymbol{\Theta}} \end{bmatrix} dS \\
&- \int_0^L \begin{bmatrix} N_i(S)\, \boldsymbol{\sigma}^e \\ 0 \end{bmatrix} dS + \delta_{in} \begin{bmatrix} I_{3\times 3} & 0 \\ 0 & I_{3\times 3} \end{bmatrix} \begin{bmatrix} \tilde{\boldsymbol{n}}^e(S=L) \\ \tilde{\boldsymbol{m}}^e(S=L) \end{bmatrix}.
\end{aligned} \tag{7.28}$$

The number of equations becomes $6(n-1)$. Kronecker delta δ_{in} is applied to ensure that the upper boundary condition givens only apply to node n.

7.1.4 Gauss Quadrature

The integrals of (7.28) are approximated using two point Gaussian quadrature for each interval $[S_i, S_{i+1}] \subset [0, L]$, except for the stiffness integral which is ap-

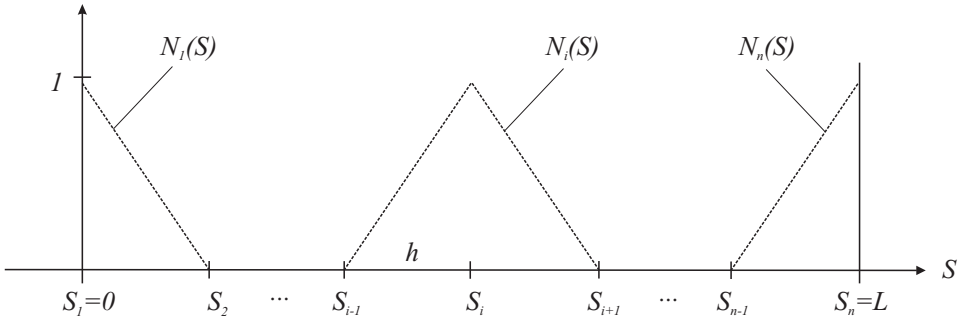

Figure 7.2: Test functions N_i.

proximated by a one point Gaussian quadrature to avoid shear locking (Simo and Vu–Quoc, 1986). The n–point Gaussian quadrature rule is stated on the domain $[-1, 1]$ as

$$\int_{-1}^{1} f(x)\, dx \approx \sum_{i-1}^{N} w_i f(x_i)\,. \tag{7.29}$$

For one point Gaussian quadrature $x_i = 0$ and $w_i = 2$, such that (7.29) becomes

$$\int_{-1}^{1} f(x)\, dx \approx 2\, f(0)\,, \tag{7.30}$$

while for two point Gaussian quadrature $x_i = \pm\sqrt{1/3}$ and $w_i = 1$, such that (7.29) becomes

$$\int_{-1}^{1} f(x)\, dx \approx f\left(-\sqrt{\frac{1}{3}}\right) + f\left(\sqrt{\frac{1}{3}}\right). \tag{7.31}$$

Let the integration over a single interval $S \in I_j = [S_j, S_{j+1}]$ be

$$\int_{S_i}^{S_{i+1}} F(S)\, dS = \frac{h}{2} \int_{-1}^{1} \tilde{F}(x)\, dx, \tag{7.32}$$

where for convenience the change of variables $S_j \le S \le S_{j+1} \rightarrow -1 \le x \le 1$ is done using the mapping

$$S = S_j + \frac{h}{2}(1 + x)\,, \quad dS = \frac{h}{2} dx, \tag{7.33}$$

such that

$$\tilde{F}(x)\, dx = F\left(S_j + \frac{h}{2}(1 + x)\right), \tag{7.34}$$

and (7.22) is

$$\tilde{N}_i(x) = \begin{cases} \frac{1}{2}(1+x) & , S \in I_{i-1} \\ \frac{1}{2}(1-x) & , S \in I_i \\ 0 & , \text{otherwise,} \end{cases} \tag{7.35}$$

and (7.23) is

$$\partial_S \tilde{N}_i(x) = \begin{cases} \frac{1}{h} & , S \in I_{i-1} \\ -\frac{1}{h} & , S \in I_i \\ 0 & , \text{otherwise,} \end{cases} \tag{7.36}$$

The approximate solution for one interval by one point Gaussian quadrature is found by considering the integration over every interval. Consider a single interval $S \in I_j = [S_j, S_{j+1}]$, where all test functions $N_i = 0 \; \forall \; i, \; \backslash \; i = \{j, j+1\}$, such that for N_j and N_{j+1},

$$\begin{aligned} f_h &= \sum_{i=1}^{n} N_i(S) f_i(t) = N_j(S) f_j(t) + N_{j+1}(S) f_{j+1}(t) \\ &= \frac{S_{j+1} - S}{h} f_j(t) + \frac{S - S_j}{h} f_{j+1}(t), \end{aligned} \tag{7.37}$$

where (7.22) has been applied. Applying (7.35) and (7.36) yield

$$\begin{aligned} \tilde{f}_h(x) &= \frac{1}{2}(1-x) f_j(t) + \frac{1}{2}(1+x) f_j(t) \\ &= \frac{1}{2}\left[(1-x) f_j(t) + (1+x) f_{j+1}(t)\right], \end{aligned} \tag{7.38}$$

and

$$\begin{aligned} \partial_S \tilde{f}_h(x) = \partial_x \tilde{f}_h(x) \frac{\partial x}{\partial S} &= \frac{1}{2}\left[-f_j(t) + f_{j+1}(t)\right] \frac{2}{h} \\ &= \frac{1}{h}\left[f_{j+1}(t) - f_j(t)\right]. \end{aligned} \tag{7.39}$$

Note that due to the boundary condition at the seabed, the pipe is not allowed to move, and $N_1 = 0$ for I_1. The semi discretized problem is finally obtained on the form

$$\overline{\boldsymbol{M}}_h(\dot{\boldsymbol{x}}_j, \boldsymbol{x}_j)\ddot{\boldsymbol{x}}_i + \overline{\boldsymbol{C}}_h(\dot{\boldsymbol{x}}_j, \boldsymbol{x}_j)\dot{\boldsymbol{x}}_i + \overline{\boldsymbol{K}}_h(\boldsymbol{x}_j)\boldsymbol{x}_i = \boldsymbol{0}, \qquad \text{for} \quad i, j = 1, \ldots, N, \tag{7.40}$$

where

$$\boldsymbol{x}_i = \left[\boldsymbol{\varphi}_i, \boldsymbol{\Theta}_i\right]^{\mathrm{T}}. \tag{7.41}$$

is the state vector, and $\overline{\boldsymbol{M}}_h$, $\overline{\boldsymbol{C}}_h$ and $\overline{\boldsymbol{K}}_h$ are the semi discretized system mass, damping and stiffness matrices, respectively. This form is well known in marine control engineering. In the simulations Matlab is applied, and the embedded ODE–solver `ode23tb` is used to solve the semi discretized problem (7.40).

Table 7.1: Applied physical constants and parameters.

Parameter	*Notation*	*Value*	*Unit*
Constants			
Density of steel	ρ_s	$7.850 \cdot 10^6$	kg/m^3
Density of water	ρ_w	$1.025 \cdot 10^3$	kg/m^3
Earth gravity	g	9.80665	m/s^2
Young's modulus steel	E	$206 \cdot 10^9$	N/m^2
Shear modulus steel	G	$7.9231 \cdot 10^{10}$	N/m^2
Pipe properties			
Outer pipe diameter	d_o	0.762	m
Wall thickness	WT	0.033	m
Undeformed pipe length	L	1500	m
Unit mass of empty pipe	m_p	593.2818	kg
Submerged unit weight	w_s	$1.2341 \cdot 10^3$	N/m
Moments of inertia	I_1	78.9851	$kg \cdot m^2$
	$I_2 = I_3$	39.4925	$kg \cdot m^2$
Unit polar moments of inertia	I	$5.0309 \cdot 10^{-3}$	m^4
	J	$1.0062 \cdot 10^{-2}$	m^4
Axial stiffness	EA	$1.5569 \cdot 10^{10}$	Nm^2
Shear stiffness	GA	$9.0330 \cdot 10^9$	Nm^2
Torsional stiffness	GJ	$7.9720 \cdot 10^8$	Nm^2
Bending stiffness	EI	$1.0364 \cdot 10^9$	Nm^2

7.2 FEM Model Validation Against RIFLEX

7.2.1 Scenario and Parameters

For the analysis, we will consider the installation of a 30 inch ($0.762m$) OD (outer diameter) steel pipe, without weight coating, at a water depth of 900 meters using the J–lay method, see Figure 6.1. The seabed is assumed to be flat, there are no environmental disturbances, and the physical constants and material pipe properties applied in the analysis are listed in Table 7.1. This scenario and the parameters are chosen since they are realistic, and similar scenarios are analyzed for industrial applications.

The Static Case

The static analyses are performed in the vertical plane spanned by $\{\boldsymbol{e}_1, \boldsymbol{e}_3\}$. Three different values for the horizontal tension $H = \{200, 400, 800\}kN$ are applied to the

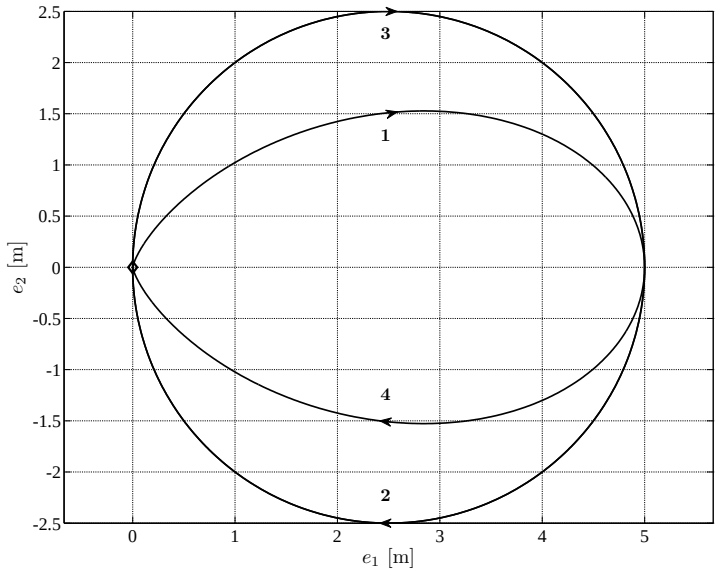

Figure 7.3: The path followed by the surface vessel. The vessel starts in $(0, 0)$, which represents the surface position for the static solution where $H = 400kN$. The path is made up of three complete circles with ramps to limit acceleration at the beginning and end. The sequence and direction is indicated by the arrows and numbers 1–4. After completing the third circle, the vessel remains fixed at $(0, 0)$.

top node at $\boldsymbol{\varphi}(L)$ in the $\boldsymbol{e}_1$–direction. The case is studied for $EI = 0$ and $EI \neq 0$ to see how bending stiffness influences the geometric configuration. The hang–off angle β and the lay–back distance l_h, the horizontal distance from hang–off to touchdown, and the pipe curvature are compared for validation.

The Dynamic Case

The static solution for $H = 400\,kN$ is assumed as the initial condition for the dynamic analysis. No lateral or axial seabed friction is assumed. The pipe at $S = 0$ is horizontally clamped to the seabed, and at $S = L$, it is attached to the center of gravity of the vessel, where it is free to rotate. A linearized vessel model is used where the coefficient matrices are obtained from the *Marine Systems Simulator* (MSS) available at (Fossen and Perez, 2004). A DP system is implemented by the nonlinear PID–controller (6.77), to force the surface vessel to track a circular path with period $T = 10\,s$ and diameter $\delta = 5\,m$, three times, before returning to its initial position, see Figure 7.3. This imposes a spiraling motion on the pipe. The control reference is ramped to limit accelerations.

The same number of nodes, with equal spacing are defined for the RIFLEX simulation. In addition, added mass and seabed friction are removed, and the vertical equilibrium for the pipe resting at the seabed is set to $d_o/2$, which is

Table 7.2: Static analyses results for the pipe model without bending stiffness e.g. $EI = 0$ and the catenary.

Horizontal tension	H	200	400	800	kN
Pipe model without bending stiffness, $EI = 0$					
Hang–off angle	β	81.22	74.64	65.24	deg
Lay–back distance	l_h	412.25	645.10	975.51	m
Catenary					
Hang–off angle	β	81.22	74.64	65.24	deg
Lay–back distance	l_h	415.25	649.41	982.24	m

slightly below the corresponding equilibrium for the FEM simulation; $d_o/8$. The position of the pipe tip over the course of 60 seconds of simulation with the FEM model is given as input to RIFLEX, as RIFLEX does not include the surface vessel dynamics.

7.2.2 Static Solutions

To approximate the static solution, $G_{\text{stat}}(\boldsymbol{\varphi}, \boldsymbol{\Theta}; \boldsymbol{u}, \boldsymbol{\vartheta}) = 0$, the Newton–Raphson strategy described in (Simo and Vu–Quoc, 1986) is applied. For the approximated static solution (7.20), let the averaged error estimate be given by

$$\varepsilon^N \triangleq \frac{1}{N} \sum_{i=1}^{N} \|(\boldsymbol{\varphi}_i, \boldsymbol{\Theta}_i) - (\boldsymbol{\varphi}^{\text{ref}}(S_i), \boldsymbol{\Theta}^{\text{ref}}(S_i))\|_2, \tag{7.42}$$

where the approximated solution from a fine gridded discretization is taken as a reference solution

$$(\boldsymbol{\varphi}^{\text{ref}}(S), \boldsymbol{\Theta}^{\text{ref}}(S)) \triangleq \sum_{i=1}^{N} (\boldsymbol{\varphi}_i, \boldsymbol{\Theta}_i) N_h^i(S). \tag{7.43}$$

The convergence of ε^N is shown in Figure 7.4.

For high accuracy, the pipe model is semi–discretized with $N = 740$, such that element length is approximately 2 meters. The following three cases are studied:

- **PDE vs. The natural catenary** – *(Figure 7.5)* – To validate the model against the catenary, the bending stiffness in the pipe model is set to zero, i.e., $EI = 0$, and the computed static configurations are plotted. The FEM pipe model configurations and the catenary configurations, obtained from (4.4), can hardly be distinguished. The hang–off angle β and the lay–back distance l_h for the PDE and the catenary are presented in Table 7.2, and are seen to correspond well. With an accuracy of two decimals, the hang–off angles obtained by the two models can not be distinguished from each other. The difference in lay–back distance computed by the PDE model differs with

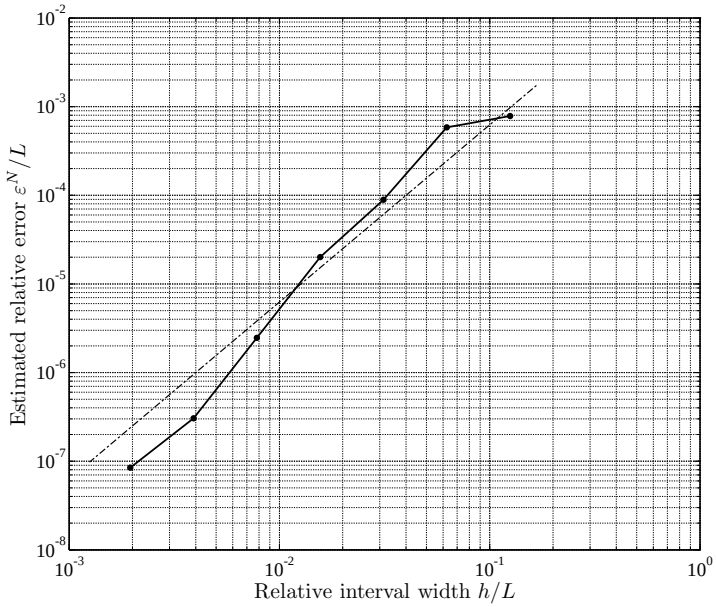

Figure 7.4: The estimated relative error ε^N/L for the static solution approximations where the number of elements $N-1 = 8, 16, 32, 64, 128, 256, 512$, against relative interval width $h/L = 1/(N-1)$, where an approximated solution with $N-1 = 1024$ is taken as the reference. The results compare well to the quadratic auxiliary line.

Table 7.3: Static analyses results for the pipe model including the effects of bending stiffness and RIFLEX.

Horizontal tension	H	200	400	800	kN
Pipe model					
Hang–off angle	β	80.97	74.30	64.87	deg
Lay–back distance	l_h	467.92	679.76	996.29	m
RIFLEX					
Hang–off angle	β	81.0	74.4	65.0	deg
Lay–back distance	l_h	477	686	1001	m

less than 0.7% from the results obtained by the catenary equation. This may be explained from the effect of the seabed interaction of the pipe model. However, this error is so small that it might as well we due to the numerical solution.

- **Bending stiffness vs. no bending stiffness** – *(Figure 7.6)* – The FEM model with $EI \neq 0$, and without bending stiffness $EI = 0$ are plotted. The effect of the bending stiffness is most significant in the touchdown area and for the hang–off angle. The effect of the bending stiffness is seen to become less when the axial tension increases.

- **PDE vs. RIFLEX** – *(Figures 7.7 and 7.8)* – The computed static configurations including bending stiffness for $H = \{200, 400, 800\}\, kN$ for the PDE and RIFLEX are plotted in Figure 7.7. The hang–off angles and lay–back distances are presented in Table 7.2, and corresponds well. The largest difference is found in the l_h, which for $H = 200\, kN$ is approximately 1.9%. As the tension increases, this difference decreases, $H = 400\, kN$ yields a relative error of 0.9%, and $H = 800\, kN$ yields a relative error of 0.5% The curvature along the pipe configurations of Figure 7.7 are plotted in Figure 7.8, and show that the forces also correspond well in the two models.

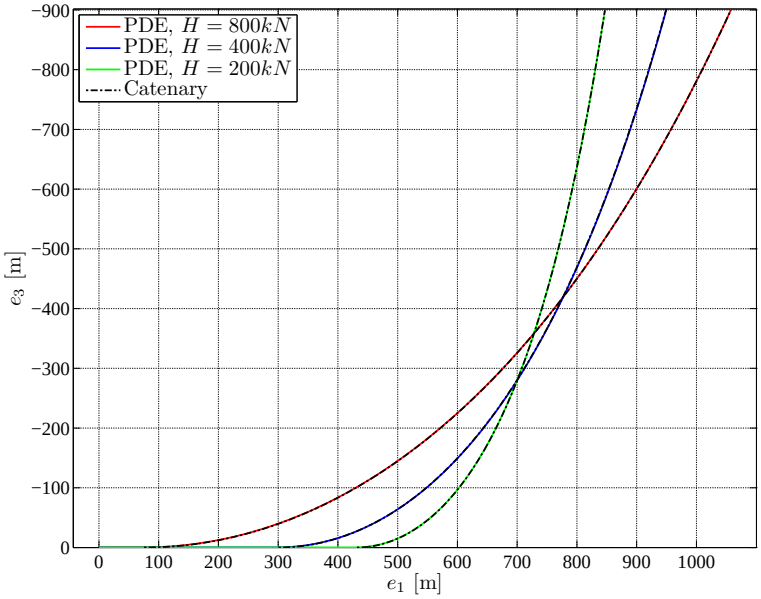

Figure 7.5: Static pipe configuration without bending stiffness of the pipe model validated against the catenary.

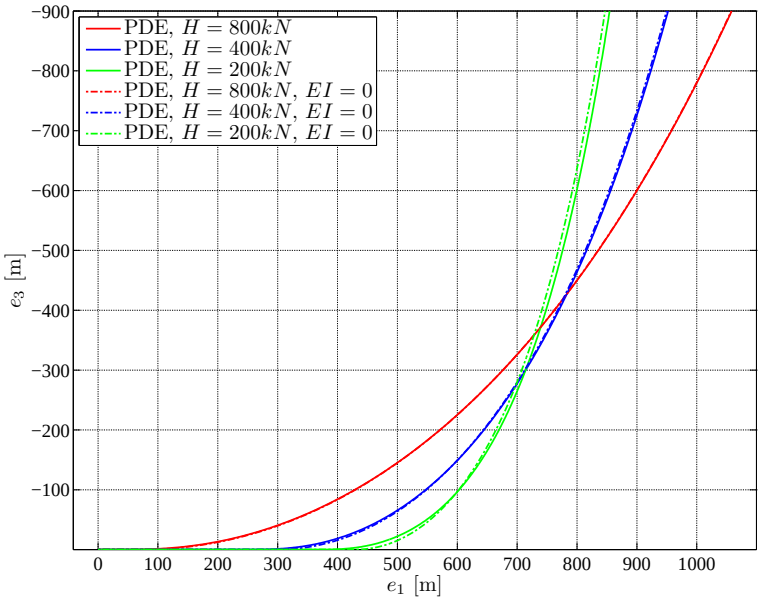

Figure 7.6: Pipe model configurations with and without bending stiffness compared.

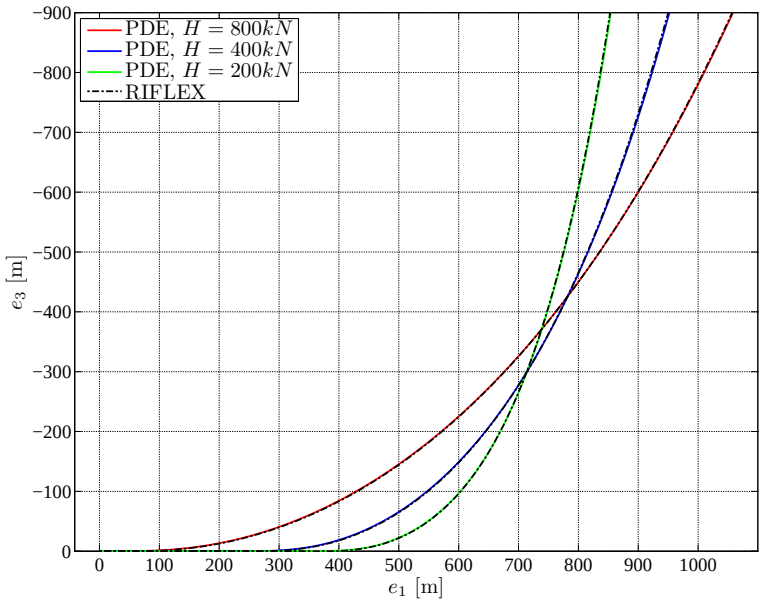

Figure 7.7: Static pipe configuration of the pipe model validated against RIFLEX.

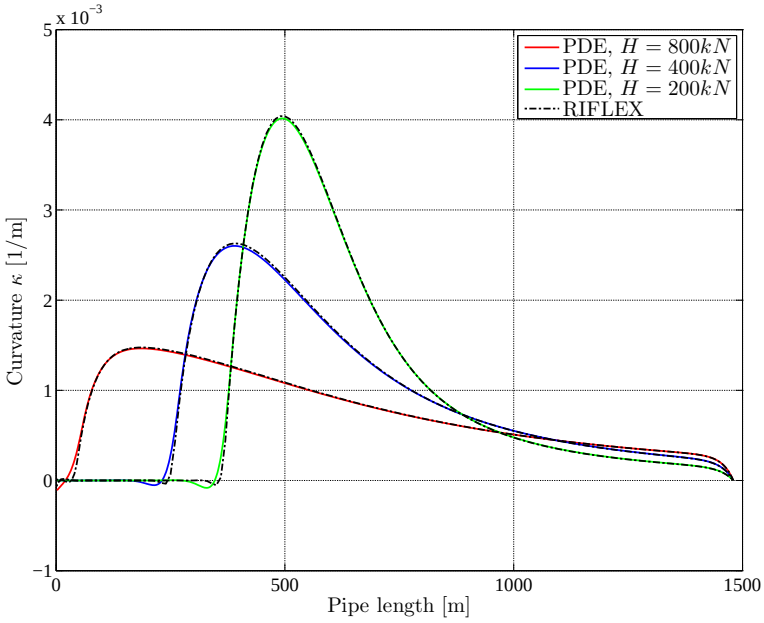

Figure 7.8: Comparing the curvature κ of the pipe model and RIFLEX.

7.2.3 Dynamic Simulation

In the dynamic analysis, the static configuration for $H = 400\,kN$ and $N = 100$ with elements of equal lengths is taken as the initial configuration. The RIFLEX results are always denoted by the dashed black line. The plots of the simulation results are divided in three groups; *geometric plots*, *force and moment plots*, and *node plots*.

Geometric Plots

Plots related to the geometric shape of the configuration, and how it changes during the simulation.

- **Snapshots** – *(Figures 7.9 and 7.10)* – A snapshot of the pipe configurations is taken every 5 seconds over the course of the dynamic simulation. In Figure 7.9, the surface vessel follows the path described in Figure 7.3. The pipe moves in a helix, however the choice of axes makes this impossible to see. A wave propagates down the pipe and is reflected at the lower boundary. The lack of longitudinal friction at the seabed can be seen. At $t = 30\,s$, the vessel is fixed in its initial position, Figure 7.9. The hydrodynamic drag forces are seen to damp out pipe motion. The FEM and RIFLEX results are seen to follow closely.

- **Displacement envelopes** – *(Figure 7.11)* – The maximum relative displacement from the initial configuration over the course of the simulation.

- **Pipe length** – *(Figure 7.12)* – The pipe overall length is a sensitive parameter, since it integrates the elongation of all the nodes along S. Both the amplitude and frequency of the pipe elongation over the course of the simulation are seen to correspond well. Pipe extension along $\boldsymbol{t}_1$ is derived from the first component of the vector $\boldsymbol{\gamma}^t$ (6.17).

Force and Moment Plots

Plots for the forces and moments distributed in the pipe during the simulation.

- **Axial tension envelope** *(Figure 7.13)* – The maximum axial tension over the course of the simulation. The axial tension along the axis $\boldsymbol{t}_1$ is given as the first component of the material stress resultant $\boldsymbol{n}^t$ (6.20), denoted $\boldsymbol{n}_1^t$.

- **Shear force envelope** – *(Figure 7.14)* – The maximum shearing of the pipe along S during the simulation. The cross–section of the pipe is considered, and the shearing is taken in directions $\boldsymbol{t}_2$ and $\boldsymbol{t}_3$ of the material stress resultant $\boldsymbol{n}^t$ (6.20). The shearing is largest close to the touchdown point and at the point where the pipe is connected to the vessel.

- **Twisting force envelope** – *(Figure 7.15)* – The twisting about $\boldsymbol{t}_1$ is found in the stress couple $\boldsymbol{m}^t$ (6.21), as $\boldsymbol{m}_1^t$ in the PDE model.

- **Bending moment** – *(Figure 7.16)* – The maximum bending moment $\boldsymbol{m}_2^t$ and $\boldsymbol{m}_3^t$ along S. This is also given by the stress couple $\boldsymbol{m}^t$ (6.21), but along $\boldsymbol{t}_2$ and $\boldsymbol{t}_3$. The largest values are found close to the touchdown and the surface vessel.

Node Plots

The plots so far has been considering the entire pipe. Finally we will investigate the dynamic position and bending moment as a function of time at a few nodes along the discretized pipe. The norms of the displacement and bending moment vectors are plotted.

- **Near surface** – *(Figure 7.17)* – Node $N = 90$, close to the surface vessel. The forced motion of the surface vessel can be seen. The FEM and RIFLEX simulations compares very well.

- **Near touchdown** – *(Figure 7.18)* – Node $N = 25$, close to the touchdown. The motion is more chaotic here, and the forced motion from the surface vessel can not be recognized. However, also at this node the FEM and RIFLEX simulations compares very well.

This indicates a very good dynamic correlation of the results, as well as nominal values are in agreement.

7.3 Model Convergence

For a practical applications of the numerical implementation, the convergence must be considered. The number of nodes in a simulation should be small to optimize computation time, while at the same time capture the main dynamic behavior of the system. The dynamic simulation scenario, given in section 7.2.1, is repeated for different discretization of S, for $N = \{10, 20, 40, 80\}$ and plotted against $N = 100$, used in the dynamic validation, see Figures 7.19 and 7.20.

Visual investigation of the configurations, compared the reference configuration for $N = 100$, are:

- $N = 10$ – Large difference from the reference,
- $N = 20$ – The main dynamics are kept,
- $N = 40$ – Can only be distinguished at some locations,
- $N = 80$ – Can not be distinguished from the reference.

Where N is too small, the forced motion at the upper boundary is seen to propagate too fast along the elastic body. To improve the dynamics without increasing the number of nodes, variable element lengths can be introduced, such that sensitive regions along the pipe, i.e., the touchdown and the hang–off area, may have shorter elements than the less sensitive regions.

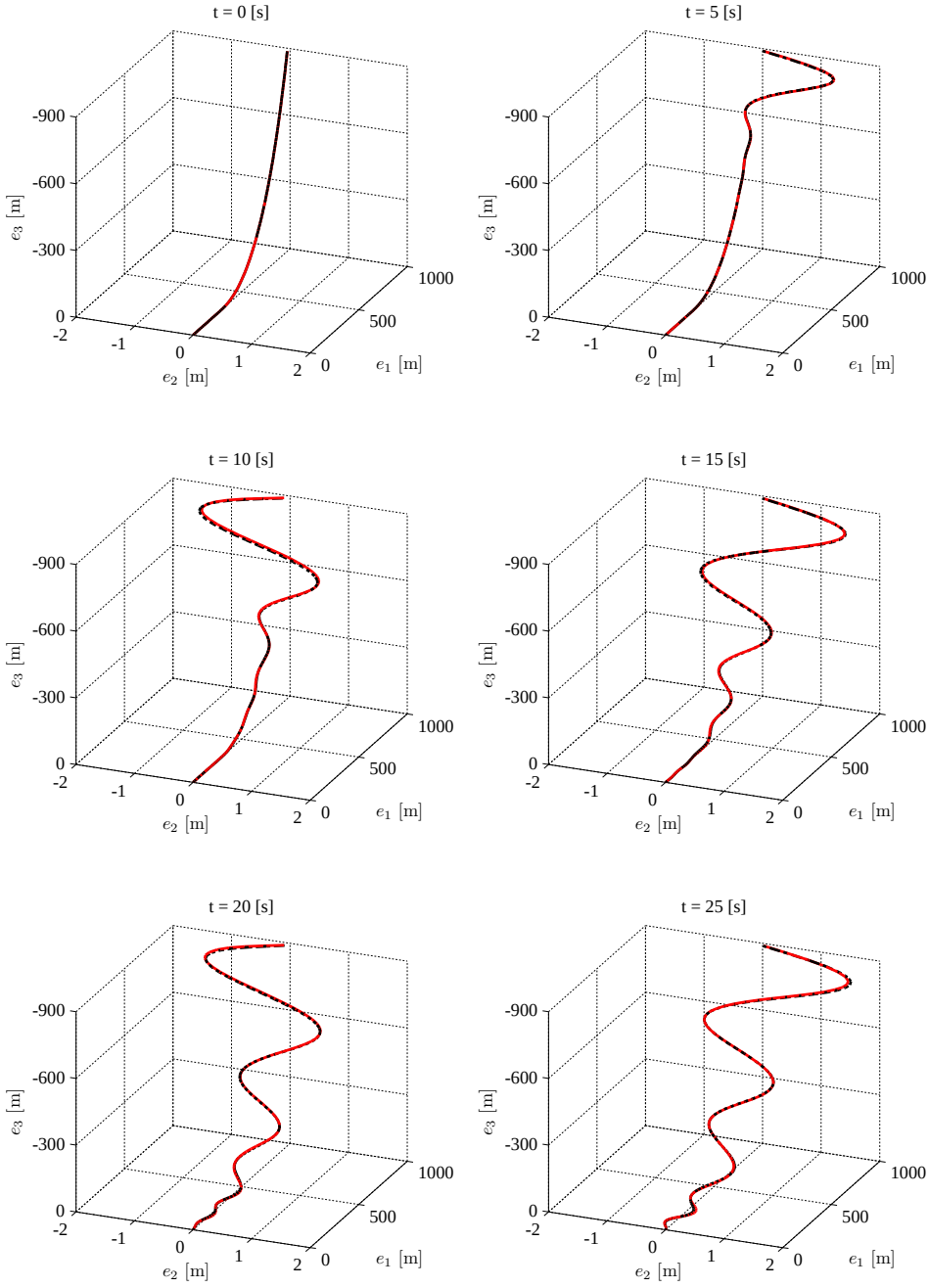

Figure 7.9: Snapshots of the dynamic simulation, $t = 0 - 25\,s$.

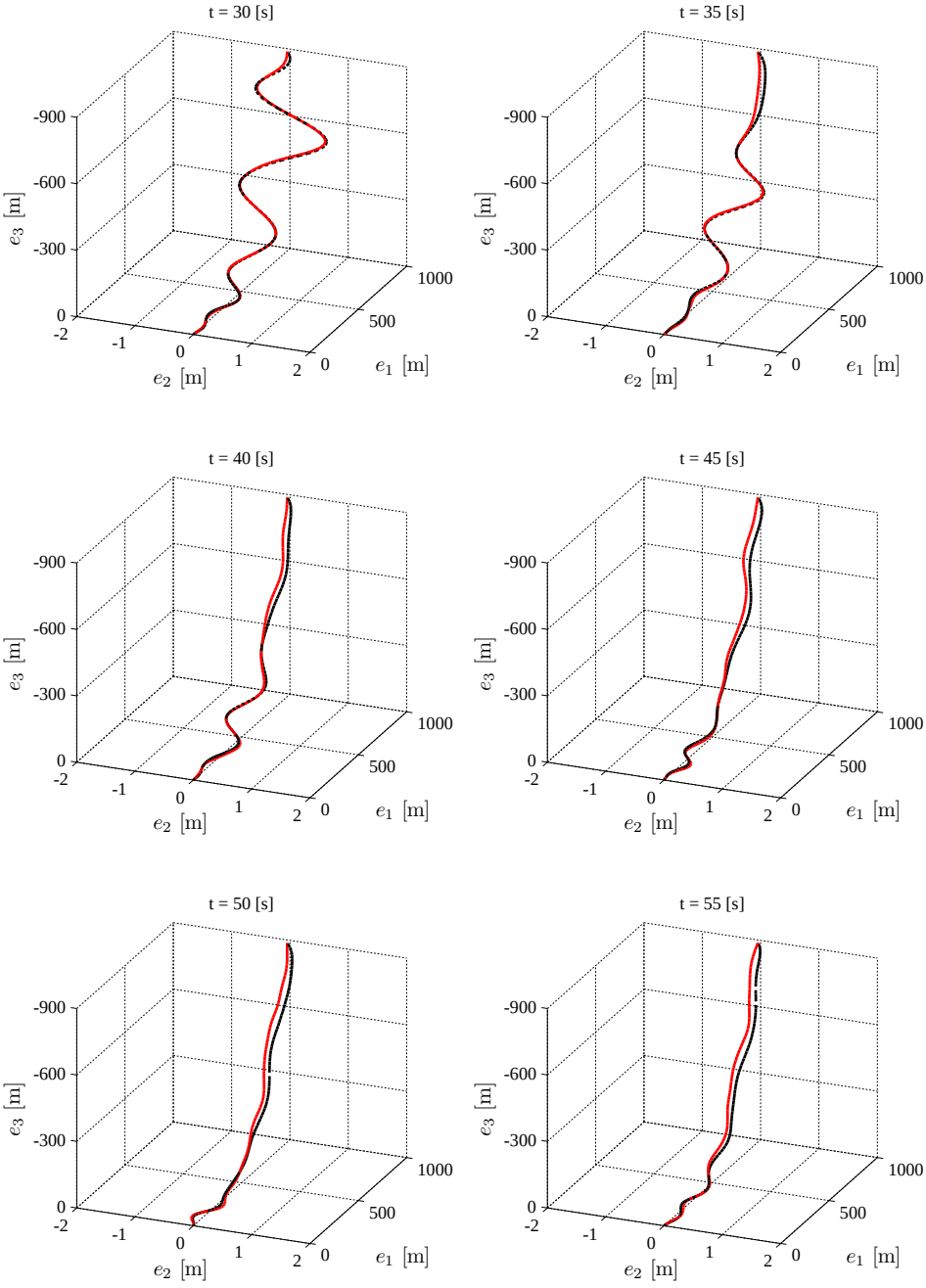

Figure 7.10: Snapshots of the dynamic simulation, $t = 30 - 55\,s$.

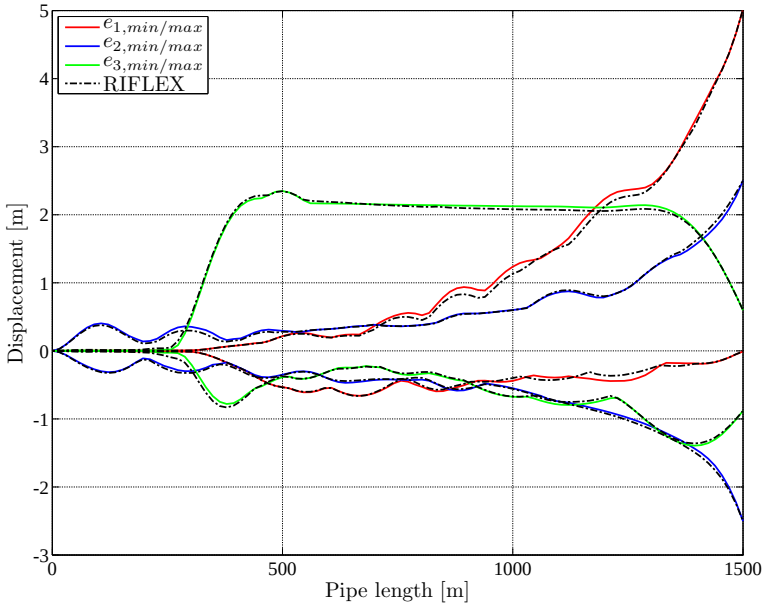

Figure 7.11: Relative displacement envelope in the $\boldsymbol{e}_1$, $\boldsymbol{e}_2$ and $\boldsymbol{e}_3$ directions for the proposed model compared to RIFLEX.

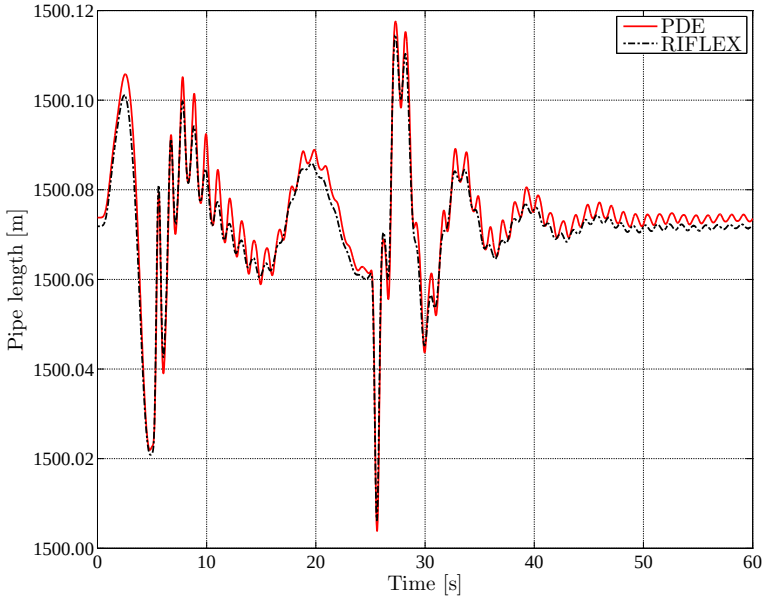

Figure 7.12: Pipe length.

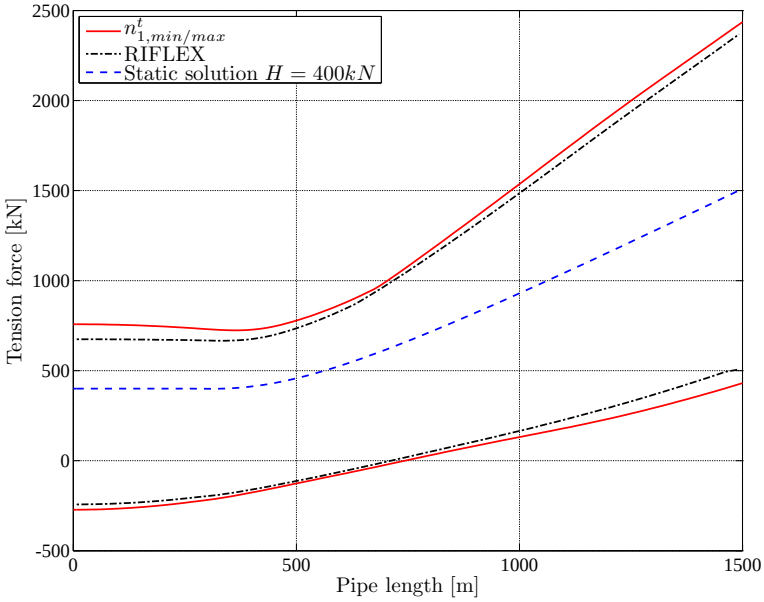

Figure 7.13: Axial tension envelope, including the static axial tension for $H = 400kN$.

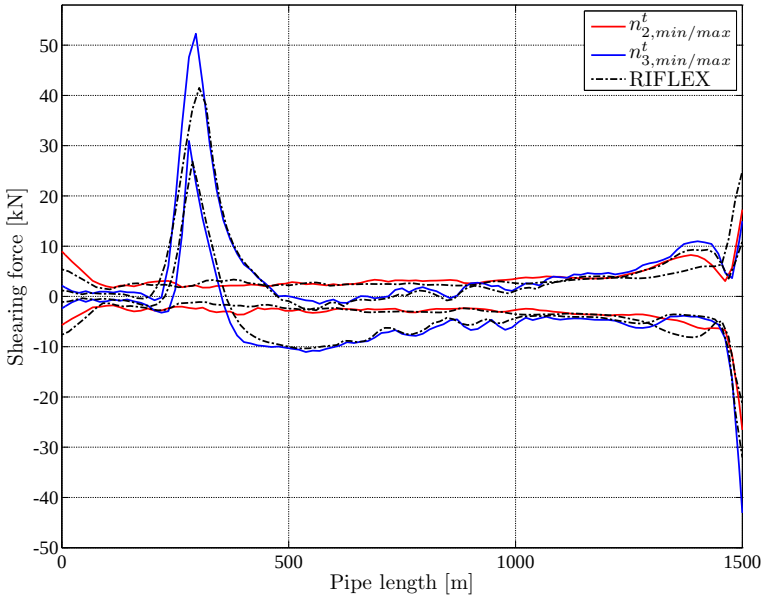

Figure 7.14: Shear force envelope.

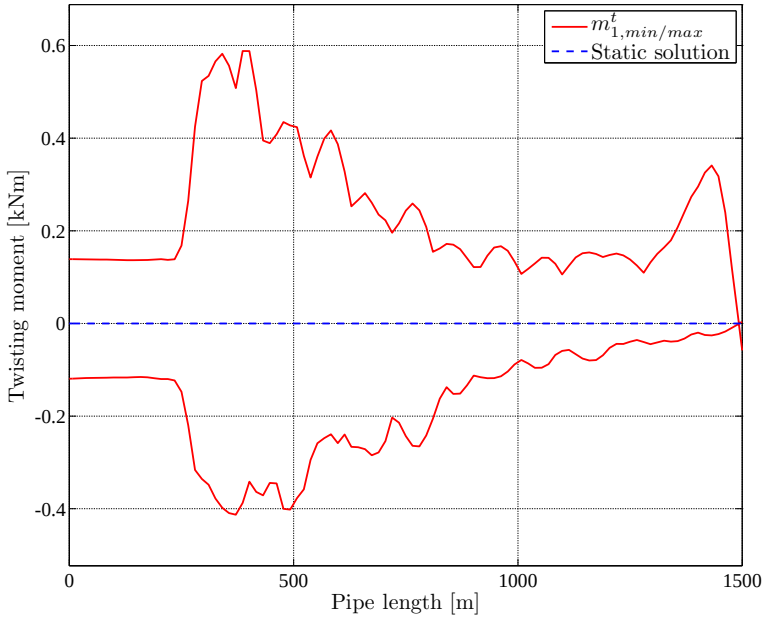

Figure 7.15: Twisting moment envelope about $\boldsymbol{m}_1^t$. There are no twisting forces in the static solution.

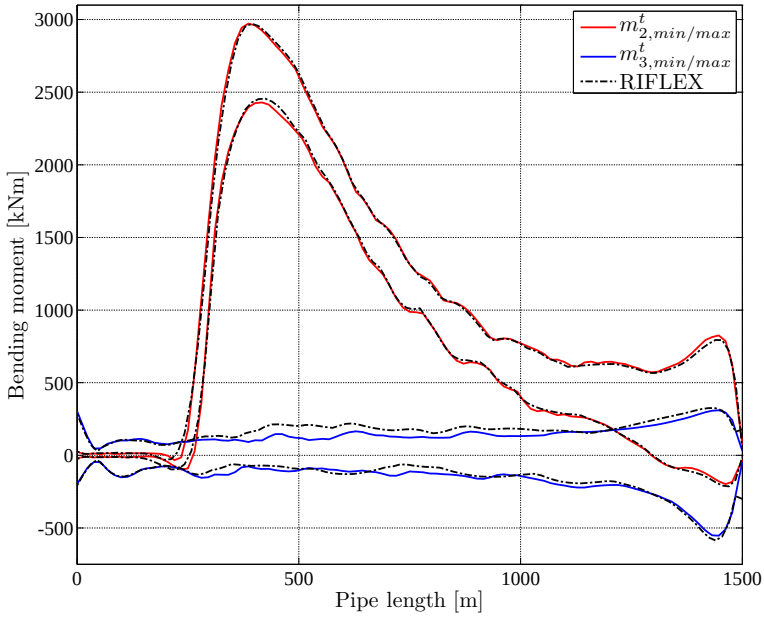

Figure 7.16: Bending moment envelope about the $\boldsymbol{t}_2$ and the $\boldsymbol{t}_3$ axis along the pipe.

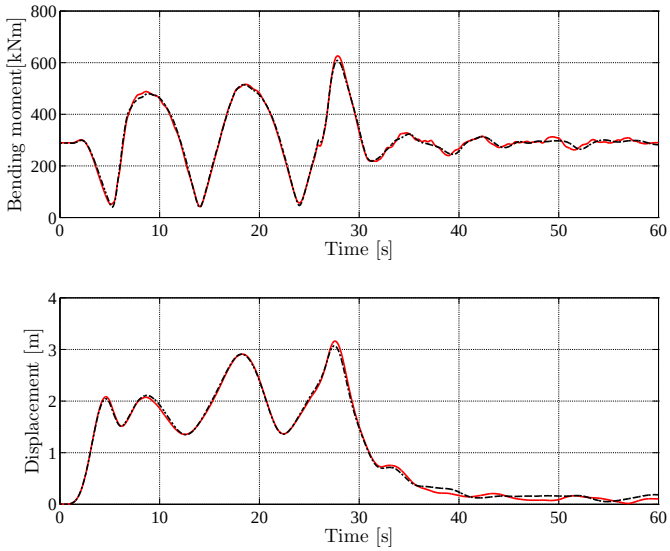

Figure 7.17: Dynamic bending moment *(top)* and relative displacement *(bottom)* for a node ($N = 90$) close to the surface vessel.

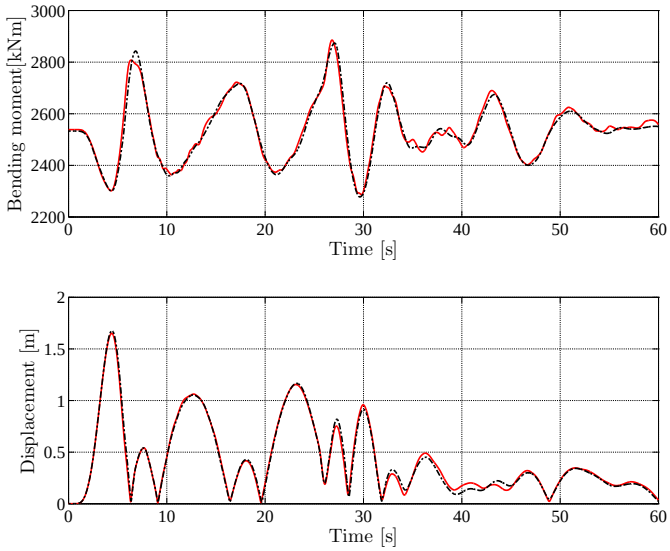

Figure 7.18: Dynamic bending moment *(top)* and relative displacement *(bottom)* for a node ($N = 25$) close to the touchdown point.

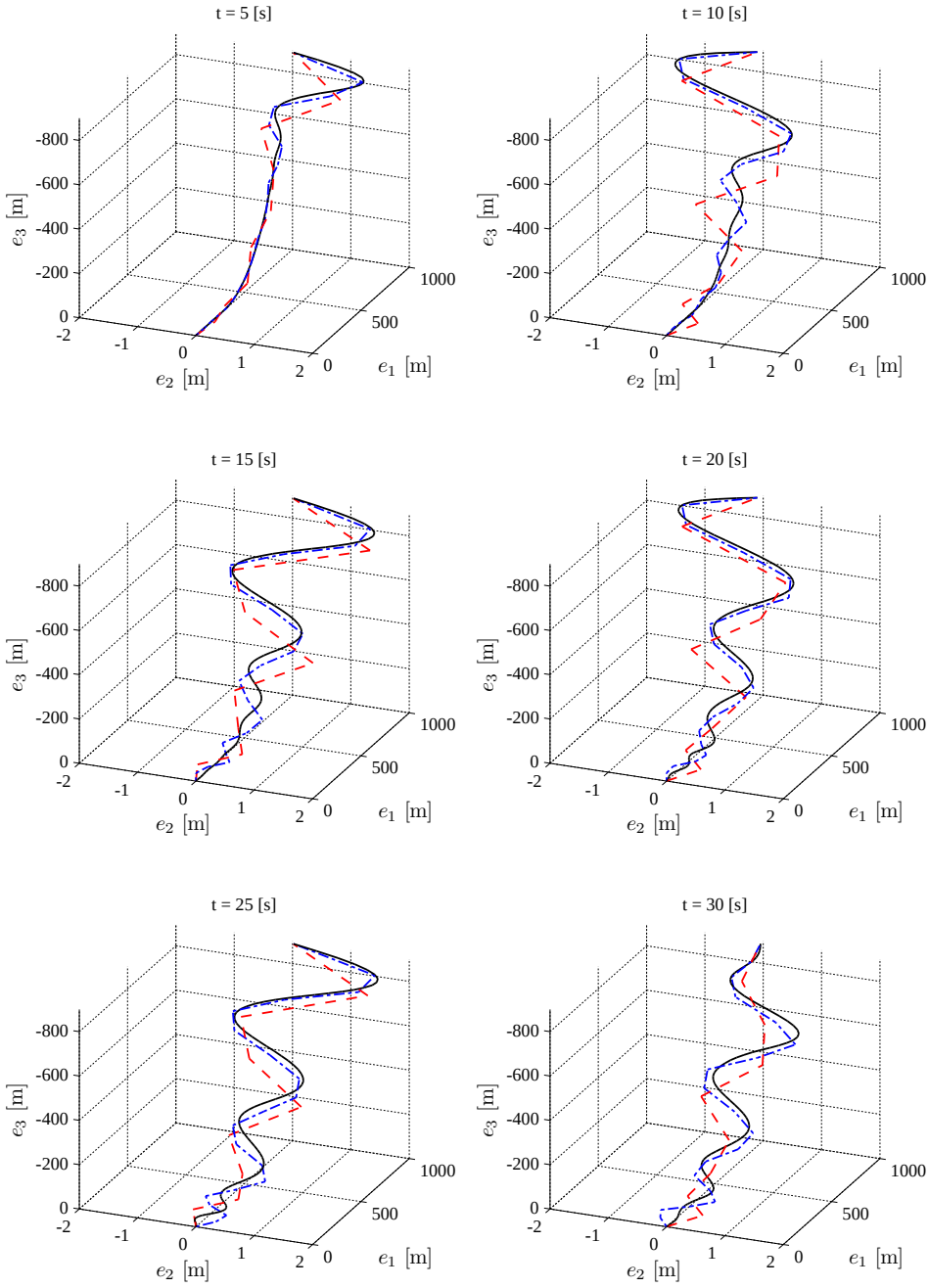

Figure 7.19: Comparing pipe configurations for $N = 10$ *(red dashed line)*, 20 *(blue dash–dot line)*, 100 *(black solid line)*.

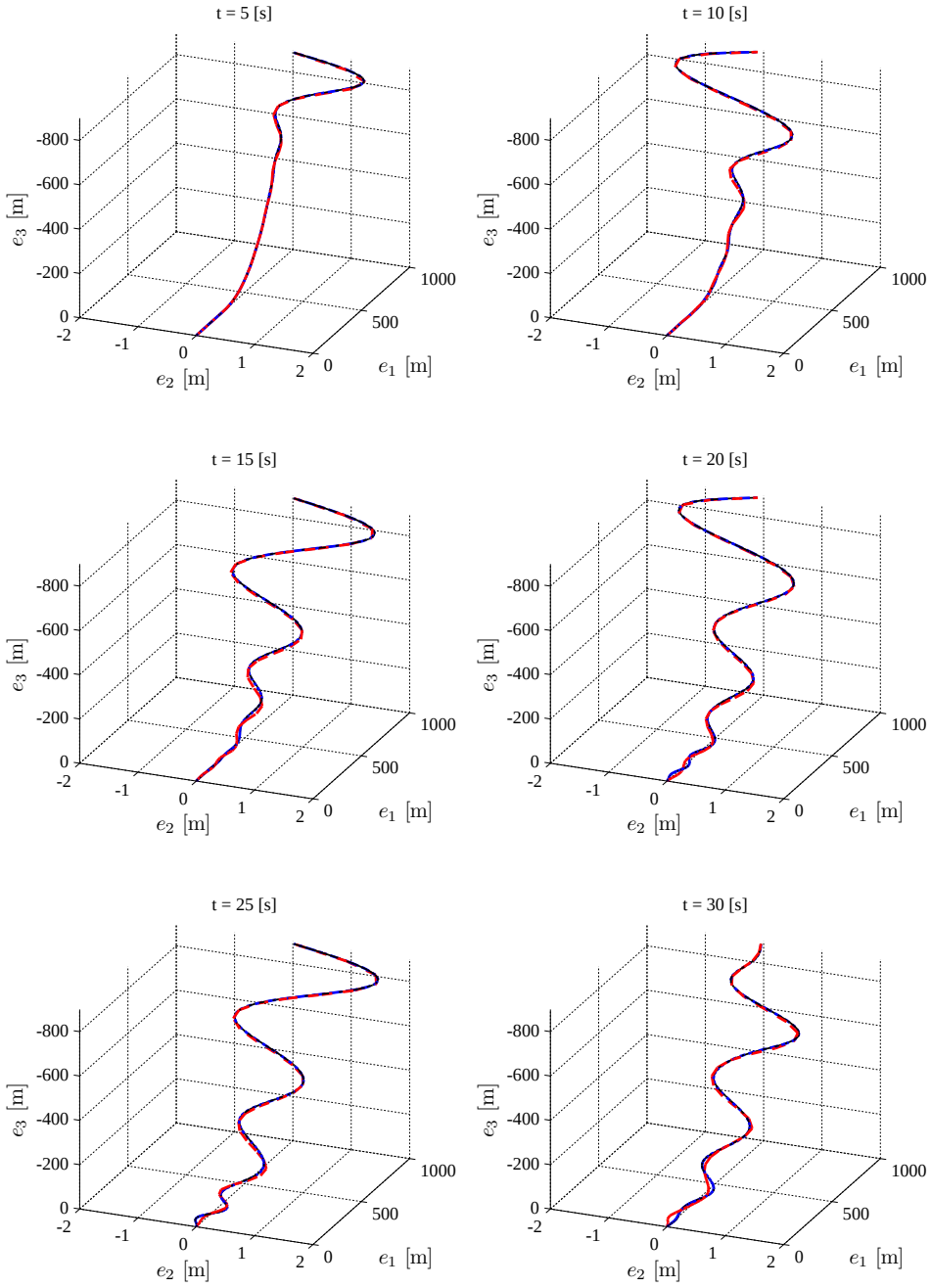

Figure 7.20: Comparing pipe configurations for $N = 40$ *(red dashed line)*, 80 *(blue dash–dot line)*, 100 *(black solid line)*.

7.4 Conclusions

A numerical implementation of the proposed PDE model has been developed, and successfully validated against the catenary equation and RIFLEX. The simulation results documents that the FEM model derived from the PDE model yields results with is very similar to that of RIFLEX, and may be used for analysis and simulation of a pipe string suspended from a surface vessel to the seabed. The range of analyses that can be performed using the PDE model extends that of RIFLEX, since the dynamics of the surface vessel is included in the model. Hence, it may be used to e.g., analyze the interaction between a pipe string and a motion control systems for the surface vessel.

Implementation

The numerical implementation is done in Matlab. The simulation results are accurate, but the computation time of the natural catenary or RIFLEX can not be achieved. The Matlab implementation will typically for static computations complete in the range of minutes for a large number of nodes ($N = 200$), while for the dynamic simulations, the simulation of $60\,s$ may take hours for a small number of nodes ($N = 10$), and considerably longer for $N > 10$. All simulations are performed on regular computers. However, it seems that implementing the FEM model in a more suited compilable language, e.g., *C* or *Fortran*, will speed up the execution of the computations. Implementing a dedicated time discretization algorithm rather than using general built–in functions, may also improve computation time since the discretization and integration methods can be chosen based on detailed knowledge of the model, see e.g., Romero and Armero (2002); Betsch and Steinmann (2002); McRobie and Lasenby (1999).

In the implemented model, rotations are parameterized using Euler angles. Euler angles have inherent singularities, which the system may move close to, and then slow down the computation. Using a parametrization for the rotations that does not introduce singularities may make the system more reliable, and possibly faster. The beam model (6.25)–(6.26) is parameterized by quaternions in Säfström (2009).

Simulations

Based on the static and dynamic simulations results presented in this chapter, and the comparisons to the results obtained from the natural catenary equation and RIFLEX, we claim that the PDE pipe model (6.30)–(6.31) is validated. This also implies the verification of the development of the semi–discrete FEM model derived in the section 7.1. By considering the analysis results, the difference between the results obtained are not more than what can be expected from different numerical implementation, and the dynamics of the proposed model is very close to that obtained by RIFLEX both with respect to displacement and forces.

Convergence

The convergence of the model as $N \to \infty$ is briefly discussed. Since the difference between the results obtained in the dynamic simulations for $N = 80$ and $N = 100$, there will be little to gain from increasing N further. This implies that for $N \to \infty$, the solution of the discretized FEM model will converge to the true solution of the PDE.

Chapter 8

Conclusions and Recommendations for Future Work

This thesis has focused on offshore pipelay dynamics. In this final chapter, it is appropriate to recall the initial motivation for this work, as given in Section 1.1, to conclude on what was achieved, and to give recommendations for future work.

8.1 Conclusions

The main three objectives that have been addressed in this thesis are:

- Offshore pipelaying in a control perspective.
- A new nonlinear robotic pipe model.
- A new nonlinear FEM formulation based on exact kinematics.

Offshore Pipelaying in a Control Perspective

From a control engineering perspective, the objective of the pipelay operation is to install a pipeline along a reference path on the seabed, which can be stated as a *path–following* control problem, where the touchdown point track the reference path. The path–following problem could easily be solved if the touchdown point could be directly controlled. However, all the actuators are located onboard the pipelay vessel. Hence, the touchdown point position is determined by the free configuration of the elastic pipe in the water, which in turn is governed by the lift-off angle through the applied pipe–lay tension. Finally, this tension is controlled by the position of the pipelay vessel. The pipe and pipelay vessel is subject to environmental disturbances, so that in order to control the position of the touchdown

point, the vessel must track a dynamic target at the surface. This extends the control problem to a *dynamic target–tracking* problem.

The dynamic target tracking problem can be solved by extending the vessel motion control system with a *guidance* component. For a desired touchdown point position, the guidance system can compute the dynamic target reference for the DP system, based on on–line measurements and an adequate dynamic pipe model. In implementing such a control system, obtaining a suitable model for the pipeline is the task requiring most work, since several on–line measurements are already available in the pipelay operation, and guidance can not be implemented without this model.

Fundamental understanding of the control objectives, challenges, methods and background for offshore pipelaying, is sufficiently provided here to enable control engineers to work in the field of offshore pipeline installation.

A Robotic Pipe Model

A simplified dynamic model for the pipeline based on robotics is derived for an arbitrary number of links in Chapter 5. A limited validation of the model is performed. This model can be used for simulations and in model based controllers. The model is applicable in simulations where the main dynamics are required, and the available computation time is limited, e.g. model–based controllers. The model implementation in Matlab developed as a part of this thesis was not able to perform in real–time. However, it seems likely that optimization of the code should be able to reduce the computation time.

PDE and FEM Pipe Model

A nonlinear PDE formulation for a the dynamics of an elastic pipeline dynamics is successfully developed. The formulation is on a Newton–Euler form, based on the linear and angular momentum balance equation for a beam, where external loads have been added by superposition. A passivity analysis of the PDE, also including the dynamics for a surface vessel is one boundary condition is performed, and these systems are found to be input–output passive based on energy consideration.

A nonlinear FEM model of the dynamics of the pipe is derived from the PDE as a set of ODEs by using calculus of variations. By not linearizing the system, the energy properties of the system is preserved. This FEM model is validated against the natural catenary equation and RIFLEX, and documented by numerous plots comparing the results with respect to geometry and internal loads. These plots show that the nominal values and the dynamics of the FEM model and RIFLEX are almost identical. The difference is not more than what can be expected from the numerical implementation.

The single most important result in this thesis is the development and validation of this model FEM model. Important properties found in RIFLEX is also present here, but in addition it has properties that makes it suitable for simulation and control applications.

8.2 Future Work

In the attempt to answer one question, new questions frequently arise.

Offshore Pipelaying in a Control Perspective

A guidance system extending the DP system has in previous sections been considered a solution to the dynamic target–tracking problem, *The Pipelay Problem*. Applying the developed FEM model, a dynamic mapping between the touchdown point and the surface vessel can be computed, and attention should now be focused at designing such a guidance system to close the control–loop.

A Robotic Pipe Model

Future work to extend and improve this model is described in the concluding section of Chapter 5. The model should be extended to also include added mass and environmental loads. Further, the model should be extended to three dimensional space, and further dynamic validations should be performed to get a more complete understanding of the model. A validation study of this model with the nonlinear FEM model should be considered.

PDE and FEM Pipe Model

The future work on the nonlinear FEM model can be separated in three areas, related to the considered effects in the model, the discretization methods, and applications.

Some effects are not included in the model, and in order to complete it, the following loads should be added:

- Added mass,
- wave loads on the pipe,
- a small linear damping in the damping term.

The implementation applied to obtain the results presented here is done in Matlab, where an integrated general purpose time integrator has been applied. This resulted is computation times considerably exceeding that of RIFLEX, which has a comparable complexity. Optimizing the code, and preferably re–code in a more optimal manner is necessary in order to apply the model to more test cases. Additionally, since RIFLEX was designed, the field of computational numerics in mathematics has developed new methods in variational calculus that a potential successor to RIFLEX should take advantage of.

The model is applicable to other slender structures with the same elastic properties. In our case a surface vessel is used for the upper boundary condition, and a fixed position is used for the lower boundary condition, but the model is not limited to this. The model could e.g., be used to simulate an ROV with an attached umbilical, either fixed, or connected to a vessel.

Applying the FEM model as an observer for internal states of stress and strain in the pipe enables controllers controlling the stresses directly rather than the pipe configuration.

More notes on future work, improvements for the model and the implementation is described in the concluding sections of Chapters 6 and 7.

Bibliography

Anonymous, 1987a. From car ferry to pipelaying vessel. Diesel & Gas Turbine Worldwide 19 (1), 52–54.

Anonymous, 1987b. New electrical concept for DP thruster control. Ocean Industry 22 (2), 177.

Anonymous, 1995. High performance lay vessel heads for completion this year. Oil and Gas Journal 93 (6), 58–59.

Anonymous, Jan. 1996. Converted DP Lorelay to install deepwater lines. Offshore 56 (1), 39.

Anonymous, 1997. Lorelay establishes new Gulf benchmarks. Offshore Engineer November, 45–49.

Apache II, 2009. Technip Brochure (www.technip.com).

API, 1998. API RP 1111. API, Design, Construction, Operation, and Maintenance of Offshore Hydrocarbon Pipelines.

Aranha, J., Pinto, M., da Silva, R., 2001. On the dynamic compression of risers: An analytic expression for the critical load. Applied Ocean Research 23 (2), 83–91.

Åström, K. J., 1996. Automatic control: A perspective. Colloquium on Automatic Control, Vol. 215 of Lecture Notes in Control and Information Sciences. Springer Berlin / Heidelberg, pp. 1–26.

Austin, D., Carriker, B., McGuire, T., Pratt, J., Priest, T., Pulsipher, A. G., Jul. 2004. History of the offshore oil and gas industry in Southern Louisiana. Interim report. Volume 1: Papers on the evolving offshore industry. Tech. rep., Mexico.

Bai, Y., Bai, Q., 2005. Subsea Pipelines and Risers. Elsevier.

Balas, M. J., 1978. Active control of flexible systems. Journal of Optimization Theory and Applications 25 (3), 415–436.

Betsch, P., Steinmann, P., 2002. Frame–indifferent beam finite elements based upon the geometrically exact beam theory. International Journal for Numerical Methods in Engineering 54 (12), 1775–1788.

Blanke, M., Kinnaert, M., Lunze, J., Staroswiecki, M., 2006. Diagnosis and Fault–Tolerant Control, 2nd Edition. Springer.

Braestrup, M. W., Andersen, J. B., Andersen, L. W., Bryndum, M. B., Christensen, C. J., Rishøy, N., 2005. Design and Installation of Marine Pipelines. Blackwell Science Ltd.

Bray, D., 2003. Dynamic Positioning, 2nd Edition. Vol. 9 of Oilfield Seamanship. Oilfield Publications Limited.

Breivik, M., Fossen, T. I., 2008. Guidance laws for planar motion control. In: Proceedings of the 47th IEEE Conference on Decision and Control, Cancun, Mexico.

Brewer, W. V., Dixon, D. A., 1969. Influence of lay barge motion on a deep water pipeline laid under tension. In: Proceedings of the Annual Offshore Technology Conference. OTC 1072.

Bryndum, M. B., Colquhoun, R. S., Verway, A., 1982. Dynamic lay stresses for pipelines. In: Proceedings of the Annual Offshore Technology Conference. OTC 4267.

BS, 1993. BS 8010. BSI, Code of Practice for Pipeline – Part 3. Pipeline Subsea: Design, Construction and Installation.

Callegari, M., Canella, F., Titti, F. M., Bruschi, R., Torselletti, E., Vitali, L., 2000. Concurrent design of an active automated system for the control of stinger/pipe reaction forces of a marine pipelaying system. In: Proceedings of the Int. Workshop on Harbour, Maritime & Multimodal Logistics Modelling and Simulation, Portofino, Italy.

Castoro 7, 2009. Saipem Brochure (www.saipem.it).

Cavicchi, M., Ardavanis, K., 2003. J–lay installations lessons learned. In: Proceedings of the Annual Offshore Technology Conference. OTC 15333.

Chatjigeorgiou, I. K., Feb. 2008. Solution of the boundary layer problems for calculating the natural modes of riser–type slender structures. Journal of Offshore Mechanics and Arctic Engineering 130 (1), 011003.

Chickasaw, 2009. Global Industries Brochure (www.globalind.com).

Choi, H., Jo, H., 1999. Characteristics of ultra–deepwater pipelay analysis. In: Proceedings of the Annual Offshore Technology Conference. OTC 10710.

Collier, G. P., Rosier, P., 1995. Environmental impact of submarine pipeline installation. Journal of Offshore Technology 3 (2), 9–14.

Cox, H. D., Hammett, D. S., Ronald, D. J., Shatto Jr., H. L., Jul. 1967. Tension pipe laying method. U.S. Patent 3331212.

Det Norske Veritas, 2000. Offshore Standard DNV–OS–F101 Submarine Pipeline Systems. DNV.

Dixon, D., Rutledge, D., February 1968. Stiffened catenary calculations in pipeline laying problem. ASME Journal of Engineering for Industry 90 (1), 153–160.

Egeland, O., Gravdahl, J. T., 2002. Modeling and Simulation for Automatic Control, 1st Edition. Marine Cybernetics.

Faldini, R., 1999. S7000: A new horizon. In: Proceedings of the Annual Offshore Technology Conference. OTC 10712.

Faltinsen, O. M., 1990. Sea Loads on Ships and Offshore Structures. Cambridge University Press.

Fathi, D., 2004. ShipX Vessel Responses (VERES). MARINTEK Trondheim, www.marintek.sintef.no.

Faÿ, H., 1990. Dynamic Positioning Systems: Principles, Design and Applications. Éditions Technip.

Fossen, T. I., 1994. Guidance and Control of Ocean Vehicles. John Wiley & Sons Ltd.

Fossen, T. I., 2002. Marine Control Systems: Guidance, Navigation, and Control of Ships, Rigs and Underwater Vehicles, 1st Edition. Marine Cybernetics, Trondheim Norway.

Fossen, T. I., Perez, T., 2004. Marine systems simulator (MSS). URL `www.marinecontrol.org`

Fossen, T. I., Smogeli, Ø. N., 2004. Nonlinear time–domain strip theory formulation for low–speed manoeuvering and station–keeping. Modeling, Identification and Control 25 (4), 201–221.

Fylling, I., Larsen, C. M., Sødahl, N., Passano, E., Bech, A., Engseth, A. G., Lie, H., Ormberg, H., 2008. RIFLEX User's Manual 3.6, MARINTEK, Trondheim, Norway.

Guo, B., Song, S., Chacko, J., Ghalambor, A., 2005. Offshore Pipelines. Gulf Professional Publishing.

Heerema, E., 2005. Recent achievements and present trends in deepwater pipe–lay systems. In: Proceedings of the Annual Offshore Technology Conference. OTC 17627.

Heerema, E. P., 1995. DP pipelay vessel 'Solitaire': Plunging into the deep. In: Proceedings of the International Conference on Offshore Mechanics and Arctic Engineering – OMAE. Vol. 5. ASME, Copenhagen, Denmark, pp. 525–537.

Heerema, E. P., 1998. Major deepwater pipelay vessel starts work in North Sea. Oil and Gas Journal 96 (18), 78–82.

Irvine, H. M., 1981. Cable Structures. The MIT Press.

ISO, 2000. ISO 13623:2000 – Petroleum and natural gas industries – Pipeline transportation systems. ISO.

Jensen, G. A., Fossen, T. I., 2009. A robotic approach to nonlinear dynamic modeling of offshore pipelaying operations. In: Proceedings of the 8th IFAC International Conference on Manoeuvring and Control of Marine Craft, Guarujá (SP), Brazil.

Jensen, G. A., Säfström, N., Nguyen, T. D., Fossen, T. I., 2009. Modeling and control of offshore pipelay operations based on a finite strain pipe model. In: Proceedings of the 2009 American Control Conference, St. Louis, USA.

Jensen, G. A., Transeth, A. A., Nguyen, T. D., 2008. Modelling and control of offshore marine pipeline during pipelay. In: Proceedings of the 17th IFAC World Congress, Seoul, Korea.

Johansen, V., 2007. Modelling of flexible slender systems for real–time simulation and control applications. Ph.D. thesis, Norwegian University of Science and Technology.

Khalil, H., 2002. Nonlinear Systems, 3rd Edition. Prentice Hall.

Knight, R., Palathingal, O., 2007. Pipelay market constrained by vessel shortages? In: OTC07 Show Daily 05.02.07. pp. 20–21.

Knott, T., Jul. 2005. Solitaire shines even brighter. Offshore Engineer, 22–30.

Kongsberg, 2006. Kongsberg K–Pos DP Dynamic Positioning System. Kongsberg Maritime AS, report no. 301093/B.

Kyriakides, S., Corona, E., 2007. Mechanics of Offshore Pipelines, Volume 1: Buckling and Collapse, 1st Edition. Elsevier.

Langner, C. G., 1969. The articulated stinger: A new tool for laying offshore pipelines. In: Proceedings of the Annual Offshore Technology Conference. OTC 1073.

Larsen, C. M., 1976. Static and dynamic analysis of offshore pipelines during installation. Ph.D. thesis, Norges tekniske høgskole. Institutt for skipskonstruksjoner.

Leffer, W. L., Pattarozzi, R., Sterling, G., 2003. Deepwater Petroleum Exploration & Production: A Nontechnical Guide. PennWell Books.

Lenci, S., Callegari, M., Aug. 2005. Simple analytical models for the J–lay problem. Acta Mechanica 178 (1–2), 23–29.

Love, A. E. H., 1944. The Mathematical Theory of Elasticity. Dover, New York.

Marbus, G., 2007. Verification of the water forces on stinger of Allseas Solitaire. Master's thesis, Delft University of Technology.

Martinez, C. E., Goncalves, R., 2003. Laying modeling of submarine pipelines using contact elements into a corotational formulation. Journal of Offshore Mechanics and Arctic Engineering 125 (2), 145–152.

McRobie, F., Lasenby, J., 1999. Simo–Vu Quoc rods using Clifford algebra. International Journal for Numerical Methods in Engineering 45 (4), 377–398.

Miesner, T. O., Leffler, W. L., 2006. Oil & Gas Pipelines in Nontechnical Language. PennWell Books.

Molin, B., 2002. Hydrodynamique des Structures Offshores. Editions TECHNIP.

Morison, J. R., O'Brien, M. P., Johnson, J. W., Schaaf, S. A., 1950. The force exerted by surface waves on piles. Petroleum Transactions AIME 189, 149–189.

Mørk, K. J., Collberg, L., Bjørnsen, T., 1998. Limit state design in DNV'96 rules for submarine pipeline systems: Background and project experience. In: Proceedings of the Annual Offshore Technology Conference. OTC 8671.

Ogilvie, T. F., 1964. Recent progress toward the understanding and prediction of ship motions. In: Proceedings of the Fifth Symposium on Naval Hydrodynamics, Bergen, Norway. Vol. ACR-112. ONR, pp. 3–79.

Palmer, A. C., 1994. Deepwater pipelines: Improving state of the art. In: Proceedings of the Annual Offshore Technology Conference. OTC 7541.

Palmer, A. C., Hutchinson, G., Ells, J. W., 1974. Configuration of subnmarine pipelines during laying operations. Journal of Engineeing for Industry-Transactions of the ASME 96 (4), 1112–1118.

Palmer, A. C., King, R. A., 2008. Subsea Pipeline Engineering, 2nd Edition. PennWell Books.

Perez, T., Fossen, T. I., 2007. Kinematic models for manoeuvring and seakeeping of marine vessels. Modeling, Identification and Control 28 (1), 19–30.

Perinet, D., Frazer, I., 2007. J–lay and Steep S–lay: Complementary tools for ultradeep water. In: Proceedings of the Annual Offshore Technology Conference. OTC 18669.

Perinet, D., Frazer, I., 2008. Strain criteria for deep water pipe laying operations. In: Proceedings of the Annual Offshore Technology Conference. OTC 19329.

Pesce, C. P., Martins, C. d. A., da Silveira, L. M. Y., Feb. 2006. Riser–soil interaction: Local dynamics at TDP and a discussion on the eigenvalue and the VIV problems. Journal of Offshore Mechanics and Arctic Engineering 128 (1), 39–55.

Plunkett, R., 1967. Static bending stresses in catenaries and drill strings. ASME Journal of Engineering for Industry 89, 31–36.

Pratt, J. A., Priest, T., Castaneda, C. J., 1997. Offshore Pioneers: Brown & Root and the history of offshore oil and gas. Gulf Publishing Company.

Reissner, E., 1982. Some remarks on the problem of column buckling. Ingenieur-Archiv 52, 115–119.

Rienstra, S. W., 1987. Analytical approximations for offshore pipelaying problems. In: Proceedings of ICIAM 87, Paris–La Vilette, France.

Romero, I., Armero, F., 2002. An objective finite element approximation of the kinematics of geometrically exact rods and its use in the formulation of an energy-momentum conserving scheme in dynamics. International Journal for Numerical Methods in Engineering 54 (12), 1683–1716.

Säfström, N., 2009. Modeling and simulation of rigid body and rod dynamics via geometric methods. Ph.D. thesis, Norwegian University of Science and Technology.

Sciavicco, L., Siciliano, B., 2001. Modelling and Control of Robot Manipulators, 2nd Edition. Springer.

Searle, A., 2004. PLUTO Pipe–Line Under The Ocean, 2nd Edition. Shaklin Chine.

Seven Oceans, 2009. Subsea7 Brochure (www.subsea7.com).

Seyed, F. B., Patel, M. H., 1992. Mathematics of flexible risers including pressure and interal flow effects. Marine Structures 5 (2–3), 121–150.

Simo, J. C., May 1985. A finite strain beam formulation. The three-dimensional dynamic problem. Part I. Computer Methods in Applied Mechanics and Engineering 49 (1), 55–70.

Simo, J. C., Tarnow, N., Doblare, M., 1995. Non–linear dynamics of three–dimensional rods: Exact energy and momentum conserving algorithms. International Journal for Numerical Methods in Engineering 38, 1431–1473.

Simo, J. C., Vu–Quoc, L., Oct. 1986. A three–dimensional finite–strain rod model. Part II: Computational aspects. Computer Methods in Applied Mechanics and Engineering 58 (1), 79–116.

Simo, J. C., Vu–Quoc, L., Feb. 1988. On the dynamics in space of rods undergoing large motions – a geometrically exact approach. Computer Methods in Applied Mechanics and Engineering 66 (2), 125–161.

Skjetne, R., Fossen, T. I., Kokotović, P. V., 2004. Robust output maneuvering for a class of nonlinear systems. Automatica 40 (3), 373–383.

Small, S. W., 1970. The submarine pipeline as a structure. In: Proceedings of the Annual Offshore Technology Conference. OTC 1223.

SNAME, 1950. Nomenclature for treating the motion of a submerged body through a fluid. Technical and Research Bulletin No. 1–5.

Sørensen, A. J., Leira, B., Strand, J. P., Larsen, C. M., 2001. Optimal setpoint chasing in dynamic positioning of deep–water drilling and intervention vessels. International Journal of Robust and Nonlinear Control 11 (13), 1187–1205.

Sparks, C. P., 2007. Fundamentals of Marine Riser Mechanics: Basic Principles and Simplified Analyses. PennWell.

Spong, M., Vidyasagar, M., 1989. Robot Dynamics and Control. John Wiley & Sons, New York.

Steenhuis, A. L. J., van Norden, T., Regelink, J., Krutzen, M., 2007. Modifications to the pipelay vessel Solitaire for the Independence trail project. In: Proceedings of the Annual Offshore Technology Conference. OTC 19059.

Strang, G., 1986. Linear Algebra and its Applications, 3rd Edition. Brooks/Cole.

Sumer, B. M., Fredsøe, J., 2006. Hydrodynamics Around Cyclindrical Structures. World Scientific Publishing Company, revised edition, (Advanced Series on Ocean Engineering).

Timmermans, W., 2000. The past and future of offshore pipelines. Offshore Pipeline Technology EP 1108.

Torselletti, E., Bruschi, R., Vitali, L., Marchesani, F., 1999. Lay challenges in deep waters: Technologies and criteria. In: Proceedings of the 2nd Int. Deepwater Pipeline Technology Conf., New Orleans, Louisiana, USA.

Triantafyllou, M. S., 1990. Cable mechanics with marine appl., lecture notes. Dept. of Ocaen Eng., M.I.T., Cambridge, MA.

van den Boom, H. J. J., 1985. Dynamic behaviour of mooring lines. In: Proceedings of the 4th Int. Conference on Behaviour of Offshore Structures.

Wade, B. G., Dwyer, M., 1976. On the application of Morison's equation to fixed offshore platforms. In: Proceedings of the Annual Offshore Technology Conference. OTC 2723.

WAMIT, 2004. WAMIT User Manual. www.wamit.com.

Wilhoit, J. C., Merwin, J. E., Feb 1967. Pipe stress induced in laying offshore pipeline. Journal of Engineering for Industry.

Wilkins, J. R., 1994. From S–lay to J–lay. In: Proceedings of the 13th Int. Conference on Offshore Mechanics and Arctic Engineering, New York, NY, USA.

Worldsen, A. S., 2007. Modelling and control of tensegrity structure. Ph.D. thesis, Norwegian University of Science and Technology.

Yttervik, R., 2005. Ocean current variability in relation to offshore engineering. Ph.D. thesis, Norwegian University of Science and Technology.

Appendix A

Mathematical Preliminaries

Fundamental mathematical concepts related to vectors, matrices, reference frames and vector differentiation are briefly addressed. More extensive treatment of these concepts are found in text books such as e.g., Egeland and Gravdahl (2002).

A.1 Coordinate Vectors

Entities such as forces, torques, positions, velocities, and accelerations are frequently described by vectors. A vector $\vec{u}$ is given by its magnitude $|\vec{u}|$, and its direction. This coordinate–free vector form is impractical for vector operations, therefore coordinate vectors will be used in this thesis. Consider a Carthesian coordinate frame a, with orthonormal unit vectors $\vec{a}_1$, $\vec{a}_2$, and $\vec{a}_3$. The vector $\vec{u}$ can be expressed as a linear combination the unit vectors, see Figure A.1a, (Egeland and Gravdahl, 2002),

$$\vec{u} = u_1\vec{a}_1 + u_2\vec{a}_2 + u_3\vec{a}_3, \tag{A.1}$$

and the equivalent coordinate vector, $\boldsymbol{u}^a$, is a column vector of the coefficients,

$$\boldsymbol{u}^a = \begin{bmatrix} u_1 & u_2 & u_3 \end{bmatrix}^{\mathrm{T}}. \tag{A.2}$$

The usual inner product of two vectors $\boldsymbol{u}, \boldsymbol{v} \in \mathbb{R}^n$ is denoted $\langle \boldsymbol{u}, \boldsymbol{v} \rangle$ or equivalently on vectorial form $\boldsymbol{u}^{\mathrm{T}}\boldsymbol{v}$. Vectors are denoted by a boldface lower case letter, where the corresponding reference frame is indicated by a superscript. Matrices are denoted by boldface uppercase letters.

A.2 Reference Frames

Two types of reference frames are used in this thesis; *inertial* frames, and *body–fixed* frames. An inertial reference frame, or *Newtonian* frame, is a reference frame which is not accelerating, such that Newtons laws apply. A body–fixed frame remains fixed to a location in a body as it moves relative to the inertial frame. Elastic bodies are also subject to deformation.

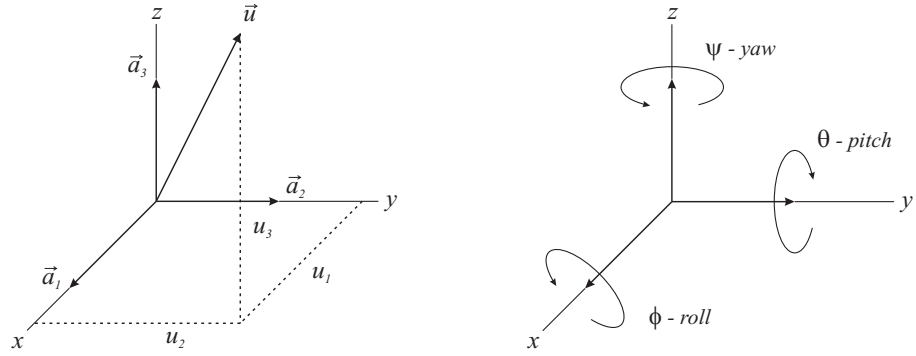

(a) The coordinate vector. (b) Euler angles.

Figure A.1: Notation

The *North–East–Down* (NED) reference frame n is commonly adopted to describe the motion of a marine vessel, e.g., the pipelay vessel (Fossen, 2002). The frame is usually defined as the tangent plane on the surface of the Earth, moving with the vessel. The unit vectors are in the directions *north*, *east* and *down*. Marine vessels operating in a local area will use the Earth–fixed tangent plane for navigation. Assuming this frame to be inertial is commonly referred to as *flat Earth navigation*. For a marine vessel, b is a body–fixed reference with origin commonly chosen to be midships in the water line, and where the axes coincide with the principal axes of inertia. This frame is convenient for expressing linear and angular velocities, whereas the position and orientation must be expressed in the inertial frame.

For the development of a robotic pipe model in Chapter 5, the inertial reference frame from robotics is applied. This frame is referred to as the *fixed frame*, and denoted by *0* (Spong and Vidyasagar, 1989), and is typically fixed to the base of the robot manipulator. The links of the manipulator are considered rigid, and a body–fixed reference frame is fixed to each link.

For the pipe model developed in Chapter 6, the reference frames applied in Simo (1985) are adopted. An inertial frame e is fixed to one end of the elastic beam, while a body–fixed reference frame t is fixed to every point along the line of centroids of the beam.

A.3 Rotation Matrices

Let $\boldsymbol{u}^b$ be $\vec{u}$ expressed in frame b with orthonormal unit vectors $\vec{b}_1$, $\vec{b}_2$, and $\vec{b}_3$. It can then be shown that $\boldsymbol{u}^a$ and $\boldsymbol{u}^b$ are related as

$$\boldsymbol{u}^a = \boldsymbol{R}_b^a \boldsymbol{u}^b, \quad \boldsymbol{u} \in \mathbb{R}^3, \tag{A.3}$$

where

$$\boldsymbol{R}_b^a \in SO(3), \quad SO(3) \triangleq \{\boldsymbol{R}_b^a \in \mathbb{R}^{3\times 3} \,|\, (\boldsymbol{R}_b^a)^{\mathrm{T}} \boldsymbol{R}_b^a = \boldsymbol{I}_{3\times 3},\ \det \boldsymbol{R}_b^a = 1\}, \tag{A.4}$$

is a so–called *rotation matrix* from a to b, that transforms the vector coordinates of $\boldsymbol{u}^b$ in frame b to frame a. This notation is adopted from Egeland and Gravdahl (2002). In addition to representing the coordinate transformation between the coordinates of a point expressed in two different frames, the rotation matrix is also describing the mutual orientation between two coordinate frames where its column vectors are the directional cosines of the axes of the rotated frame with respect to the original frame (Sciavicco and Siciliano, 2001). Hence, the orientation of a body can be expressed by the orientation of the body–fixed reference frame with respect to the inertial frame.

A rotation can be expressed as a sequence of partial rotations where each rotation is defined with respect to the preceding one (Sciavicco and Siciliano, 2001). Hence, a rotation matrix of composite rotations is the product of rotation matrices, and by introducing a reference frame c, $\boldsymbol{R}_b^a$ can be found by the composite rotations

$$\boldsymbol{R}_b^a = \boldsymbol{R}_c^a \boldsymbol{R}_b^c. \tag{A.5}$$

The most common parameterizations of the $\boldsymbol{R}_b^a$ is by Euler angles, $\boldsymbol{R}_b^a(\boldsymbol{\Theta})$, and quaternions, $\boldsymbol{R}_b^a(\boldsymbol{q})$. Euler angles are most frequently applied in marine applications, and will be applied in this thesis, see Figure A.1b. The Euler angles are *roll* ϕ, rotation about the x–axis, *pitch* θ, rotation about the y–axis, and *yaw* ψ, rotation about the z–axis. The elementary rotations about the x, y and z axes are

$$\boldsymbol{R}_{x,\phi} = \begin{bmatrix} 1 & 0 & 0 \\ 0 & \mathrm{c}\,\phi & -\mathrm{s}\,\phi \\ 0 & \mathrm{s}\,\phi & \mathrm{c}\,\phi \end{bmatrix}, \quad \boldsymbol{R}_{y,\theta} = \begin{bmatrix} \mathrm{c}\,\theta & 0 & \mathrm{s}\,\theta \\ 0 & 1 & 0 \\ -\mathrm{s}\,\theta & 0 & \mathrm{c}\,\theta \end{bmatrix},$$
$$\boldsymbol{R}_{z,\psi} = \begin{bmatrix} \mathrm{c}\,\psi & -\mathrm{s}\,\psi & 0 \\ \mathrm{s}\,\psi & \mathrm{c}\,\psi & 0 \\ 0 & 0 & 1 \end{bmatrix}, \tag{A.6}$$

where $\mathrm{s}\cdot = \sin(\cdot)$, and $\mathrm{c}\cdot = \cos(\cdot)$. Let $\boldsymbol{\Theta} = [\phi, \theta, \psi]^{\mathrm{T}}$ give the orientation of frame b with respect to a. Then $\boldsymbol{R}_b^a$ can be parametrized in Euler angles $\boldsymbol{R}_b^a(\boldsymbol{\Theta})$, by the zyx–convention, which is locally to $SO(3)$ as

$$\boldsymbol{R}_b^a(\boldsymbol{\Theta}) = \boldsymbol{R}_{z,\psi}\boldsymbol{R}_{y,\theta}\boldsymbol{R}_{x,\phi}. \tag{A.7}$$

Rotations in the two dimensional plane is addresses in chapters 2 and 5. In this case the rotation matrix $\boldsymbol{R}_b^a(\psi) \in SO(2)$ from frame a to b is simply the rotation ψ about the axis normal to the plane,

$$\boldsymbol{R}_b^a(\psi) = \begin{bmatrix} \mathrm{c}\,\psi & -\mathrm{s}\,\psi \\ \mathrm{s}\,\psi & \mathrm{c}\,\psi \end{bmatrix}. \tag{A.8}$$

A.4 Differentiation of Vectors

Vectors must be differentiated with respect to a frame. Differentiation of the coordinate vector $\boldsymbol{u}^a = \boldsymbol{u}^a(t)$ with respect to time t, is found by differentiating the

components of the vector,

$$\dot{\boldsymbol{u}}^a = \frac{d}{dt}\left(\boldsymbol{u}^a\right) = \left[\begin{array}{ccc} \dot{u}_1 & \dot{u}_2 & \dot{u}_3 \end{array}\right]^{\mathrm{T}}. \tag{A.9}$$

For partial differentiation of $\boldsymbol{u}^a = \boldsymbol{u}^a\left(S,t\right)$, where S is the spatial curve parameter, the partial derivatives are denoted by

$$\partial_S \boldsymbol{u}^a\left(S,t\right) = \frac{{}^a\partial}{\partial S}\boldsymbol{u}^a\left(S,t\right), \quad \dot{\boldsymbol{u}}^a\left(S,t\right) = \partial_t \boldsymbol{u}^a\left(S,t\right) = \frac{{}^a\partial}{\partial t}\boldsymbol{u}^a\left(S,t\right). \tag{A.10}$$

Differentating (A.3) yields the relation between time derivatives of $\boldsymbol{u}^a$ and $\boldsymbol{u}^b$,

$$\dot{\boldsymbol{u}}^a = \boldsymbol{R}^a_b \dot{\boldsymbol{u}}^b + \dot{\boldsymbol{R}}^a_b \boldsymbol{u}^b, \tag{A.11}$$

which is equivalent to

$$\dot{\boldsymbol{u}}^a = \boldsymbol{R}^a_b \left[\dot{\boldsymbol{u}}^b + \left(\omega^b\right) \times \boldsymbol{u}^b\right], \tag{A.12}$$

where ω^b is the angular velocity of frame b relative to frame a given in frame b.